DISSERTATIONES
CHIMICAE
UNIVERSITATIS
TARTUENSIS
230

HEIGO ERS

Adsorption and Structuring Processes at Single Crystal Electrode – Ionic Liquid Interface – Insights from Simulations and *in situ* Studies

DISSERTATIONES CHIMICAE UNIVERSITATIS TARTUENSIS
230

DISSERTATIONES CHIMICAE UNIVERSITATIS TARTUENSIS
230

HEIGO ERS

Adsorption and Structuring Processes at Single Crystal Electrode – Ionic Liquid Interface – Insights from Simulations and *in situ* Studies

UNIVERSITY OF TARTU
Press
1632

Institute of Chemistry, Faculty of Science and Technology, University of Tartu, Estonia

The dissertation was accepted for the commencement of the degree of Doctor of Philosophy in Chemistry on June 11th, 2024, by the Council of Institute of Chemistry, University of Tartu.

Supervisors: Research Fellow Piret Pikma, PhD
University of Tartu, Estonia

Research Fellow Vladislav Ivaništšev, PhD
University of Tartu, Estonia

Professor Enn Lust, PhD
University of Tartu, Estonia

Opponent: Professor Alexei Kornyshev, PhD
Imperial College London, United Kingdom

Commencement: August 16th, 2024 at 14.15, Ravila 14A-1020, Tartu (Chemicum)

This doctoral thesis was supported by the project ″Increasing the knowledge intensity of Ida-Viru entrepreneurship″ co-funded by the European Union and by the Estonian Ministry of Education and Research (TK210).

Funded by the European Union

Investing in your future

ISSN 1406-0299 (print)
ISBN 978-9916-27-566-5 (print)
ISSN 2806-2159 (pdf)
ISBN 978-9916-27-567-2 (pdf)

University of Tartu Press
www.tyk.ee

TABLE OF CONTENTS

1. LIST OF ORIGINAL PUBLICATIONS

I. I.V. Voroshylova, **H. Ers**, V. Koverga, B. Docampo-Álvarez, P. Pikma, V.B. Ivaništšev, M.N.D.S. Cordeiro, Ionic liquid–metal interface: The origins of capacitance peaks, Electrochim. Acta 379 (2021) 138148

II. **H. Ers**, I.V. Voroshylova, P. Pikma, V.B. Ivaništšev, Double layer in ionic liquids: Temperature effect and bilayer model, J. Mol. Liq. 363 (2022) 119747

III. **H. Ers**, L. Siinor, P. Pikma, Maintaining the order: 4,4′-bipyridine self-assembled layers on the Bi(111) | ionic liquid interface, Electrochim. Acta (2024) 144081

IV. **H. Ers**, L. Siinor, C. Siimenson, E. Lust, P. Pikma, Order beyond a monolayer: The story of two self-assembled 4,4′-bipyridine layers on the Sb(111) | ionic liquid interface, Electrochim. Acta 421 (2022) 140468

V. **H. Ers**, L. Siinor, P. Pikma, The adsorption of 4,4′-bipyridine at a Cd(0001)|ionic liquid interface – The descent into disorder, Electrochem. Commun. 148 (2023) 107451

Author′s contributions:

I: Performed the analysis of molecular dynamics simulations data, participated in the derivation of bilayer model and the preparation of the manuscript.

II: Conducted molecular dynamics simulations, performed the analysis of obtained data, participated in the development of bilayer model and the preparation of the manuscript.

III: Performed electrochemical scanning tunnelling microscopy, electrochemical impedance spectroscopy measurements and density functional theory calculations, performed the analysis of obtained data and contributed to the writing of the manuscript.

IV: Conducted electrochemical scanning tunnelling microscopy, electrochemical impedance spectroscopy measurements and density functional theory calculations, performed the analysis of obtained data and contributed to the writing of the manuscript.

V: Conducted electrochemical scanning tunnelling microscopy, electrochemical impedance spectroscopy measurements and density functional theory calculations, performed the analysis of obtained data and contributed to the writing of the manuscript.

2. ACRONYMS AND SYMBOLS

4,4′-BP	4,4′-bipyridine
A	electrode surface area
ab initio	″from the first principles″ in Latin
in situ	″on site″ in Latin
ac	alternating current
AFM	atomic force microscopy
BF_4^-	tetrafluoroborate anion
$BMImPF_6$	1-butyl-3-methylimidazolium hexafluorophosphate
C	interfacial capacitance
C_H	interfacial capacitance estimated using the Helmholtz model of electrical double layer
C_{IL}	interfacial capacitance due to the non-uniform distribution of electrolyte ions at the electrode-IL interface
C_Q	quantum capacitance
C_{tot}	interfacial capacitance with quantum capacitance included
CV	cyclic voltammetry
DFT	density functional theory
d	distance
E	electrode potential
E_{ads}	adsorption energy of molecule or ion at the electrode surface
$E_{binding}$	energy related to the binding of the molecule to the electrode′s surface
E_{dif}	surface diffusion barrier
E_{inter}	energy related to the intermolecular interactions in the adsorbed layer
E_{kin}	kinetic energy of adsorbing molecule
E_m	amplitude of alternating electrode potential
E_Σ	overall potential drop accounting for the electrode′s potential drop
EC–STM	electrochemical scanning tunnelling microscopy
EIS	electrochemical impedance spectroscopy
Electrode | IL	interface between electrode and ionic liquid
$EMIm^+$	1-ethyl-3-methylimidazolium cation
$EMImBF_4$	1-ethyl-3-methylimidazolium tetrafluoroborate
f	alternating current frequency
IL	ionic liquid
j	current density
j_{ox}	current density associated with an oxidation process
j_p	current density associated with a current peak
j_m	amplitude of measured current for alternating potential
j_{tunnel}	tunnelling current

l	distance between the electrode′s surface and the first ionic liquid layer′s charge density plane
MD	molecular dynamics
PBE	Perdew–Burke–Ernzerhof exchange–correlation functional
PZC	potential of zero charge
SEIRAS	surface-enhanced infrared absorption spectroscopy
STM	scanning tunnelling microscopy
T	temperature
U_{LJ}	Lennard-Jones potential
v	electrode potential scan rate
Z	complex notation of impedance
$\|Z\|$	magnitude of impedance
Z'	real part of impedance
Z''	imaginary part of impedance
λ	charge overscreening the electrode′s charge σ
δ	distance between the first and the second ionic liquid layer
ε_{LJ}	the depth of potential well in Lennard-Jones potential
ϵ	relative permittivity (dielectric constant)
ϵ_0	vacuum permittivity
σ	electrode surface charge density
σ_{ij}	distance between atoms i and j at zero Lennard-Jones potential
Γ	amount of adsorbed species on the electrode′s surface
ω	angular frequency
θ	phase difference angle (phase shift)
κ	decay constant for the wave functions
ρ_N	number density
ρ_{bulk}	density of ionic liquid in the bulk phase
$\varphi(z)$	electric potential at distance z from the electrode′s surface
φ_{IL}	potential drop at the interface
φ_{Gr}	potential drop at the graphene electrode
φ_{BL}	potential drop at the interface estimated using bilayer model

3. INTRODUCTION

The development of modern energy devices and the transition to sustainable chemistry are essential for achieving global energy and climate goals. At the heart of numerous energy devices are processes at the electrode–electrolyte interface. The adsorption of electrolyte ions at the electrode accumulates the charge in supercapacitors, while the batteries are based on reversible redox processes of electroactive ions and electrode materials. Moreover, the adsorbed layers of organic molecules can be used to fabricate sensors, molecular wires, and switches, paving the way for the miniaturisation of electronic components [1]. Thus, the importance of understanding and accurately describing the processes at different electrode–electrolyte interfaces cannot be overstated.

Ionic liquids have attracted significant attention due to their low vapour pressure, good electrochemical stability, and tuneable properties provided by the large variety of possible combinations of cations and anions [2]. Therefore, they have been studied as possible electrolytes for energy storage applications, solvents, and reaction mediums. Their interfacial properties differ notably from common aqueous or organic electrolytes, raising the interest of fundamental electrochemists′ in describing the interactions and processes occurring at the electrode–ionic liquid interface and in the bulk ionic liquid [3].

Computational techniques such as molecular dynamics simulations and density functional theory calculations have played an integral role in describing the properties of ionic liquids. The computational techniques provide atomic-level insights into the interfacial structure at various surface charge densities, thus allowing the description of capacitance–structure relations and interactions between the adsorbed ions and the electrode surface [4]. Meanwhile, the experimental techniques facilitate the investigation of processes occurring over longer timescales, such as self-assembly and corrosion, verifying the predictions and trends of computational models, highlighting the discrepancies, and providing input for developing new models [5].

In this thesis, to investigate the electrode | ionic liquid, the model systems of graphene | $EMImBF_4$ and Au(100) | $BMImPF_6$ have been simulated at various electrode charges and temperatures. The studies of organic adsorption from ionic liquid, combining various experimental and computational techniques, were conducted on Bi(111), Sb(111), and Cd(0001) single crystal electrodes using 4,4′-bipyridine as a probe molecule.

The studies of ionic liquid electrolytes at model electrode surfaces covered in this thesis aim to:

- relate the capacitance–potential dependence to the reorganisation of the electrode | ionic liquid using molecular dynamics simulations,
- clarify the electrode | ionic liquid capacitance dependence on temperature with molecular dynamics simulations and density functional theory calculations,
- investigate the impact of ionic liquid and the electrode material characteristics on the adsorption and self-assembly of organic molecules by combining electrochemical impedance spectroscopy, electrochemical scanning tunnelling microscopy, and density functional theory calculations.

4. LITERATURE OVERVIEW

4.1. Adsorption of Organic Molecules at Electrode | Electrolyte

An electrochemical interface is the boundary region between an electrode and an electrolyte, where the forces operating on the particles differ notably from the ones acting inside the electrolyte. The interactions of the electrolyte with the electrode lead to the adsorption, *i.e.*, the accumulation of molecules and ions from the bulk electrolyte to the electrode′s surface. The adsorption processes are differentiated by the interactions that dictate the accumulation of particles. The process is considered non-specific when the ions adsorb due to the long-range Coulomb interactions [6]. In contrast, when short-range interactions determine the transfer of particles to the interface, the adsorption is described as specific. Different energy contributions that influence the adsorption of molecules can be divided as follows: the binding of the molecule to the electrode′s surface ($E_{binding}$), the intermolecular interactions inside the adsorption (surface) layer (E_{inter}), and the kinetic energy (E_{kin}) of the molecule necessary to overcome the surface diffusion barrier (E_{dif}). The interplay between those contributions is most evident in the case of highly ordered self-assembled layers, where intermolecular bonds significantly influence the adsorption kinetics and the formed structures. The optimal conditions for forming molecular self-assembled layers are $E_{binding} > E_{inter} > E_{kin} > E_{dif}$ [7].

The characteristics of any material are determined by its constituents and their interactions. Therefore, the properties and structure of the interfacial region between the electrode and electrolyte differ significantly from the bulk. An electrical potential difference across the interface develops due to the adsorption, leading to the separation of charges at the boundary between the electrode and the electrolyte. This difference is known as the potential drop. When no faradic charge transfer processes (oxidation/reduction reactions) occur at the interface, the increase of the potential drop leads to the rise of the electrode′s surface charge as well as the accumulation of counter-ions to its surface. Capacitance (C) is a central term in electrochemistry, as the amount of conserved charge per applied electric potential is crucial for energy storage considerations. Furthermore, as capacitance depends on the interfacial structure, the analysis of capacitance–potential dependences provides insights into the processes occurring at the interface.

Early adsorption studies of various organic compounds were conducted mainly on the Hg electrode using classical electrochemistry methods such as cyclic voltammetry (CV) and electrochemical impedance spectroscopy (EIS) [8–12]. These studies highlighted slow interfacial processes, leading to capacitance hysteresis and regions with significantly lower capacitance values than in Hg – pure electrolyte systems due to the formation of organic films [10–12]. Very deep capacitance depressions were observed at concentrated solutions. These depressions were related to the formation of three-dimensional organic layers

[8,13]. Similar trends have been observed at single crystal electrodes with well-defined surface structures on various surfaces and organic adsorbates [14–17]. For example, in the case of interfaces between pyridine-containing aqueous electrolyte and Au(*hkl*) [18,19], Ag(*hkl*) [20,21] or Bi(*hkl*) [22] electrodes, the adsorption of pyridine on the electrode′s surface was observed while highlighting the impact of surface crystallography to the energetics of pyridine adsorption. The impact of electrode potential on the adsorbed organic layer structure has been displayed in the case of uracil [23,24], uridine [14], and viologens [25,26].

The fundamental adsorption studies have benefitted significantly from developing *in situ* techniques that provide insights into the balance of intermolecular interactions [7,27]. Techniques such as scanning tunnelling (STM) and atomic force microscopy (AFM) can provide submolecular resolution in imaging, making the detection of small changes in adsorbed structures possible. These studies have allowed visualising the structures of uracil [28], camphor [29], benzoic acid [30], viologens [26,31], and other organic compounds [32], facilitating a clearer understanding of the phase transitions and dynamics associated with adsorbed layers. Combined with other techniques such as surface-enhanced infrared absorption (SEIRAS) and Raman spectroscopy, density functional theory (DFT) calculations, and molecular dynamics (MD) simulations, a multi-faceted picture of the interfacial processes and adsorption kinetics can be gathered [33–39].

In the given thesis, 4,4′-bipyridine (4,4′-BP) has been used for studying the adsorption at electrode | ionic liquid. 4,4′-BP can bond with the electrode as well as interact with the electrolyte and other molecules in various ways. Depending on the electronic and crystallographic properties of the chosen electrode, the 4,4′-BP forms highly ordered structures, where the molecules have adsorbed to the surface with the ring plane parallel [38,40–42] or ring plane perpendicular with N-atoms pointing towards [43–45] or parallel [38,42] to the electrode surface. The adsorbed structures have been demonstrated to be influenced by the applied potential or the used electrolyte [38,42,44]. These studies highlight the interplay between different interactions that lead to the formation of two-dimensional condensed ordered structures on the electrode surface, such as the dispersion, Coulomb, and π-interactions, along with hydrogen bonding.

4.2. Ionic Liquids

Room temperature ionic liquids (ILs) are a class of compounds that have been under intense study since the 2000s due to their large structural variability and peculiar properties. Although Walden described the first IL in 1914 [46], the rapid growth of interest was followed by synthesising ILs that are stable in air and moisture [47]. ILs typically have a melting point below 100 °C while consisting of ionic species – large organic cations and organic or inorganic anions. A typical IL cation is based on central imidazole, pyridine or quaternary ammonium group modified with alkyl side chains (see Figure 1). At the same time, the anions are made up of various structures, such as halide, tetrafluoroborate, hexafluoro-

phosphate, acetate, or alkylsulphate ions [48]. The relatively low melting point of ILs is associated with the large size and flexibility of ions, favouring the liquid state due to small lattice enthalpies and large entropy changes [49].

The broad structural variability and the possibility of combining different ions allow for refining the properties of ILs for task-specific applications. For example, the melting point of IL that contains cations with short alkyl side chains can be lowered by increasing the side chain length or altering the degree of branching [50]. Alternatively, the melting point can be lowered by pairing the selected cation with an anion with a larger molar volume and mass. The properties of ILs can be further enhanced by mixing different ILs. This is utilised in increasing the capacitive properties of electrode–IL interface by adding ILs with halide anions to common ILs (such as 1-ethyl-3-methylimidasolium tetrafluoroborate ($EMImBF_4$) and 1-ethyl-3-methylimidazolium bis(trifluoromethylsulfonyl)imide) through the adsorption and reversible charge transfer processes associated with halide ions [51–53].

ILs are investigated as electrolytes in energy storage and conversion devices such as batteries, fuel cells, dye-sensitised solar cells, and supercapacitors. [54] The large-scale interest is carried by their remarkable electrochemical stability, allowing the application of larger voltage, the high number of ions, contributing to charge transport and storage, and low vapour pressure, preventing the electrolytes from drying and easing their handling. Due to the tunability of properties and large structural variety, ILs are used in organic synthesis and catalysis [55–57]. They have been studied for biomass and CO_2 conversion to value-added chemicals, where ILs act as solvents and catalysts [54,58]. Furthermore, ILs have been investigated for extracting various organic compounds [59,60] and metal ions [61].

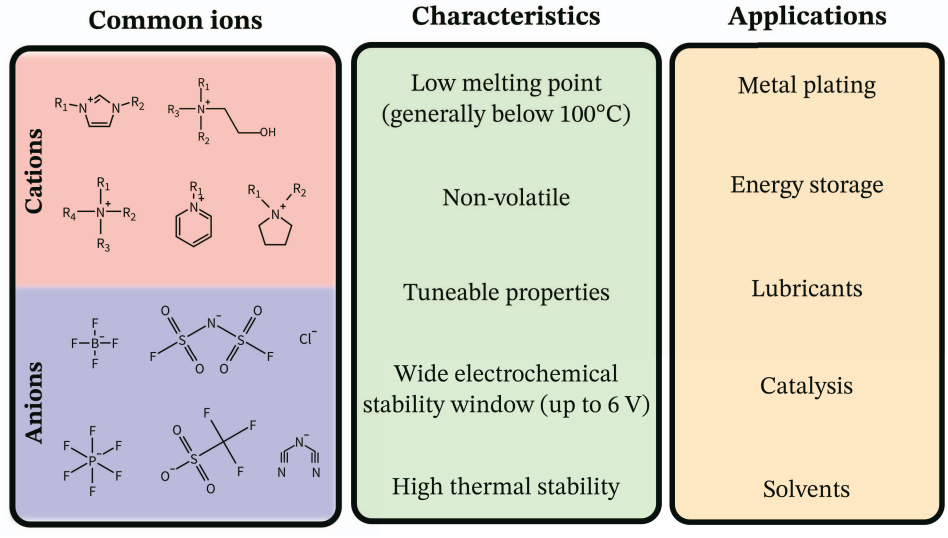

Figure 1. Schematics of common ionic liquid ions, properties, and applications.

The ILs are also attractive from a fundamental perspective. As they consist of ionic species, the Coulomb interactions between the ions are significant. Thus, ILs have higher densities than similar molecular compounds due to coulombic compaction that decreases the molar volume [62]. Along with the establishment of charge networks due to long-range charge oscillations, this gives rise to increased viscosity and the formation of aggregates inside the liquid [63,64]. However, only 15–25% of ions can be considered free, while others are bound to larger clusters. This leads to conductivities that are smaller than expected and comparable to other conventional electrolytes [65].

At charged interfaces with solid materials (such as electrodes), ILs form ordered ionic layers due to strong charge–charge correlations and the overcompensation of the electrode′s charge (overscreening). Numerous computational studies have characterised it using MD simulations [66–70]. The formation of a layered structure has also been demonstrated with AFM [71] and surface force apparatus [72]. Thus, the interfacial properties and structure of ILs differ significantly from other common aqueous and organic electrolytes. To highlight this, the widely-used Gouy–Chapman theory [73,74] of diffuse ion layer for dilute electrolytes does not hold in ILs. Therefore, other mean-field theories, such as Kornyshev and Goodwin–Feng–Kornyshev models, have been derived [75–77]. In contrast with the Gouy–Chapman, these theories have proposed that the capacitance–potential dependence at around the potential of zero charge (PZC) has a bell (with a maximum at PZC) or camel shape (with a local minimum at PZC between two maximums) depending on the compacity of the IL. In addition, models by Bazant *et al.* [78] and Souza *et al.* [79] have moved beyond the mean-field theory to describe the strong charge–charge correlations, IL layered structure, and overscreening phenomenon.

The peculiar capacitance–potential dependence has also been demonstrated with computational simulations of IL interfaces [66,80–82]. Unfortunately, a conclusive agreement on the shape of capacitance–potential dependence has not been reached experimentally due to the frequency dependence of capacitance measured with EIS and the significant impact of impurities on the capacitance values [83].

In the experiments and simulations that comprise the given thesis, two ILs were used. The first studied IL, $EMImBF_4$, is characterised by a wide electrochemical stability potential region, moderate viscosity, and good molar conductivity. Numerous experimental [84–87] and computational studies [88–90] have investigated its interfaces with various electrodes to describe its interfacial structure and capacitance at various electrodes. Therefore, as the properties of the electrode | $EMImBF_4$ are well-defined, there is a solid foundation for describing the organics′ adsorption processes from IL electrolyte on the example of 4,4′-bipyridine at different electrode surfaces [91–93]. The second IL, 1-butyl-3-methylimidazolium hexafluorophosphate ($BMImPF_6$), is also widely studied [66,94–97]. It has a wider electrochemical stability region, higher viscosity, and lower melting point than $EMImBF_4$ [98]. In this thesis, $BMImPF_6$ is used to computationally study the IL interfacial structure and describe the capacitance–structure relation.

4.3. Single Crystal Electrodes

The processes and reactions occurring on the electrode′s surface are influenced by its structure and properties. For example, the electrode′s charge at the selected potential depends on the surface structure, affecting the kinetics of adsorption and surface reactions [99,100]. Single crystals are solids with a uniform arrangement of atoms. In contrast with polycrystalline electrode materials, where the arrangement of atoms may suddenly change, single crystal surfaces have a highly regular composition and long-range structure. Thus, using single crystals reduces the complexity of collected experimental results and facilitates a better understanding of the interfacial processes. In the given thesis, Bi(111), Sb(111), and Cd(0001) single crystal surfaces have been used in the conducted experiments. These surfaces are stable and do not undergo surface reconstruction processes, which could hinder the formation of highly ordered adsorbed monolayer structures and complicate the analysis of surface processes. Furthermore, the IL structure at Au(001) and graphene surfaces were studied using MD simulations.

Bismuth is a Group 15 semimetal considered green electrode material due to its non-toxic character [101,102]. It has a rhombohedral crystal structure, shown in Figure 2, with lattice parameters a = 4.546 Å and c = 11.862 Å [103]. In a Bi crystal, each Bi atom has three closest equidistant neighbouring atoms and three next to closest equidistant neighbours, resulting in a bilayer structure with the intralayer spacing of b = 1.594 Å. The surfaces of Bi(110), Bi(100), and Bi(111) have metallic surface states, leading to more metallic nature than bulk Bi [104–106]. This is crucial when considering the use of Bi in small systems such as thin films and clusters.

Antimony like bismuth is a Group 15 semimetal with a semimetal-semiconductor transition in thin films. Their crystal lattices are very similar as the parameters of antimony lattice (a = 4.308 Å and c = 11.274 Å) [107] differ from bismuth very slightly while having the same crystal and bilayer structure (b = 1.51 Å). The electronic structure of Sb(111) is similar to that of Bi(111), with quantitative differences in electron carrier numbers [108]. Both Bi and Sb crystals can be cleaved along the (111) plane due to the weaker bonds between the bilayers than inside the bilayer. Thus, the Bi(111) and Sb(111) surfaces are not expected to undergo reconstruction, as the crystal consists of weakly bonded stacks of bilayers, while intralayer bonding is predominantly covalent. Previous electrochemical studies of interfaces with Bi(111) and Sb(111) surfaces have verified high surface stability using various methods [109–112].

Cadmium is a Group 12 metal that has been used in electronic devices and corrosion protection. In atmospheric conditions, cadmium oxidises quickly, forming a thin protective oxide layer on the metal′s surface. Unlike antimony or bismuth, it has a hexagonal close-packed structure with lattice parameters (a = 2.973 Å and c = 5.6073 Å) [113]. Each cadmium atom has 12 closest equidistant neighbouring atoms in this crystal structure. No surface reorganisation processes have been reported by previous studies within the studied potential ranges [92,114,115].

Gold is a noble metal of Group 11 that has been widely studied as an electrode material. It has a face-centred cubic crystal structure with lattice parameter a = 4.07 Å [116]. Although attractive due to its inertness, the low index surfaces of gold have been shown to undergo surface reconstruction: Au(111) to herring-bone structure [117], Au(001) to quasihexagonal structure [118], while Au(011) corrugates [119].

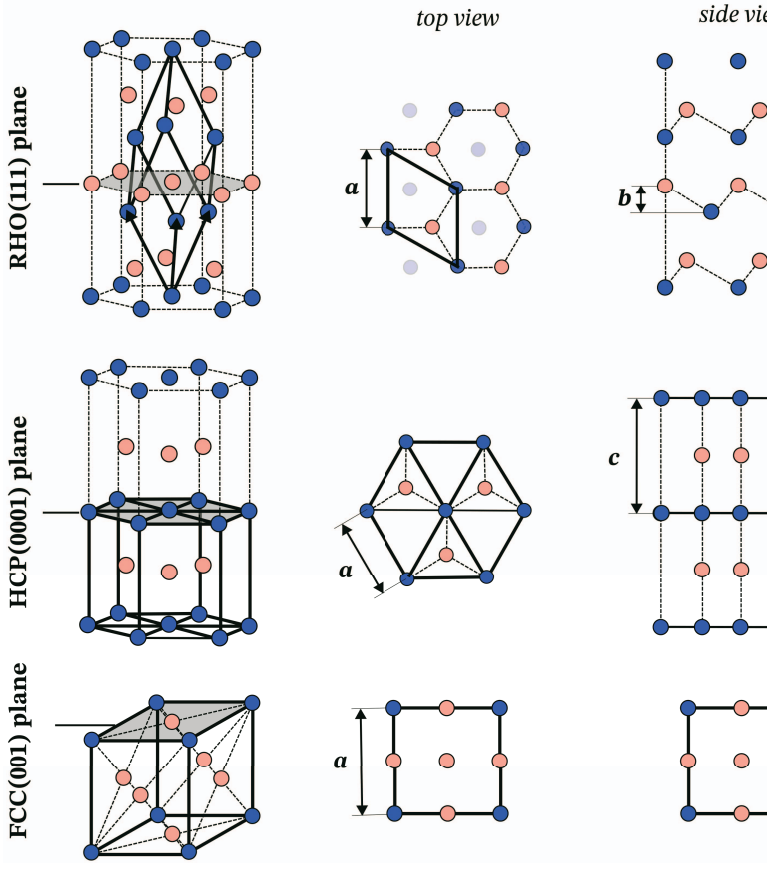

Figure 2. Rhombohedral (RHO) (in a hexagonal representation), hexagonal close-packed (HCP), and face-centred cubic (FCC) structures with top and side views.

4.4. Cyclic Voltammetry

Cyclic voltammetry is a linear potential sweep technique where the applied potential (E) is cycled at a constant scan rate (v) over a given potential range while measuring the current density (j). This method allows the investigation of molecular species′ reduction and oxidation processes through electron transfer. It is a common starting point of an electrochemical investigation, as it allows for the identification of the potentials where redox processes occur.

In a typical CV measurement, when the electrode′s potential is first gradually increased, the increase of current points to an oxidation process. During the oxidation, the concentration of reduced species decreases while oxidised species increases near the electrode. This leads to the formation of a diffusion layer at the interface, where the concentrations of electroactive species near the electrode differ from their bulk values. The current decreases when the reduced species at the electrolyte near the electrode′s surface are depleted while the diffusion layer grows. If the process is reversible, switching the potential cycling direction to the negative direction leads to a reduction process, reversing the oxidation. The choice of potential scan rate (v) is important, affecting the diffusion layer thickness. Moreover, the scan rate allows for the characterisation of interfacial processes.[120]

The studied electrode processes can be divided into diffusion-limited, adsorption-limited, and charge-transfer-limited. In diffusion-limited processes, the reaction kinetics is dictated by the diffusion of electrochemically active species from the bulk solution. For this process, the peak current (j_p) increases with the square root of the sweep rate according to the Randles–Sevcik equation:

$$j_\mathrm{p} = 0.446nFAC_\mathrm{o}\sqrt{\frac{nFvD_\mathrm{o}}{RT}}, \quad (1)$$

where n is the number of transferred electrons, A is the surface area of the electrode, T is temperature, R is the molar gas constant, F is the Faraday constant, C_o and D_o are bulk concentration and diffusion coefficient of the reduced species, respectively. The difference between the oxidation and reduction current peak E values is expected to be 57 mV at 298 K for a reversible diffusion-controlled one-electron transfer process.[121]

The occurring process is adsorption-limited if the reactions are related to the species adsorbed onto the electrode′s surface or confined close to the electrode. Then, the measured current increases linearly with the sweep rate as the peak current response is characterised by:

$$j_\mathrm{p} = \frac{n^2F^2}{4RT}vA\Gamma, \quad (2)$$

where Γ is the amount of adsorbed species on the electrode′s surface.

The process is limited by charge transfer when the rate of electron exchange between the electrode and the electrochemically active species is sluggish. For a given process to overcome the high barrier to electron transfer, a larger applied potential is necessary to observe the oxidation/reduction reaction. These processes are characterised by increased separation between the oxidation and reduction peak E values. Thus, charge-transfer limited processes, while in a chemical sense reversible, are considered electrochemically irreversible.[122]

4.5. Electrochemical Impedance Spectroscopy

Electrochemical impedance spectroscopy is a technique that provides insights into the kinetics of interfacial processes. Its relevance lies in the ability to differentiate between various electrochemical and physical processes at the electrode-electrolyte interface. This is achieved by deconvoluting a complex system into individual processes with different time constants, simplifying the analysis. The method has widespread use in studies focusing on adsorption, electrical double layer formation, corrosion, chemical sensing, energy conversion, and storage.[123]

EIS is based on the perturbation of an electrochemical system by applying a small sinusoidal signal over a wide range of alternating current frequencies (f) while monitoring the response to the perturbation. If an alternating potential $E(t) = E_m\sin(\omega t)$ is applied to an electrode, then the measured current is $j(t) = j_m\sin(\omega t - \theta)$, where E_m and j_m are the amplitudes of potential and current. The phase difference between E and j is denoted by θ, while ω is the angular rotation velocity, related to f by $\omega = 2\pi f$. The impedance (Z) is then defined as:

$$Z = \frac{j}{E} = |Z|e^{i\theta} = |Z|[\cos(\theta) + i\sin(\theta)] = Z' + iZ'', \quad (3)$$

where $i = \sqrt{-1}$, $|Z|$ is the impedance modulus, while Z' and Z'' are the real and imaginary parts of the impedance, respectively. The phase difference θ depends on the interface′s characteristics. When the interfacial behaviour is governed by the electrolyte resistance or charge transfer reaction kinetics, $Z = R$, as $\theta = 0°$. In the case of purely capacitive behaviour (*i.e.*, the charging/discharging of an electrical double layer), $Z = -i/(2\pi fC)$, as $\theta = -90°$. Alternatively, if the diffusion of redox species to the electrode′s surface from the bulk is the limiting process, then $\theta = -45°$. Thus, the individual processes occurring on the electrode′s surface can be related to the elements of an electrical circuit. [124]

These elements can be combined into a complex equivalent circuit of individual processes with different time constants, modelling the interfacial response. For example, an ideally polarisable electrode is characterised by no charge transfer across the interface. Therefore, the given interface can be modelled as a series combination of resistor and capacitor, related to the solution resistance and double layer capacitance, respectively.[125] The interface that contains electroactive species can be described by Randles circuit, where the charge transfer and diffusion are represented by the resistor and Warburg element, connected parallel to the capacitor, describing the double layer capacitance. More complex circuits can be obtained by fitting experimental data [94,126,127]. Studying the interfacial processes over a wide range of frequencies is necessary as slow interfacial processes can be studied at low frequencies (*e.g.*, diffusion). In contrast, fast processes (*e.g.*, double layer charging) can be investigated at high frequencies.

4.6. Scanning Tunnelling Microscopy

Scanning tunnelling microscopy is a versatile method that allows surface topography imaging at atomic resolution. It has contributed significantly to the development of nanotechnology and surface sciences, where the detailed knowledge of surface structures and active sites and the interactions of the various system components on the electrode′s surface is vital.[128]

STM is based on the quantum tunnelling effect, where due to the existence of delocalised electron wave functions, a current can flow between the electrodes that are separated by a few Ångstroms if a bias voltage is applied. The tunnelling current (j_{tunnel}) is related to the distance between the electrodes (d) as $j_{\text{tunnel}} \sim e^{-2\kappa d}$, where κ is the decay constant for the wave functions. Thus, even a small increase of d decreases the j_{tunnel} by order of magnitude, providing high sensitivity in the vertical direction. The STM images are obtained by scanning the sharp metal tip over the surface. The lateral resolution of the STM image depends on the tip′s shape and sharpness, which determines how different points of the tip contribute to the j_{tunnel}. Ideally, a single atom should terminate the STM tip, which is almost unachievable in practice. Furthermore, the tip needs to be made up of hard materials to prevent damage to the tip when it crashes into the surface. Thus, metals such as tungsten or platinum–iridium wires are commonly used to prepare the STM tip.[129]

The exponential dependence of j_{tunnel} on d requires that the movement of the STM tip is precisely controlled. This is achieved using piezoelectric ceramic actuators that can expand or retract depending on the voltage generated by the electronic control system. The response of piezoelectric scanners to the applied voltage is linear, being a few nanometers per applied voltage. Therefore, lateral scan widths up to 10 μm can be achieved by applying several hundred volts to the scanner.

The scanning of the tip over the surface is done in either constant current or constant height mode. In constant current mode, the j_{tunnel} is kept steady during scanning while the scanner adjusts the distance between the tip and the surface to maintain j_{tunnel}. These distance adjustments are registered. This mode is suitable for any type of surface topography. In constant height mode, the scanner does not adjust the tip's distance. Thus, the change of j_{tunnel} is monitored, as the d changes due to the step edges and other surface features. Therefore, only very smooth surfaces can be measured using this mode.[129,130]

In addition to visualising the surface topography, STM allows studying the processes and reactions occurring at the solid–liquid interface *in situ*. The development of electrochemical scanning tunnelling microscopy (EC–STM) has made it possible to investigate the impact of potential change to processes such as adsorption, metal deposition, and corrosion. In EC–STM, illustrated in Figure 3, the electrochemical three-electrode cell is combined with STM. The tip and working electrode potentials are controlled independently by bipotentiostat with respect to the reference potential in this configuration. As the measuring tip acts as an electrode, the electrochemical processes occurring on its surface can affect

the measured j_{tunnel} and create noise. To minimise this effect in polar liquids, the measuring tip must be coated with insulating wax or organic glue, leaving only the apex of the tip uncovered. EC–STM also requires the preparation of well-defined sample surfaces reproducibly, which is achieved by flame annealing, electrochemically polishing/etching or cleaving single crystal electrodes.[131]

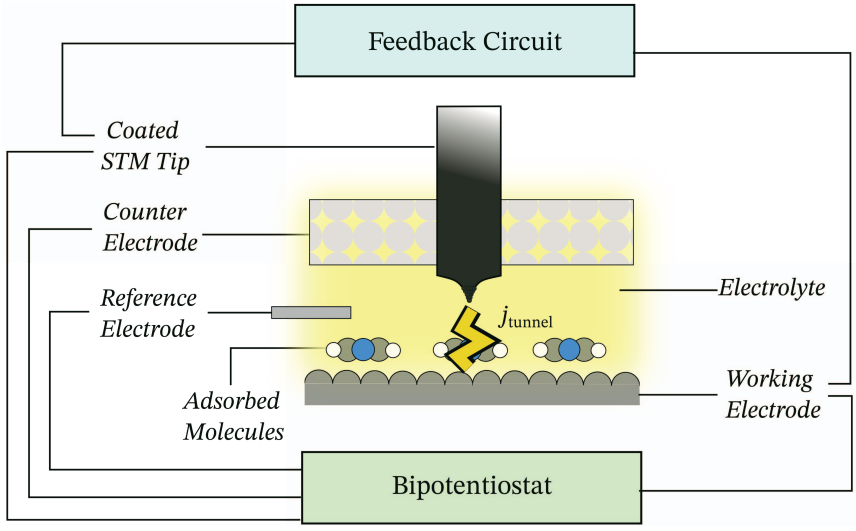

Figure 3. Schematic illustration of electrochemical scanning tunnelling microscopy (EC–STM) setup scheme.

4.7. Molecular Dynamics Simulations

Molecular dynamics is a computational method that evaluates how the simulated system evolves over time according to Newton′s second law. It can provide atomic-scale insights into the description of structure–property relationships or guide the design of novel materials. Thus, it has been applied to studies focusing on energy storage [4], drug discovery [132], and materials science [133].

A MD simulation is based on a force field – a function describing the interatomic interactions of the given system. The choice of force field is crucial as it determines the accuracy of the MD simulation. The potential energy of a studied system is evaluated as a sum of different terms corresponding to the distortion of the molecule′s bonds or non-bonded interactions [134]. In molecular dynamics, the description of electrons is avoided, while the molecules and ions are considered to consist of charged atoms connected by bonds with varying length and stiffness. Thus, separate terms describe the bond stretching, change of bond angle, and rotations around the bond. The electrostatic interaction between the atoms is evaluated using the Coulomb potential when the atoms are considered point charges. For an accurate description of non-bonded interactions, the effects that arise due to the interactions or distortions of electron clouds, such as van der Waals repulsion

or attraction, need to be included. These terms can be estimated using the Lennard-Jones potential:

$$U_{\mathrm{LJ}} = 4\varepsilon_{\mathrm{LJ}}\left[\left(\frac{\sigma_{ij}}{r_{ij}}\right)^{12} - \left(\frac{\sigma_{ij}}{r_{ij}}\right)^{6}\right], \tag{4}$$

where the distances between atoms *i* and *j* at zero potential and evaluated potential are σ_{ij} and r_{ij}, respectively. The depth of the potential is given by $\varepsilon_{\mathrm{LJ}}$. More advanced polarisable force fields also account for the distortion of the electron density due to the electric field, which has a notable effect in the case of high ionic concentrations or at charged interfaces [135].

Numerous empirical force fields such as OPLS–AA [136], ReaxFF [137], CHARMM [138], and GAFF [139] have been parametrised for various atom types and compounds. Force fields are fitted to reproduce the experimental physical properties or computational data from density functional theory calculations. More recently, machine learning methods have been incorporated into constructing force fields. In machine learning force fields, underlying structure-property relations are learned by fitting the energy and forces of *ab initio* simulations, which allows for avoiding the fitting of obtained data to chosen potential functions.[140]

The force field allows estimating the forces exerted on a particle at a given time t_1 by other system constituents. Using Newton′s law of motion, the particle′s position can be estimated at a time t_2 by knowing the particle′s position, velocity and acceleration through numerical integration. The difference between t_1 and t_2 is known as the timestep. The chosen timestep must be smaller than the fastest movements in the system to avoid the instability caused by numerical integration, and it is typically around 1 to 2 fs. MD simulations consist of a large number of iterations, each moving the system one timestep at a time. These iterations create a trajectory describing the evolution of the system over time.

The MD simulations of electrode–electrolyte interfaces are relevant as there are limited options for describing the local electrolyte structure changes experimentally *in situ*. The simulations thus can provide valuable information on the interfacial structure changes and explain experimental observations. Including the electrode increases the complexity of simulations as the interactions between the electrode and the electrolyte and the charging of the electrode need to be accurately described. The charging of the electrode can be achieved by assigning a charge to each electrode atom [141], applying an electric field perpendicular to the electrode′s surface [82] or defining a potential between two electrodes [142]. The constant potential method facilitates non-uniform charge distribution on the electrode′s surface. Also, in experimental measurements, the potential rather than the electrode′s charge is controlled. Despite these advantages, the constant charge or field methods are still applied due to their smaller computational complexity [135].

4.8. Density Functional Theory

Density functional theory is a powerful quantum mechanical method for studying the relationship between structure and property at the atomic scale. It has found widespread use in studies focusing on the electronic properties, adsorption behaviour and reaction mechanism of novel interfaces, materials, and molecules important in fields such as catalysis and energy storage and conversion [143–148]. The method is based on quantum mechanics, describing the electronic structure of the system. Thus, it does not require the existence of a parametrised force field. At the same time, the advantage comes with the cost of increased computational complexity, limiting the scale of studied systems.

DFT is based on the concept that the electron density of a system determines its ground-state electronic energy. Although estimating the energy from only the system′s total electron density without paying attention to orbitals is appealing, this approach has not performed well. Thus, most DFT calculations are currently based on the Kohn–Sham scheme [149]. In this scheme, the electrons fill single-particle non-interacting orbitals to estimate electronic kinetic energy. However, as the electrons do interact, the energy of a studied system in this scheme is composed of non-interacting kinetic energy, electrostatic coulombic interactions, and an exchange–correlation energy. The last term accounts for the difference between non-interacting and interacting system′s kinetic energies, self-interaction correction, and other effects, such as exchange and correlation, arising from repulsion between like-spin electrons and its influence on electron distribution.

The explicit form of exchange–correlation energy is not known, while there are approximations to this functional which determine the accuracy of calculations [150]. The simplest is local density approximation, which describes the electrons as uniform gas. Although resembling the model of idealised metal, it is unsuitable for describing atoms and molecules, which are characterised by notable variances in electronic densities. More complicated approximations account for the charge density gradient to account for the non-homogeneity of the electron density (generalised gradient approximation) and combine a fraction of Hartree–Fock′s exchange energy with DFT functionals (hybrid functionals). One widely used generalised gradient approximation for studying materials and interfaces is the non-empirical Perdew–Burke–Ernzerhof (PBE) functional [151], also applied in the given thesis. The functional has shown reasonable performance in estimating electronic properties while being known to underestimate the surface energy of material [152,153].

Another troublesome aspect of using the approximations of exchange–correlation functionals is the inclusion of dispersion interactions. These interactions are not accounted for in semi-local or hybrid density functionals, although they are important in the adsorption of organic molecules and forming organic layers [148]. Thus, correction schemes have been developed to take dispersion into account. The schemes such as DFT–D3 [154], DFT–D4 [155] or vdW^{surf} [156] evaluate the contribution of van der Waals interactions after the convergence of electronic structure estimation using analytical expressions. These corrections have allowed better agreement between the calculated and experimental structures and established energies.[157,158]

5. EXPERIMENTAL

5.1. Simulations of Electrode | Ionic Liquid

In the case of simulations of the Au(100) | $BMImPF_6$, the studied model was made up of 2 electrodes, which consisted of 4 layers of Au sheets with an area of 4.0×4.0 nm^2. The electrodes were situated at the opposing faces of the simulation box and separated by 16 nm. The space between them was filled with 720 ion pairs of $BMImPF_6$ using Packmol [159]. The composed system was subjected to the steepest descent energy minimisation followed by 0.1 ns and 10 ns equilibration runs with 0.5 fs and 1 fs timesteps at 450 K, respectively. Then, the charging of the electrode was achieved by applying an electric field perpendicular to the electrode′s surface. The applied electric field corresponded to surface charge density (σ) values of 0, 2, 4, 6, 8, 10, 12,14, 16, 20, 24, 28, 32, 36, 40, 44, 48, 52, 56, 60, 64, 68, 72, 76, 78, 82, 84, or 100 μC/cm^2. The applied electric field was equal to $\sigma/(\epsilon\epsilon_0)$, where ϵ_0 and ϵ corresponded to a vacuum permittivity and a relative permittivity of 1.6, accounting for the polarisation and charge transfer effects [160], respectively. The initial charging of the interface was achieved during a 4 ns simulation. The analysed data was collected during a 20 ns production run in the *NVT* ensemble at 450 K.

A similar model was constructed to study the graphene and $EMImBF_4$ interface at different temperatures. The simulation box consisted of two graphene sheets with an area of 2.98×2.95 nm^2 at opposite sides. The distance between the electrodes was 9.5 nm. The space between the electrodes was filled with 288 $EMImBF_4$ ionic pairs using Packmol. The constructed model′s energy was minimised and equilibrated similarly to the Au(100) | $BMImPF_6$ model. The system was then annealed at 800, 900 or 1000 K for 1 ns to produce 3 replicas. Then, the electrodes were charged by applying an electric field corresponding to σ value of 0, 1, 2, 3, 4, 5, 6, 7, 8, 9, 10, 12, 16, 20, 24, 28, 32, 36, 40, 44, 48, 52, 56 or 70 μC/cm^2 and cooled down to 300, 350, 400, or 450 K. The charging and cooling steps were both 10 ns long. The data was collected for each studied temperature during a 10 ns long production run simulation in the *NVT* ensemble.

The molecular dynamics simulations were performed using the GROMACS 5.1.4 or 2019.5 software [161] and the NaRIBaS framework [162]. The parameters for the description of $BMImPF_6$ and $EMImBF_4$ ionic liquids were taken from the refinements of the OPLS–AA force field that were developed for ionic liquids by Lopes *et al.* and Sambasivarao *et al.* [163,164]. Lennard-Jones parameters for gold and carbon atoms in electrodes were taken from [136,165]. The simulations used the leapfrog algorithm to integrate motion equations and velocity rescaling thermostat to manage the model′s temperature [166,167]. Periodic boundary conditions were applied in directions perpendicular to the electrode′s surface. The graphene′s density of states was estimated using GPAW 21.6.0 software [168]. The plane-wave method with a cut-off of 800 eV, PBE exchange–correlation functional, and 40×40×1 Monkhorst–Pack k-point grid was applied in the calculations [151,169]. The evaluated system consisted of a graphene sheet

with an area of 0.21 nm^2 surrounded by a 1 nm thick vacuum layer perpendicular to the graphene sheet.

From the collected MD simulation results, the electrostatic potential (ϕ) at a distance z from the electrode was evaluated as:

$$\phi(z) = -\frac{z\sigma}{\epsilon\epsilon_0} - \frac{1}{\epsilon\epsilon_0}\int_0^z (z - z')\rho_q(z')dz', \quad (5)$$

where $\rho_q(z')$ is the averaged ionic liquid′s charge density at a distance z' from the electrode′s surface and ϵ_0 vacuum permittivity. The potential drop (ϕ_{IL}) at the interface was estimated as $\phi_{\mathrm{IL}} = \phi_{\mathrm{electrode}} - \phi_{\mathrm{electrolyte}}$, where $\phi_{\mathrm{electrode}}$ and $\phi_{\mathrm{electrolyte}}$ correspond to ϕ at the electrode′s surface and in the bulk electrolyte. Furthermore, the estimated ϕ_{IL} values were shifted by the PZC in the following analysis: $E = \phi_{\mathrm{IL}} - \mathrm{PZC}$. The interfacial capacitance (C) was evaluated as $C = \mathrm{d}\sigma/\mathrm{d}E$ by interpolating the obtained σ–E dependence, which was smoothed using the Hamming window function with a 12 μC/cm^2 size.

To account for the shifting of the Fermi level in the case of graphene electrode, the interfacial capacitance was corrected with electrode quantum capacitance (C_{Q}). At a given σ, the graphene′s electric potential (ϕ_{Gr}) was estimated as the shift of Fermi level $\phi_{\mathrm{Gr}} = (\varepsilon - E_{\mathrm{F}})/e$, where e is the elementary charge, ε and E_{F} are the Fermi levels of an electrode with charge density σ and 0 μC/cm^2, respectively. Thus, the overall interfacial potential drop (E_Σ) at given σ was $E_\Sigma = E + \phi_{\mathrm{Gr}}$. The corrected interfacial capacitance (C_Σ) was evaluated similarly to capacitors in series:

$$\frac{1}{C_\Sigma(E_\Sigma)} = \frac{1}{C(E)} + \frac{1}{C_Q(\phi_{Gr})} \quad (6)$$

5.2. Bilayer Model

The bilayer model provides a semi-quantitative explanation for the capacitance–structure relation observed in molecular dynamics simulations. The given model is simplistic, relying only on the first two ionic liquid layers to explain the structural response to the applied electrode′s charge σ. In the bilayer model (see Figure 4), the first IL layer overscreens the electrode′s charge σ. In contrast, the second layer restores the electroneutrality of an electrical double layer by holding the charge λ. Thus, the potential drop in the bilayer model can be expressed as:

$$\phi_{\mathrm{BL}} = \frac{l\sigma - \delta\lambda}{\epsilon\epsilon_0}, \quad (7)$$

where the l and δ are the distances from the electrode′s surface to the first ionic liquid layer and from the first ionic liquid layer to the second ionic layer, respectively.

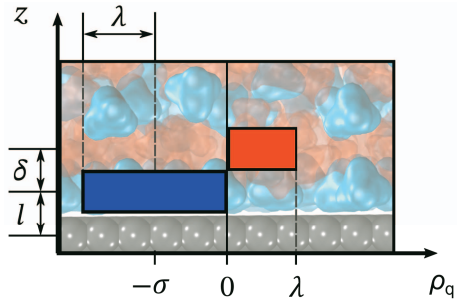

Figure 4. Snapshot of graphene–ionic liquid interface, illustrating the parameters of bilayer model.

The interfacial capacitance can be then expressed as:

$$C = \frac{d\sigma}{dE} \approx \frac{d\sigma}{d\phi_{\mathrm{BL}}} = \frac{\epsilon\epsilon_0}{l} + \frac{\epsilon\epsilon_0\phi_{\mathrm{BL}} - \delta\lambda}{l^2}\frac{dl}{d\phi_{\mathrm{BL}}} + \frac{\delta}{l}\frac{d\lambda}{d\phi_{\mathrm{BL}}} + \frac{\lambda}{l}\frac{d\delta}{d\phi_{\mathrm{BL}}}, \tag{8}$$

which can be further simplified when considering the position of the first ionic liquid layer constant ($l = const.$) and the first term equal to Helmholtz layer capacitance $C_{\mathrm{H}} = \epsilon\epsilon_0/l$:

$$C = \frac{d\sigma}{d\phi_{\mathrm{BL}}} = C_{\mathrm{H}} + \frac{\delta}{l}\frac{d\lambda}{d\phi_{\mathrm{BL}}} + \frac{\lambda}{l}\frac{d\delta}{d\phi_{\mathrm{BL}}}, \tag{9}$$

These expressions allow the rationalisation of the observed simulation data by focusing on the Helmholtz layer capacitance (C_{H}), the change of overscreening ($\mathrm{d}\lambda/\mathrm{d}\phi_{\mathrm{BL}}$), and the formation of distinct ionic layers ($\mathrm{d}\delta/\mathrm{d}\phi_{\mathrm{BL}}$).

5.3. Studies of Electrode | 4,4'-bipyridine and IL Mixtures

5.3.1. Electrochemical Impedance Spectroscopy and Scanning Tunnelling Microscopy Measurements

To study the processes occurring at the interfaces between chosen single crystal electrodes and 4,4′-bipyridine (Thermo Scientific Acros, purity 98.0%, anhydrous) dissolved in $EMImBF_4$ (Sigma–Aldrich, for electrochemistry, purity ≥99.0%, ≤200 ppm water), the investigated solutions were prepared and measurements conducted in the glove box ($H_2O < 0.3$ ppm, $O_2 < 0.2$ ppm). All *in situ* STM and EIS measurements were carried out in a classical three-electrode cell. Pt net was used as a counter electrode, and Ag | AgCl was directly in contact with the ionic liquid as a reference electrode. The studied single crystal electrode served as a working electrode and was electrochemically polished or cleaved before each experiment. Cd(0001) surface was polished using a hot 1:1 solution of concentrated phosphoric acid and Milli Q^+ water. For EIS measurements Bi(111)

and Sb(111) working electrodes were polished in a saturated KI (Sigma–Aldrich, BioUltra, purity ≥99.5%) + 0.5% HCl (Merck, Suprapur, 30% solution) aqueous solution. During the EC–STM experiment preparation, the Bi(111) or Sb(111) surfaces were cleaved to provide an atomically smooth substrate surface.

In the case of CV and EIS measurements, the prepared working electrode was introduced into the solution at potentials $E = -0.6$ V (for Sb(111) and Bi(111)) or $E = -1.4$ V (for Cd(0001)). After the initial stabilisation of current density (j) to a constant value, CV and EIS measurements were carried out using Autolab PGSTAT204 with FRA32M EIS module and Nova 1.10 software package. A single *ac* sine wave with an amplitude of 0.005 V was used in EIS measurements. The frequency (f) range applied was from 0.1 Hz to 10000 Hz with 15 frequencies per decade. Interfacial capacitance was estimated using relation $C = -(Z''2\pi f)^{-1}$ under the assumption of a non-compensated resistor and a capacitor connected in series.

The EC–STM measurements were conducted using a PicoSPM™ molecular imaging system in the constant current mode. The STM tips were made by electrochemically etching tungsten wire with 5 M KOH (Sigma–Aldrich, *puriss. p.a.*) solution and insulated with Apiezon™ wax. The prepared tips were introduced to the electrolyte solution at similar potentials as in EIS and CV measurements. STM images were analysed and filtered using Gwyddion data visualisation and analysis software [170].

5.3.2. Density Functional Theory Calculations of Adsorbed Structures

The adsorption of 4,4′-BP at Bi(111) and Sb(111) single crystal electrodes was further investigated with DFT calculations. The lone 4,4′-BP adsorption was studied at the top, bridge, hollow 1, and hollow 2 sites with the molecule′s ring plane parallel to the electrode′s surface, shown in Figure 5. The adsorption energy (E_{ads}) was investigated at each site at three different angles (0°, 45°, and 90° for the bridge adsorption site; 0°, 15°, and 30° for other sites) relative to the model surface normal. Thus, 12 structures of lone adsorbed 4,4′-BP molecule were estimated for each studied surface. The E_{ads} of molecule or ion adsorbed at electrode model surface was estimated as:

$$E_{\text{ads}} = \frac{E(\text{Me} \mid \text{Ads}) - E(\text{Me}) - nE(\text{Ads})}{n}, \tag{10}$$

where E(Me | Ads) and E(Me) correspond to the potential energies of electrode with and without adsorbate, respectively. The E(Ads) is the potential energy of an isolated adsorbate molecule or ion in the vacuum, and n is the number of adsorbed molecules/ions in the unit cell. The model surface consisted of 2 bilayers (4 layers of metal atoms in total), constructed using experimental lattice parameters [103,107]. The adsorption geometries were relaxed to a minimum, with atomic forces below 0.05 eV/Å, while keeping metal atoms fixed.

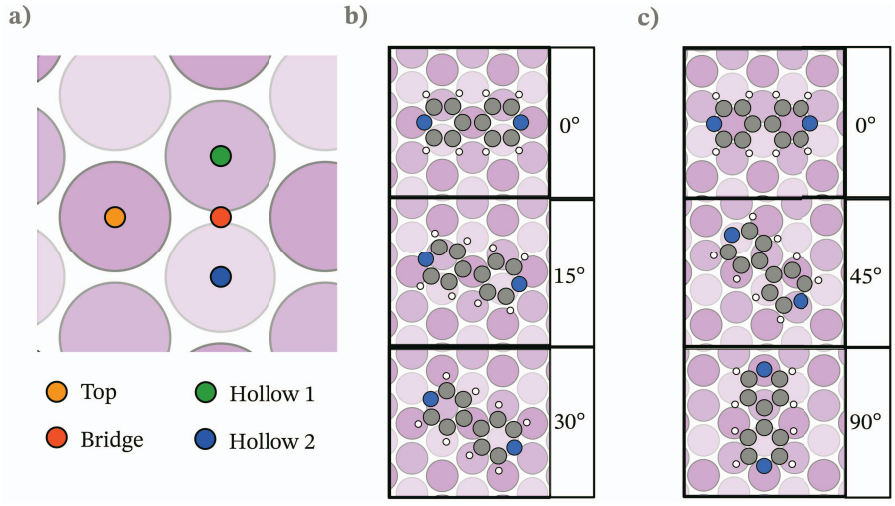

Figure 5. a) Studied adsorption sites at Bi(111) and Sb(111) surface; the investigated rotations of 4,4′-BP at **b)** the top, hollow 1, and hollow 2 sites; **c)** the bridge site.

Following that, dense adlayer structures of 4,4′-BP were evaluated to estimate the most probable adlayer structures. For this purpose, the Bayesian linear regression-based structure search algorithm SAMPLE [171] was used. To reduce the number of possible 4,4′-BP adlayer configurations, only 6 (for Bi(111)) or 8 (for Sb(111)) structures with the strongest lone 4,4′-BP adsorption were selected and used in the SAMPLE approach. The algorithm estimated the 4,4′-BP adlayer configurations with surface coverages between 1.3×10^{-10} mol/cm^2 to 2.7×10^{-10} mol/cm^2, containing up to 4 different lone adsorbed 4,4′-BP structures. In the case of 4,4′-BP adlayer on Bi(111), out of all generated structures, 300, 150, and 100 adlayer configurations were selected for the training, testing, and validation of the SAMPLE model, respectively. For 4,4′-BP adlayer on Sb(111), 290, 95, and 45 configurations were used in the above-mentioned datasets. The root-mean-square error for the validation set was 0.10 eV and 0.035 eV per adsorbed molecule for models describing 4,4′-BP structures adsorbed on Sb(111) and Bi(111), respectively.

To estimate the energy associated with the formation of coadsorbed $EMIm^+$ and 4,4′-BP adlayer, Bayesian Optimisation Structure Search (BOSS) [172] was used. The BOSS allowed determining the optimal position of $EMIm^+$ in the mixed adlayer by moving the $EMIm^+$ in the direction parallel to 4,4′-BP rows and rotating it around the axis perpendicular to the Bi(111) surface.

All DFT calculations were carried out with GPAW code in LCAO mode and ASE package [168,173,174]. Perdew–Burke–Ernzerhof (PBE) exchange–correlation functional, DFT–D4 dispersion correction, and dipole layer correction in *xy*-plane [151,175,176] were utilised. The Brillouin zone was sampled with a minimum density of 12 points/Å^{-1} and the real-space representation of the wave functions with a grid that had a spacing of 0.12 Å for the Bi(111) model. In the case of Sb(111) model, the respective parameters were 0.16 Å and 14.5 points/Å^{-1}.

6. RESULTS AND DISCUSSION

6.1. Capacitance–Structure Dependence of Au(001) | $BMImPF_6$

The MD simulations allow studying the ionic liquid′s interfacial behaviour in a significantly wider potential region than experimentally possible. Although the $BMImPF_6$ has an electrochemical stability window around 5 V [177], similar interfacial processes can occur at experimentally accessible potentials in other ILs. The capacitance–potential dependence of the Au(001) | $BMImPF_6$ interface, obtained by smoothing the simulations data with the Hamming window function, is shown in Figure 6. The *C*–*E* curve has a minimum at around the PZC and is surrounded by two peaks (I and II). Thus, the *C*–*E* can be described as having a ″camel″ shape in accordance with Kornyshev′s model [76]. At larger potentials, around 5 V and 14 V, two other capacitance peaks (III and IV) are visible. Previously, the MD simulations of Au(001) | $BMImPF_6$ by Hu *et al.* [66] and Sha *et al.* [178], reported contrasting camel- and bell-shaped *C*–*E* dependences, respectively. The bell-shaped *C*–*E* curve has also been shown experimentally by Lockett *et al.* [97] with *C* values around 7 – 9 μF/cm^2 in the studied potential range. Followingly, the capacitance peaks are linked to the changes in the IL interfacial structure and bilayer model.

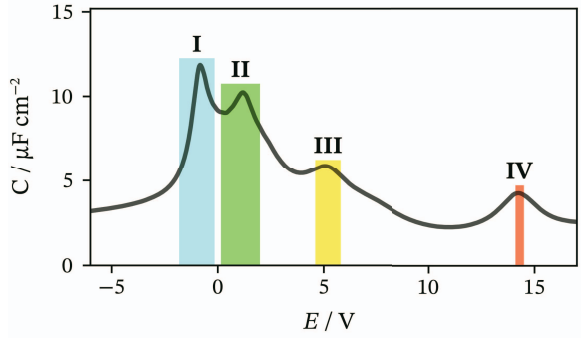

Figure 6. Capacitance (*C*) *vs.* potential (*E*) dependence of simulated Au(001) | $BMImPF_6$. The highlighted regions show the capacitance peaks that are related to the structural changes of ionic liquid.

The Peaks I and II near the PZC can be related to the formation of an ordered structure of alternatively charged ionic layer as the electrode obtains a charge. This structural reorganisation is illustrated in Figure 7a, where it can be seen that the ions with opposite charge to the electrode′s surface (counter-ions) are brought closer to the electrode′s surface, while the ions with the same charge (co-ions) are pushed further to the electrolyte. The layering of IL is also seen in the profiles of Figure 7b. At first, when the electrode is uncharged, the IL contains an almost equal number of both counter- and co-ions at various distances from the electrode.

When the potential is increased, the IL forms a layered interfacial structure with a fluctuating charge, although the layers contain both types of ions.

At larger potentials, the first and second IL layers consist of only one type of ions. Thus, around the potential regions of Peaks I and II, the change of ions between the first and second IL layers is significant, having a notable impact on the overscreening (λ). This is evident in Figure 7c, where the most considerable change in overscreening (maximal $d\lambda/dE$) occurs at the position of Peak II, which, according to Equation 9 leads to the capacitance peak, as $C_H = const.$ and $d\delta/dE \approx 0$.

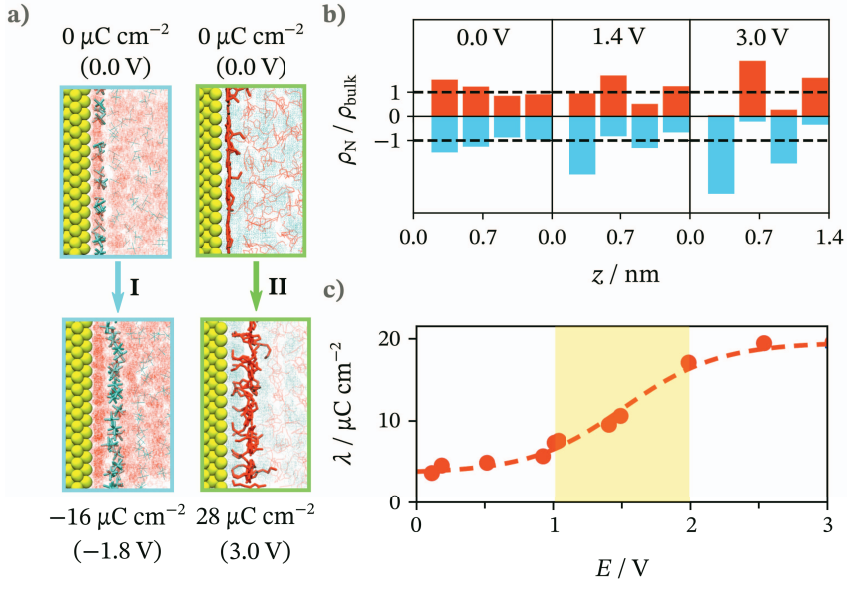

Figure 7. a) The snapshots of interfaces showing the IL′s structural changes at the Peak I and II regions; **b)** ion number density profiles (ρ_N), normalised with ion bulk density (ρ_{bulk}); **c)** overscreening (excess charge of the first IL layer) (λ) *vs.* potential (E) dependence fitted with logistic function.

The distance between the first and second layers (δ) increases at the E range around Peak III, as shown in Figure 8a and Figure 8b. The formation of a dense first IL layer causes the shift of the second IL layer. Although the first ionic liquid layer consists only of anions already at $E = 3$ V, there is still space for the cations′ alkyl chains, which reduces the repulsion between the anions. When the electrode is further charged, the alkyl chains of cations can no longer pack between the anions, leading to the reorientation of cations′ alkyl chains. The potential dependence of the shift is illustrated in Figure 8c, where it is visible that the change occurs in a highlighted potential region of Peak III. Thus, the capacitance increase is caused by a significant change of $d\delta/dE$ while the C_H remains constant and $d\lambda/dE \approx 0$.

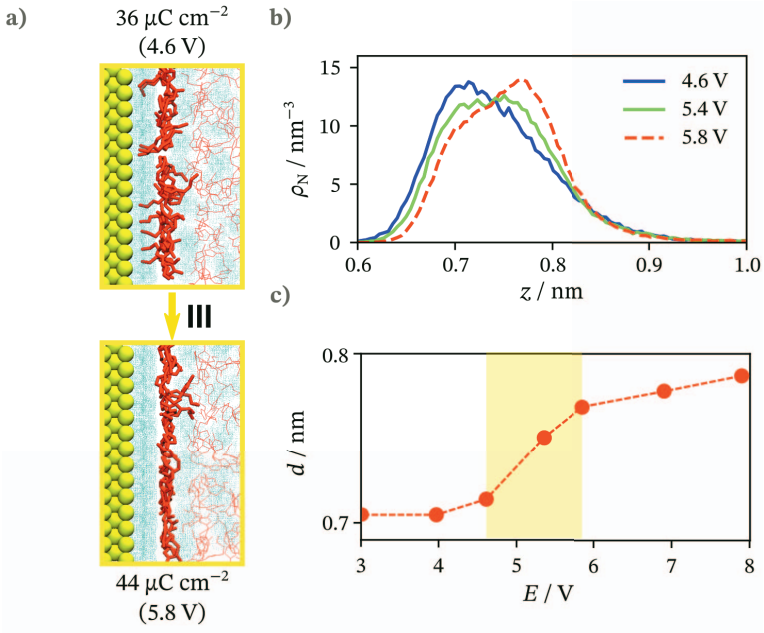

Figure 8. a) The snapshot of the interface showing the IL′s structural changes at the Peak III region; **b)** ion number density profiles (ρ_N) at noted potentials, highlighting the shifting of the second IL layer; **c)** the distance of cations′ number density maximum from the electrode′s surface (d) *vs.* potential (E).

A very dense first IL layer is formed in the E region of Peak IV. In the lower part of Figure 9b, the summed anion′s number densities up to distance z from the electrode′s surface ($\Sigma\rho_N$) are shown. From the density profile of $\sigma = 68$ μC/cm^2 (14.3 V), it can be seen that the second IL layer also contains counter-ions in contrast with density profiles around 3.0 V in Figure 7b. At $\sigma = 72$ μC/cm^2 (14.8 V), a significant structural transition occurs to an even denser first IL layer, affecting the screening of the electrode′s charge. This change can be related to the sudden increase of dλ/dE, as the denser packing allows higher charge density in the first IL layer. The notable difference in the interfacial structure, caused by a relatively small change of electrode charge, can be attributed to the existence of multiple metastable interface structures, which have high transition barriers. The high barriers lead to a slow restructuring of the ionic liquid, which cannot be captured with a relatively short duration of molecular dynamics simulations. [179,180]

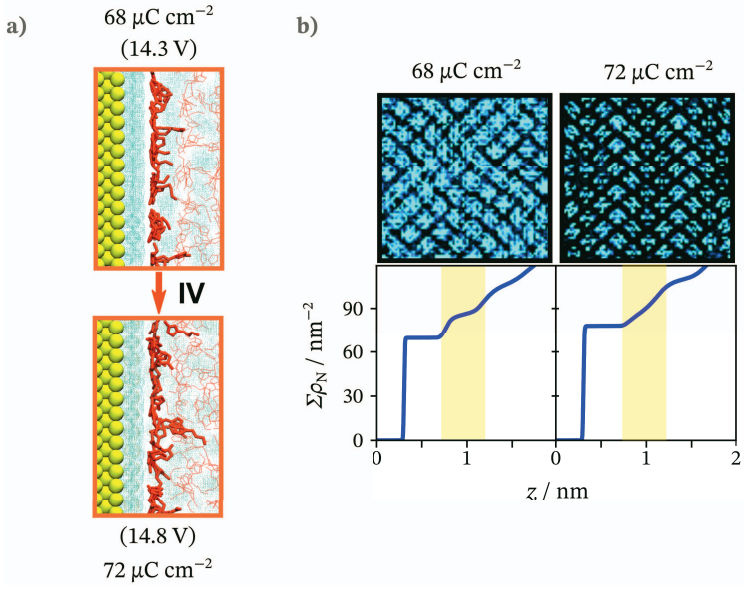

Figure 9. a) The snapshot of the interface showing the ionic liquids′ structural changes at the Peak IV region; **b)** (above) time-averaged surface distribution of ions in the contact layer, (below) the profiles of the cumulative number of anions per unit cell up to the distances z from the electrode ($\Sigma\rho_N$).

Based on the described results, it can be concluded that the peaks of *C–E* dependence correspond to the changes in the IL interfacial structure. In the *E* regions of Peaks I and II, the distribution of counter- and co-ions into alternatively charged ionic layers took place. The reorientation of cations in the second IL layer led to increased distance between the first and second IL layers around the Peak III. At very high *E* values of Peak IV, the transition between two very dense first layer structures was noted. Thus, these results agree with the conclusions by Rotenberg *et al.* [181] and Merlett *et al.* [69] that the capacitance peaks correspond to the transitions of IL interfacial structure.

6.2. Capacitance–Structure Dependence of Graphene | $EMImBF_4$

MD and DFT calculations have a crucial role in investigating the interfaces, which are challenging to study experimentally or provide insights into contrasting results. For example, in the case of electrode | IL, the capacitance has been shown to have both positive ($dC/dT > 0$) [182–184] and negative dependence ($dC/dT < 0$) [185–187] on ambient temperature. Graphene is a single layer of carbon atoms in a hexagonal structure. In the given study, as the charging of the graphene electrode induced additional potential change due to the shifting of the Fermi level [188–190], the interfacial capacitance and potential drop were divided into two: one arising due to the non-uniform distribution of electrolyte ions at the electrode–IL interface (C_{IL} and E) and the other, arising from the Fermi level shift (C_Q and ϕ_{Gr}).

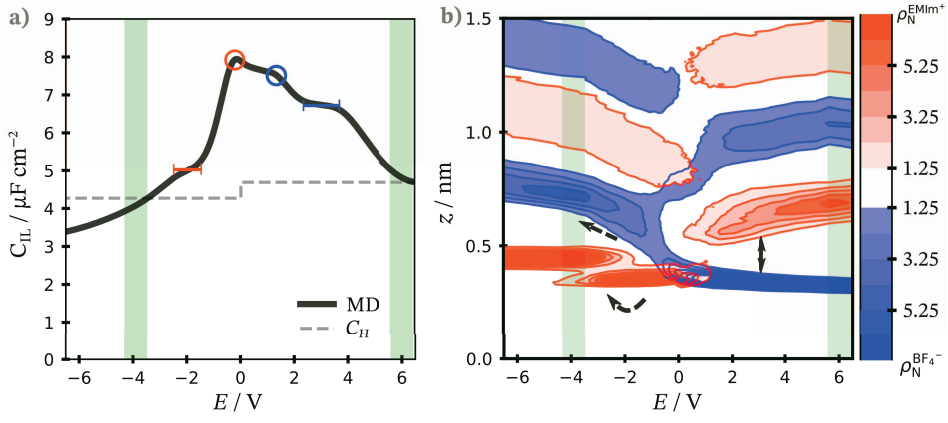

Figure 10. a) C_{IL}–E dependence at 450 K for graphene | $EMImBF_4$. The red and blue markers indicate the peaks and plateaus in the dependence; **b)** the number density (ρ_N) contour map of cations (red) and anions (blue) at 450 K. The interval of contours and colormap is equal to the bulk density of a given ion (ρ_N^{ion}).

The C_{IL}–E dependence, shown in Figure 10a, has a wide maximum around the PZC with two small peaks, which point to the changes in the IL interfacial layer structure, screening the electrode′s charge. Similarly to the Au(001) | $BMImPF_6$, the peaks occur in the E region, where the formation of an alternatively charged layer occurs, *i.e.*, there is a significant change in the overscreening of the electrode′s charge (maximal $d\lambda/dE$). In addition, there are two E regions where the C_{IL} is independent of the E. At $-2.5\ V < E < -1.5\ V$, the $EMIm^+$ ions reorient, shown in Figure 10b with a curved arrow. The reorientation of $EMIm^+$ from perpendicular to parallel position during discharge leads to the decrease of l (C_H increases as $C_H \sim 1/l$), while δ was not significantly altered ($d\delta/dE \approx 0$). Meanwhile, the reorientation decreases the overscreening as it facilitates the formation

of a sparser first IL layer upon further electrode discharging ($d\lambda/dE < 0$). Thus, the first three terms in Equation 8 balance the change of l in the given E range.

A similar compensation of various terms in Equation 8 occurs around $E = 3$ V. In this E region, the mechanism is similar to the cause of Peak III in the case of Au(001) | $BMImPF_6$, as the reorientation of the $EMIm^+$ ions in the second IL layer occurs due to the formation of denser first IL layer. This leads to the change of δ ($d\delta/dE > 0$), shown in Figure 10b with a bidirectional arrow. At the same time, the reorientation did not significantly alter the number of $EMIm^+$ ions in the second IL layer, indicating the decrease of λ ($d\lambda/dE < 0$). At $E = -4$ V and 6 V, the $C_{IL} \approx C_H$. This agrees with the bilayer model, as at these E values, the second IL layer reaches its maximum density $d\lambda/dE = 0$, while the position of the IL layers is also not shifted.

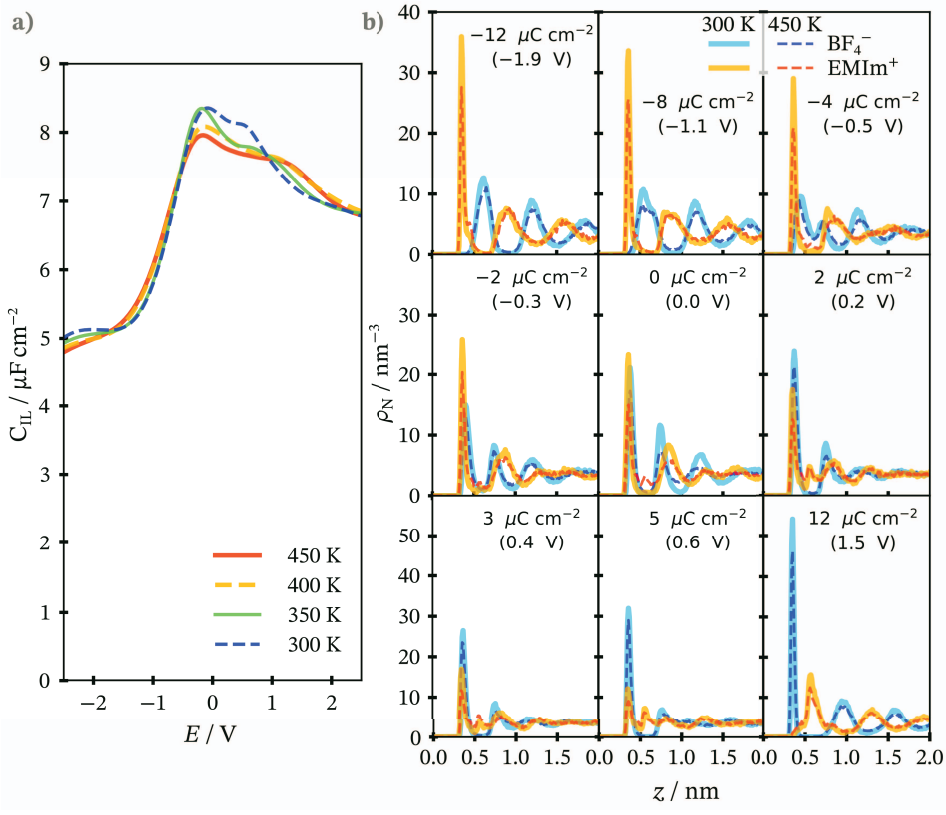

Figure 11. a) C_{IL}–E dependence for graphene | $EMImBF_4$ at noted T; **b)** number density profiles (ρ_N) of $EMIm^+$ and BF_4^- at $T = 300$ K and 450 K.

The impact of T on C_{IL} is shown in Figure 11, along with the number density profiles of ion distribution of the interface at 300 K and 450 K. From the number density profiles, it can be seen that around the PZC, the first IL layers contain both cations and anions. During the charging of the interface, the co-ions are pushed towards the second IL layer, while the counter-ions are pulled to the

graphene surface. Meanwhile, the first IL layers near the PZC contain a notable amount of co-ions despite the repulsion between the electrode and the co-ions due to ion–ion correlations and the voids on the electrode′s surface. The ambient temperature has the most significant impact on the C_{IL} near the PZC. In the E range from −0.5 V – 1 V, the increase of T led to the decrease of C_{IL}, *i.e.*, $dC/dT < 0$. There is also a notable shift of C_{IL} peaks towards larger $|E|$ values with an increase of T. In the given E range, it can be seen that the increased thermal motion led to the smearing of IL layers as the density peaks are broader and shorter at 450 K. At the same time, the increase of T did not shift the positions of IL layers. Thus, when relating the results to the bilayer model, it can be concluded that the overscreening (λ) depends on the T, while l and δ were constant.

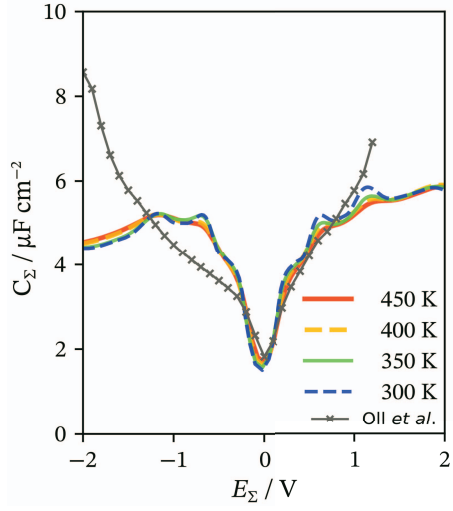

Figure 12. The overall interfacial capacitance (C_Σ) for simulated T values when accounting for the C_Q, along with experimental results of Oll *et al.* [191].

The shifting of the C_{IL} peaks further unveils a E region around 1 V – 2 V, where the $dC/dT > 0$, highlighting the importance of the choice of reference potential when discussing the dC/dT. The observed trends are in qualitative agreement with the experimental results of Drüschel *et al.* [186]. At elevated temperatures, they also observed the widening and the decrease of the C peak with the increase of T. With computational methods, the widening of capacitance peaks has been shown by Chen *et al.* with mean-field theory [187], while the shifting of the C peak due to the change of T was noted by Shen *et al.* using DFT calculations and perturbed-chain statistical associating fluid theory [192]. When considering the C_Q of graphene, the interfacial C obtained a V-like shape with a sharp minimum around the PZC, shown in Figure 12. This is due to the limiting effect of C_Q around the PZC. Furthermore, as the T has a negligible effect on C_Q, the C_Σ is only moderately affected by the T. The obtained results are in good agreement with the electrochemical impedance spectroscopy results by Oll *et al.* [191] and with molecular dynamics simulations by Paek *et al.* [193].

6.3. Adsorbed Adlayer on Bi(111) | 4,4'-BP + $EMImBF_4$

The cyclic voltammograms (CVs) of Bi(111) | $EMImBF_4$ and Bi(111) | 4,4′-BP + $EMImBF_4$ highlight the differences in interfacial processes of studied systems. The CVs of Bi(111) | $EMImBF_4$, shown in Figure 13a, have no significant *j* peaks in the *E* range from −1.1 V to −0.1 V. The increase of reduction current at more negative *E* values is related to the reduction of $EMIm^+$ cation [194] or trace O_2 and H_2O [93]. At $E > -0.1$ V, the *j* increases due to the Bi surface oxidation. In turn, when studying the electrolytes with 4,4′-BP additive in the same *E* range, a reduction peak appeared at $E = -0.97$ V during cathodic sweep, while the reversal of the sweep direction led to the oxidation peak at $E = -0.90$ V. This charge transfer process is associated with the reduction of 4,4′-BP. As visible from Figure 13b, the increase of *v* had a notable impact on the *j*. The process is limited by diffusion due to the linear j_{ox} *vs.* $\sqrt{v}$ –dependence.

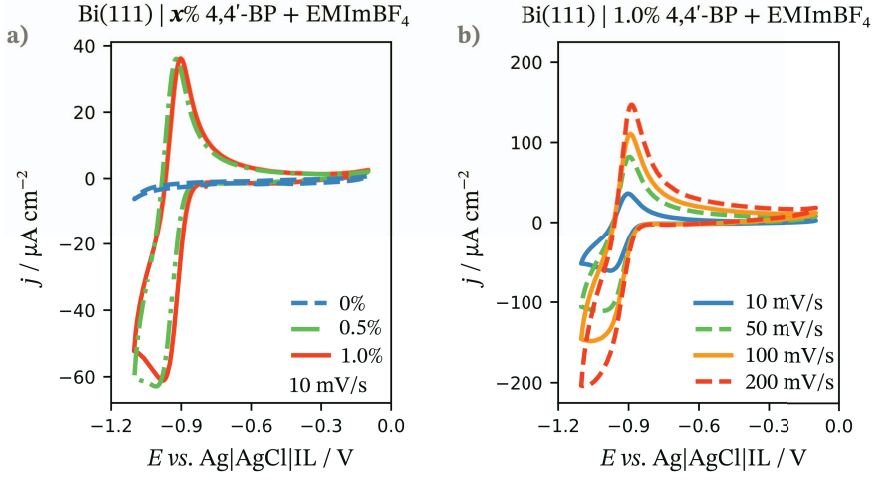

Figure 13. Cyclic voltammograms for **a)** Bi(111) in $EMImBF_4$ without and with 0.5% or 1.0% 4,4′-BP addition, measured at $v = 10$ mV/s; **b)** Bi(111) in 1.0% 4,4′-BP + $EMImBF_4$ solution measured at various scan rates, noted in the figure.

The *C*–*E* dependences of IL electrolyte with and without 4,4′-BP addition in Figure 14a point to the formation of an adsorbed 4,4′-BP adlayer. For Bi(111) | $EMImBF_4$, the *C* values in the measured *E* range are between 8 and 13 µF/cm^2. The *C*–*E* dependence has a small minimum at around −0.65 V, while there are no sharp maxima in the given *E* range. The Bode phase angle (θ) *vs.* frequency (*f*) dependencies of Bi(111) | $EMImBF_4$ in Figure 14b highlight the capacitive behaviour of the interface as at $E = -0.7$ V and $E = -0.9$ V there is a wide plateau in the *f* range 1 Hz < *f* < 300 Hz with $\theta < -85°$. The increase of θ at lower *f* is related to the reduction of trace impurities.

In turn, the *C*–*E* dependences of IL electrolytes with 4,4′-BP addition show wide adsorption plateaus (−0.8 V < *E* < −0.1 V) with *C* around 6 µF/cm^2. The

decrease of C due to the adsorption of 4,4′-BP is associated with forming a dense organic adlayer, which increases the distance between the electrode and the electrolyte ions (l), screening the electrode′s charge. In the C plateau region, the θ is below −75° in the 1 Hz < f < 300 Hz range, indicating the mixed kinetics of both adsorption- and diffusion-limited processes that can be related to the sluggish kinetics of 4,4′-BP adsorption and reorganisation. Furthermore, the 4,4′-BP reduction process is visible both in the C–E and θ–f curves. In the case of C–E dependence of 1.0% 4,4′-BP addition, there is a notable capacitance peak at E = −0.9 V. The process is of a pseudocapacitive nature as the θ increases significantly in the peak area, highlighting diffusion- and charge-transfer limited behaviour of the interface.

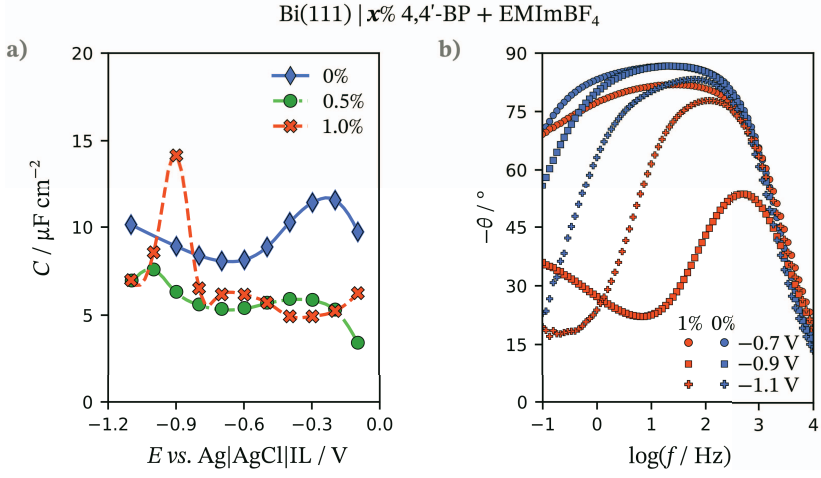

Figure 14. a) Differential capacitance (C) *vs.* potential (E) dependences for Bi(111) electrode in pure $EMImBF_4$ and with 0.5% or 1.0% 4,4′-BP addition, measured at 215 Hz; **b)** phase angle (θ) *vs.* frequency (f) dependences for Bi(111) in pure $EMImBF_4$ and with 1.0% 4,4′-BP addition at marked E values.

The scanning tunnelling microscopy measurements visualised the formation of a dense adlayer on the electrode′s surface. The striated rows of 4,4′-BP were captured at around E = −0.95 V in a very narrow potential range, where the C–E dependence in Figure 14a has a peak. The dense organised adlayer structure, shown in Figure 15a, presented itself after holding the electrode at the given potential for an extended period of time. This can be reasoned by the notable viscosity of IL and strong interactions between the IL ions, leading to the slow formation of a supramolecular structure. The 4,4′-BP molecules are interpreted to be adsorbed with the pyridine rings parallel to the Bi(111) surface. The distance between the 4,4′-BP rows is 1.6 nm, which points to a quite sparse pattern, especially considering that the distance between N atoms in the 4,4′-BP molecule is around 0.7 nm. The voids between the 4,4′-BP rows contain most likely the IL ions, which were not visualised. Similar coadsorbed striped adlayer structures have been

reported for 4,4′-BP and camphor adsorption at Bi(111) from aqueous electrolyte solutions containing sulphate ions [29,38].

The visible clusters can be related to the 4,4′-BP agglomerates adsorbed at surface defect areas [195] or to the back-deposition of Bi [194]. Curiously, the 4,4′-BP adlayers were not visualised at the plateau region of *C*–*E* dependencies. Instead, high-resolution images of Bi(111) surface (Figure 15b) were obtained in the −0.90 V < *E* < −0.65 V range. The images displayed a regular atomic structure of Bi(111) with an inter-atomic distance of 4.1 Å, in agreement with previous studies [103,196]. Thus, it can be concluded that in this *E* region, the 4,4′-BP is not strongly bound to the Bi(111) surface and its interactions with Bi(111) are only slightly favoured over the surface indifferent $EMImBF_4$ ions.

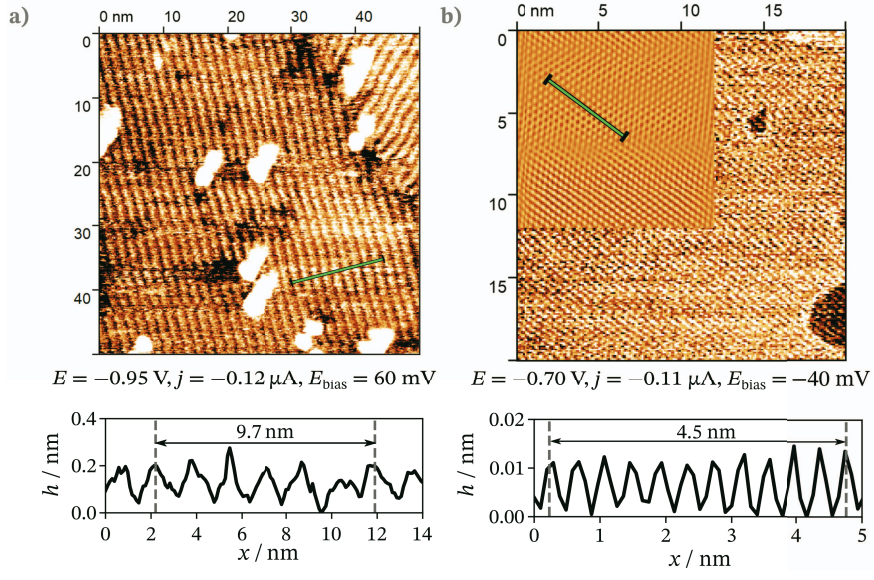

Figure 15. EC–STM images for Bi(111) in 1.0% 4,4′-BP + $EMImBF_4$ solution along with height profiles of the lines shown in STM images at **a)** *E* = −0.95 V and **b)** *E* = −0.70 V.

The formation of ordered 4,4′-BP adlayer was studied further with DFT to identify the most probable adsorption sites and adlayer configurations. First, the adlayer consisting of only 4,4′-BP molecules was studied. The adlayer configuration with the lowest predicted energy per surface atom (−0.33 eV) is shown in Figure 16a. The unit cell of this configuration consists of two 4,4′-BP molecules adsorbed at the top and bridge sites. The E_{ads} of a 4,4′-BP molecule in the configuration is −1.32 eV, while an isolated 4,4′-BP molecule at the top or bridge position was −1.00 eV and −0.98 eV, respectively. Thus, the intramolecular interactions between the 4,4′-BP molecules stabilise the adsorption layer structure.

Although the molecules are situated in a striated pattern similar to STM measurements, the predicted 4,4′-BP adlayer structure (with an estimated surface concentration of 2.3×10^{-10} mol/cm^2) is significantly denser. Thus, the coadsorbed structure of $EMIm^+$ ions and 4,4′-BP molecules was studied. One 4,4′-BP

molecule in the dense unit cell structure was replaced with an $EMIm^+$ cation to match the STM-visualised structure. The adsorption of $EMIm^+$ was considered more likely as the striated pattern was imaged at a lower potential than the PZC of Bi(111) | $EMImBF_4$ (−0.7 V *vs.* Ag | AgCl) [93]. The $EMIm^+$ was modelled to be adsorbed in the imidazolium plane parallel to the Bi(111) surface, which is a more probable orientation at low negative surface charge densities [178,197]. The given coadsorbed configuration is favoured over the 4,4′-BP monolayer, as its adsorption energy per surface atom is −0.42 eV. The E_{ads} was −1.68 eV in this configuration (Figure 16b). Thus, the coadsorption of $EMIm^+$ has a stabilising effect on the adlayer structure. Additionally, the adsorption energies of $EMIm^+$ at various coverages were evaluated by varying the unit cell size. The lowest estimated adsorption energy per surface atom was −0.44 eV at coverage 1/4, similar to the coadsorbed structure.

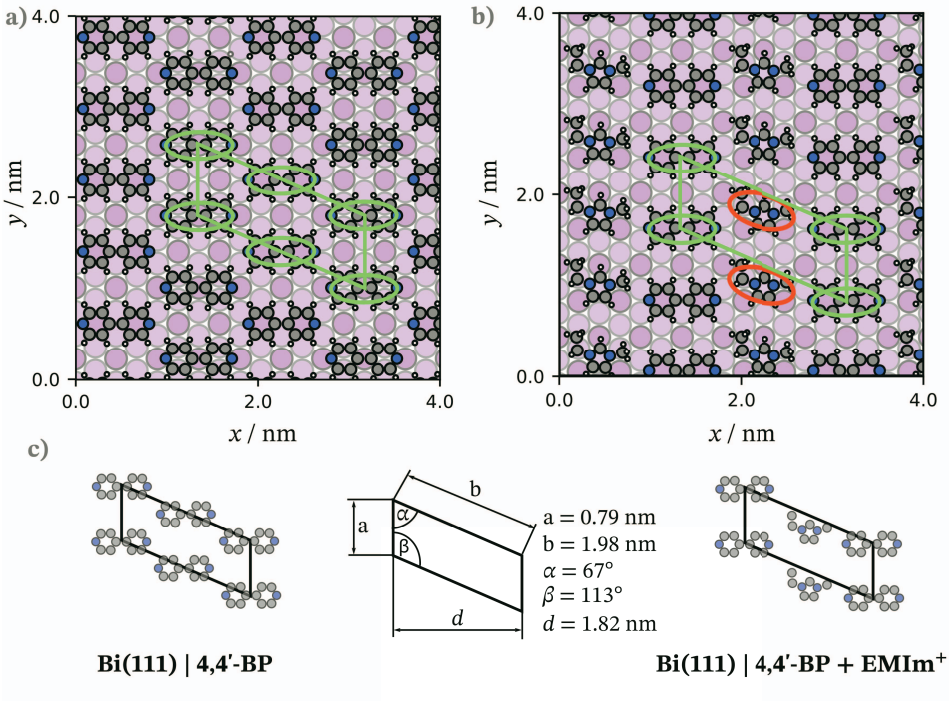

Figure 16. Monolayer configurations with the lowest adsorption energy per surface area consisting of **a)** 4,4′-BP molecules and **b)** $EMIm^+$ and 4,4′-BP molecules coadsorbed on Bi(111) surface; **c)** unit cells of adsorbed structures.

6.4. Adsorbed Multilayers on Sb(111) | 4,4'-BP + $EMImBF_4$

Sb and Bi have the same crystal structure and only differ slightly in lattice parameters and electronic properties. Thus, they are an exemplary pair of model electrodes to investigate the impact of small variations of electrode material electronic and structural properties on the interfacial characteristics. The CVs of Sb(111) in $EMImBF_4$ and 1% 4,4′-BP + $EMImBF_4$ mixture, measured in the range $-1.1\ V < E < -0.1\ V$, are shown in Figure 17a and b. For Sb(111) | $EMImBF_4$, when scanning in the negative direction, there is an increase of reduction j already at $E < -0.95$ V, associated with the reduction of trace impurities. In the CVs of Sb(111) | 1.0% 4,4′-BP + $EMImBF_4$, a similar increase of current density caused by the faradic charge transfer process as in the case of Bi(111) | 4,4′-BP + $EMImBF_4$ is visible at $E = -0.9$ V. The charge transfer process is partially reversible as both oxidation and reduction peaks are visible when the E scan direction is switched. Furthermore, the process at $E = -0.9$ V appears diffusion-limited due to the linear dependence of oxidation peak current (j_{ox}) on the square root of the potential scan rate ($\sqrt{v}$), as shown in Figure 17d.

The C–E dependence of measured Sb(111) | IL interfaces, illustrated in Figure 17c, shows that for $EMImBF_4$, there are no significant C peaks in the studied E range in contrast with 1.0% 4,4′-BP + $EMImBF_4$ mixture, where the charge transfer process is also visible. The C values of Sb(111) | $EMImBF_4$ are around 13 μF/cm^2. For Sb(111) | 4,4′-BP + $EMImBF_4$, the C values (around 9 μF/cm^2) are lower than for $EMImBF_4$, at $-0.5\ V < E < -0.1\ V$, pointing to the adsorption of 4,4′-BP. The C increases to 13 μF/cm^2 at $-0.7\ V < E < -0.6\ V$, suggesting reorganisation or desorption of 4,4′-BP, followed by the charge transfer process at $E = -0.9$ V.

The impedance modulus ($|Z|$) and Bode (θ) plots in Figure 18 highlight the differences between interfacial processes kinetics of systems with and without 4,4′-BP addition. In the $-0.8\ V < E < -0.2\ V$ range, the Sb(111) | $EMImBF_4$ has $\theta < -80°$ and the fitted slope of $\log(|Z|) < -0.9$ in a $1\ Hz < f < 500\ Hz$ region. Thus, slightly differing from the ideal capacitive behaviour [198]. The increase of θ (visible at $f < 1$ Hz) can be associated with slow IL reorganisation processes with partial charge transfer [199,200]. The Bode plots of IL mixture with 4,4′-BP show similar trends in the $-0.6\ V < E < -0.2\ V$ range without the increase of θ at very small f. A notable difference exists between the Bode plots of studied systems at $-0.9\ V < E < -0.6\ V$. The θ increases significantly with the decrease of E, implying a mixed kinetic process, where the rate is determined by a combination of various charge- and diffusion-limited processes. The changes in the shape of the θ–f dependence can be associated with the reorganisation of the 4,4′-BP layer (around −0.7 V) and the charge transfer process (around −0.9 V). The θ–f dependences of both systems are very similar at $E = -1.1$ V, possibly due to the occurrence of interfacial processes with trace impurities.

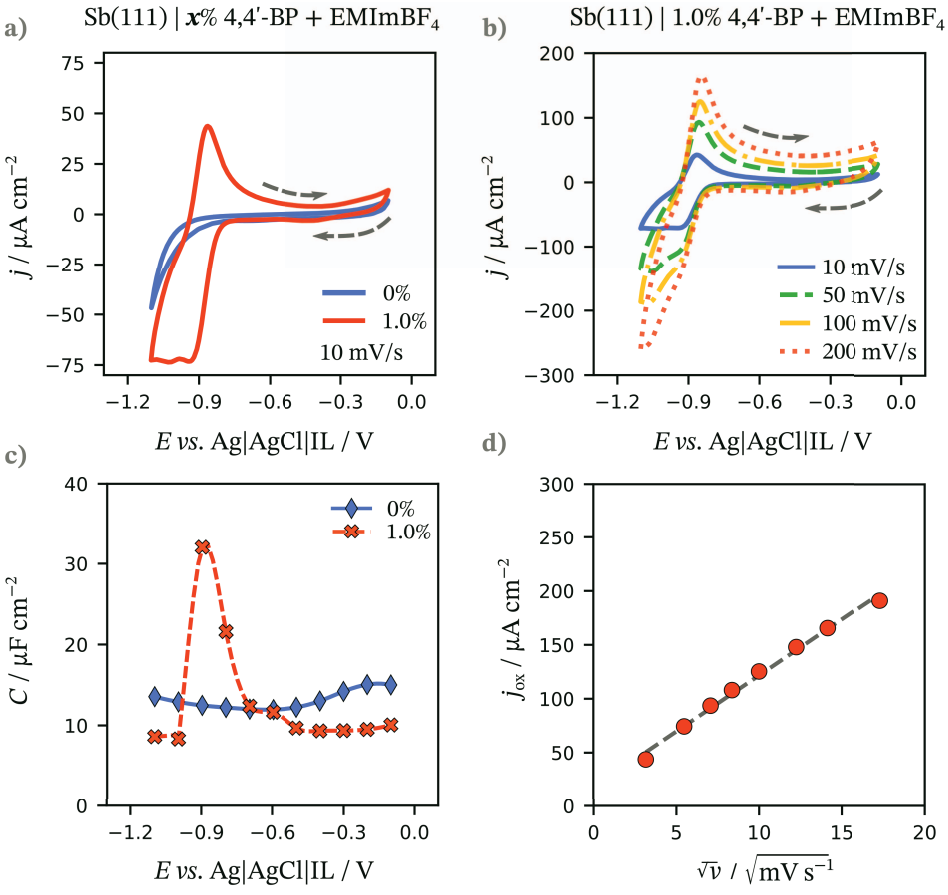

Figure 17. a) CVs at 10 mV/s scan rate for Sb(111) in $EMImBF_4$ and in 1.0% 4,4′-BP + $EMImBF_4$ solution; **b)** CVs at different scan rates rate for Sb(111) in 1.0% 4,4′-BP + $EMImBF_4$ solution; **c)** capacitance (C) *vs.* potential (E) dependences, measured at 215 Hz rate for Sb(111) in $EMImBF_4$ and in 1.0% 4,4′-BP + $EMImBF_4$ solution; **d)** oxidation current (j_{ox}) *vs.* scan rate (v) dependence for Sb(111) in 1.0% 4,4′-BP + $EMImBF_4$ solution.

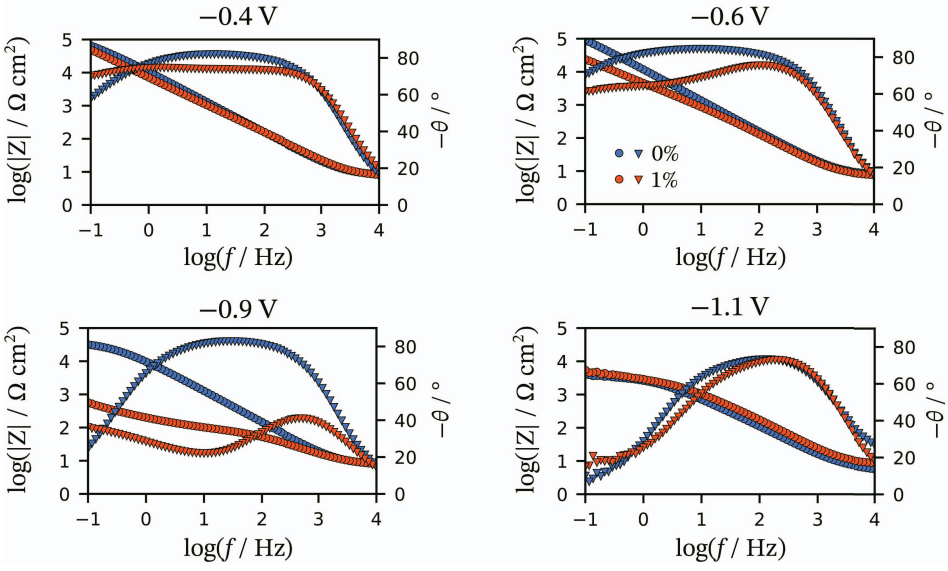

Figure 18. The combined plots of impedance modulus (|*Z*|) *vs.* frequency (*f*) (circles) and phase angle (θ) *vs.* frequency (*f*) (triangles) for Sb(111) | $EMImBF_4$ and Sb(111) | 1.0% 4,4′-BP + $EMImBF_4$, noted with blue and red colour, respectively.

The Sb(111) | 4,4′-BP + $EMImBF_4$ interface was further studied with EC–STM in the same *E* range as EIS and CV measurements. In contrast with the Bi(111) surface, the ordered 4,4′-BP adsorbed structures were visualised in a wide *E* range between −0.9 V < *E* < −0.65 V. The visualised structures are shown in Figure 19, where a striated pattern of 4,4′-BP rows (Layer II) can be seen at *E* = −0.85 V and *E* = −0.75 V. When the *E* was further decreased to *E* = −0.9 V, a denser surface structure (Layer I) appeared over time beneath the Layer II due to partial desorption or reorganisation of the adsorbed structure (see Figure 20). The denser structure (Layer I) was associated with 4,4′-BP as the separation between the ordered rows is notably larger (7.2 Å) than the distance between the nearest Sb surface atoms (4.3 Å), while very similar to the length of 4,4′-BP molecule. Furthermore, previously, for Sb(111) | $EMImBF_4$, an atomic structure of Sb(111) was imaged [91]. In both Layers I and II, the molecules are interpreted to be adsorbed with the bipyridine ring plane parallel to the electrode′s surface. The ordered structures disappeared at *E* > −0.75 V, possibly due to the changes in the interfacial structure caused by the adsorption of 4,4′-BP along with more mobile $EMImBF_4$ ions. In addition to the ordered 4,4′-BP structures, the clusters were observed at the Sb(111) surface. The clusters can be attributed to the polymerisation of reduced 4,4′-BP and its deposition to the surface as their number and size depend on the applied *E*, similarly to [41].

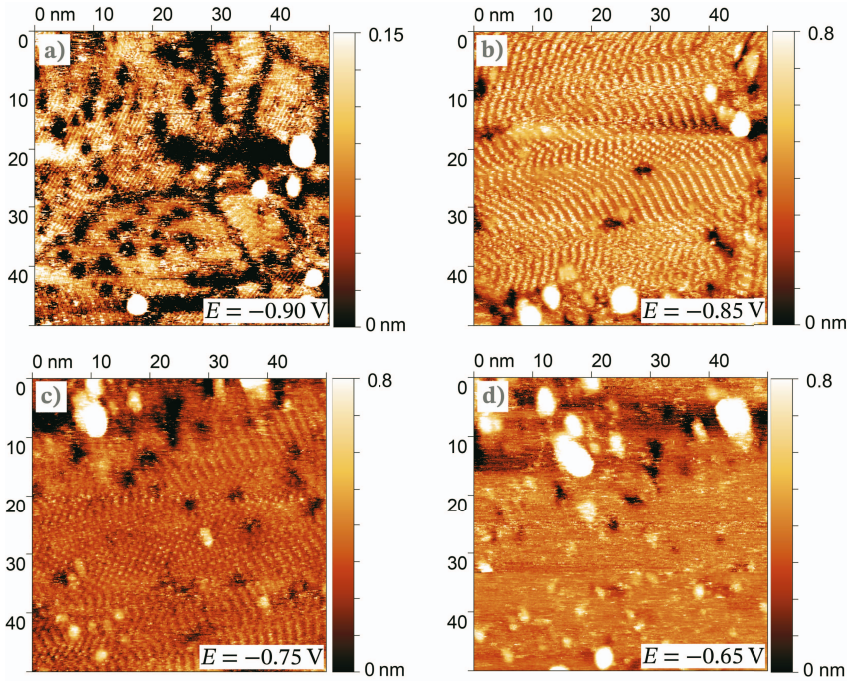

Figure 19. EC–STM images of Sb(111) | 1.0% 4,4′-BP + $EMImBF_4$ interface at potentials: **a)** $E = -0.90$ V, **b)** $E = -0.85$ V, **c)** $E = -0.75$ V, and **d)** $E = -0.65$ V.

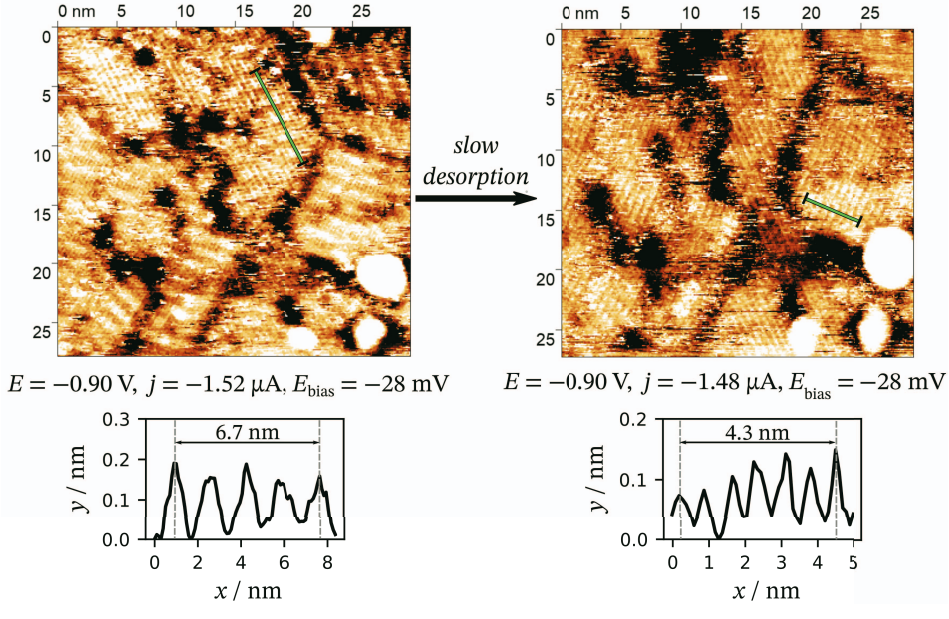

Figure 20. EC–STM images of Sb(111) | 1.0% 4,4′-BP + $EMImBF_4$ at $E = -0.90$ V with height profiles, showing desorption of 4,4′-BP from Sb(111).

EC–STM results were combined with DFT calculations to further characterise and analyse the adsorbed structures. The identified adlayers and their unit cells are shown in Figure 21. Based on EC–STM images of Layer I, the adsorbed 4,4′-BP molecules form tightly ordered rows with pyridine rings visible. The unit cell measurements of Layer I were determined with DFT. The modelled surface structure with the lowest predicted energy per surface atom is shown in Figure 21b. Similarly to EC–STM of Layer I, the structure consists of dense 4,4′-BP rows with molecules positioned at hollow 1 adsorption site and a calculated surface concentration of 2.6×10^{-10} mol/cm^2. The N-atoms of 4,4′-BP molecules are rotated towards the hydrogen atoms of neighbouring 4,4′-BP molecules in the same unit cell. The E_{ads} of a 4,4′-BP molecule in the modelled structure was −1.37 eV, significantly lower than that of an isolated 4,4′-BP molecule at hollow 1 site (−0.66 eV). This underlines the importance of intermolecular interactions in the adsorbed adlayer towards the stabilisation of the adlayer.

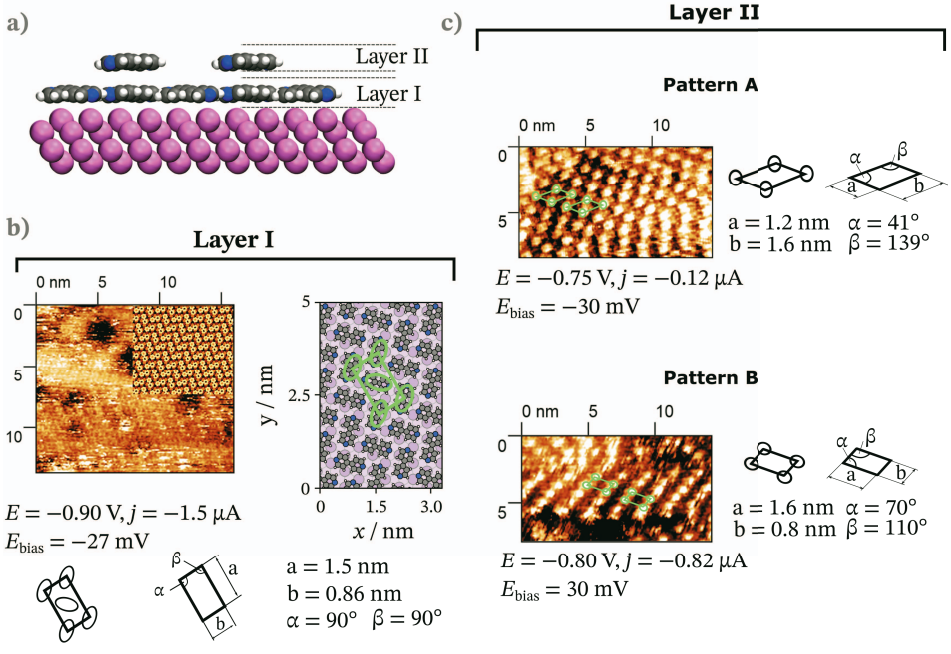

Figure 21. a) The model of 4,4′-BP multilayer structure on Sb(111) surface. EC–STM images and unit cells belonging to adlayer structures of **b)** Layer I and **c)** Layer II. The EC–STM image of Layer I contains an inset of the calculated STM image and the surface structure obtained from DFT calculations.

Two different adsorbed 4,4′-BP molecule structures were identified in Layer II, shown in Figure 21c. The unit cell of Pattern A is a parallelogram with 4,4′-BP molecules at the corners. The closest distance between the molecules in the same row was 1.2 nm. Pattern B has a more compact structure, with the distance between the 4,4′-BP molecules in the same layer being 0.8 nm. The surface concentrations of 4,4′-BP in Pattern A and B were estimated to be 1.28×10^{-10} mol/cm^2 and 1.38×10^{-10} mol/cm^2, respectively. The existence of multiple adsorbed structures at similar E values can be associated with the defects in Layer I beneath Layer II.

The study revealed the existence of an ordered adsorbed multilayer structure at the Sb(111) surface. Previously, significant capacitance depressions were related to the formation of such structures for aqueous electrolytes, while not directly visualised [8]. In turn, the formation of a layered interfacial structure of IL ions has been demonstrated with both experimental [126,201,202] and computational techniques [69,80,82,203]. Moreover, depending on the length of the cation′s alkyl chains, the interfacial structure has been shown to undergo structural transformations from alternatively charged layers to intertwined bilayer structure [72,204,205]. The formation of a multilayer structure of organic molecules can be reasoned with the strong interactions between the 4,4′-BP molecules in the adlayer and the Sb(111) surface. Furthermore, due to strong electrostatic interactions between the IL ions and the notable viscosity of IL, the partial desorption of 4,4′-BP was slow compared to desorption processes in aqueous electrolytes. Thus, the imaging of multilayer structure was possible.

6.5. Adsorbed Clusters on Cd(0001) | 4,4'-BP + $EMImBF_4$

The Cd(0001) has stronger metallic and hydrophilic properties than Bi(111) and Sb(111) [114]. Moreover, Cd metal atoms are in a hexagonal close-packed structure instead of rhombohedral. These differences in substrate properties carry over to the CVs of Cd(0001) | $EMImBF_4$ and Cd(0001) | 4,4′-BP + $EMImBF_4$ (shown in Figure 22) when compared to similar systems at Bi(111) and Sb(111) electrodes.

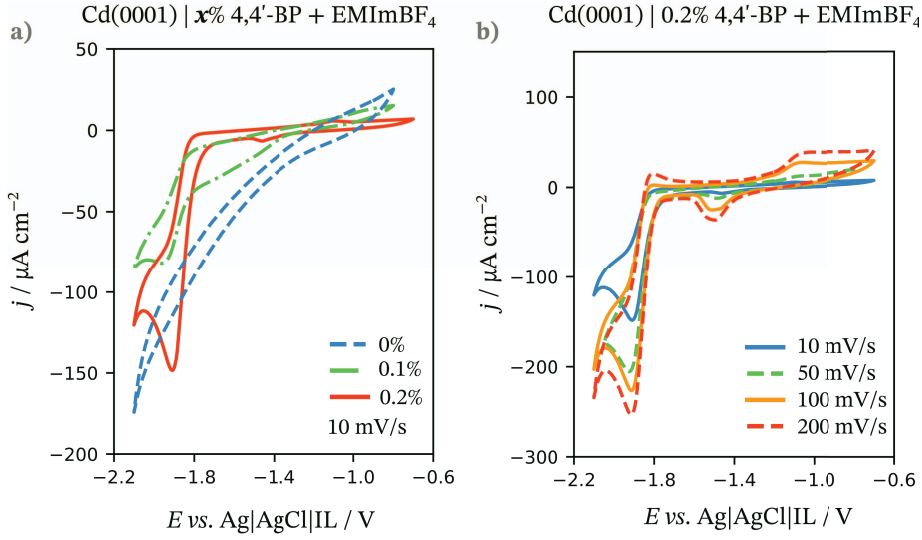

Figure 22. a) CVs at 10 mV/s scan rate for Cd(0001) in $EMImBF_4$ and in 4,4′-BP + $EMImBF_4$ solution with 0.1% or 0.2% 4,4′-BP addition, **b)** CVs at different scan rates for Cd(0001) in 0.2% 4,4′-BP + $EMImBF_4$ solution.

For Cd(0001) | $EMImBF_4$, although there are no j peaks in the studied E range, the j increases/decreases significantly at the limiting cathodic and anodic E values, possibly due to the decomposition of IL or trace water and Cd dissolution, respectively. The studied interfaces with 4,4′-BP addition had smaller $|j|$ values at $-1.7\ \text{V} < E < -0.7\ \text{V}$ than observed for $EMImBF_4$. This can be reasoned with the formation of a dense blocking 4,4′-BP layer, hindering the decomposition of IL/water and Cd dissolution. During the E scan in the negative direction, a reduction peak associated with 4,4′-BP reduction was visible at $E = -1.9$ V. Also, at higher v, a smaller reduction peak at $E = -1.5$ V appeared. The switching of a E scan direction led to the appearance of a significantly smaller oxidation peak at $E = -1.8$ V, visible only at higher v.

The measured C values of Cd(0001) | $EMImBF_4$ are consistently higher than for studied systems with 4,4′-BP addition in the studied E range, indicating the formation of 4,4′-BP adlayer. In the C–E dependences, shown in Figure 23a, the C values of Cd(0001) | $EMImBF_4$ are around 8–9 μF/cm^2 at $-1.9\ \text{V} < E < -1.0\ \text{V}$, in agreement with results by Pikma *et al.* [92]. The increase of C at more negative E values is of a pseudocapacitive nature related to the

reduction processes visible in Figure 22. The *C*–*E* dependences of interfaces with 4,4′-BP addition for both studied concentrations of 4,4′-BP have very low *C* values around 3 μF/cm^2 at $E > -1.7$ V. The concentration increase did not significantly impact the *C* plateau value due to the formation of a dense 4,4′-BP adlayer covering the Cd(0001) surface, already at 0.1% 4,4′-BP concentration. In the case of 0.2% 4,4′-BP addition, a *C* peak is visible at $E = -1.8$ V, related to the charge transfer process involving 4,4′-BP molecules. The same *C* peak is also visible for 0.1% 4,4′-BP addition at smaller *ac* frequencies.

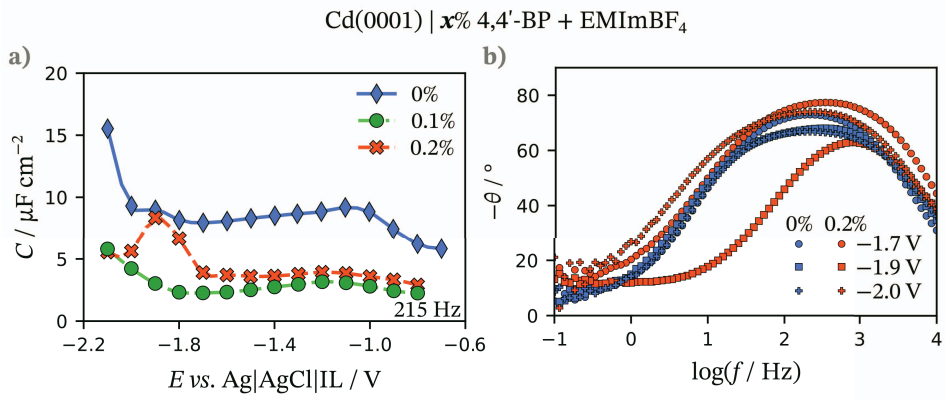

Figure 23. a) Capacitance (*C*) *vs.* potential (*E*) and **b)** Bode phase (θ) *vs.* frequency (*f*) dependencies of Cd(0001) | 4,4′-BP + $EMImBF_4$ with noted 4,4′-BP concentrations.

The θ–*f* dependencies in Figure 23b show notable deviation from the ideal capacitive behaviour for both Cd(0001) | $EMImBF_4$ and Cd(0001) | 4,4′-BP +$EMImBF_4$. For Cd(0001) | $EMImBF_4$ in the 50 Hz < *f* < 1000 Hz range, the interface is characterised by mixed kinetic behaviour as θ has minimum values of −71° and −65° at $E = -1.7$ V and $E = -2.0$ V, respectively. A nearly charge-transfer-limited behaviour is visible at very low *f* (*f* < 1 Hz) as θ is higher than −20°. For Cd(0001) | 0.2% 4,4′-BP + $EMImBF_4$, the θ values in the 50 Hz < *f* < 1000 Hz range are noticeably lower than for neat IL electrolyte. The increase of θ in the low *ac f* region (*f* < 10 Hz) occurred only at $E < -1.1$ V, while at more positive *E* values, the θ remained well below −40°. This is in contrast with the results of similar systems at Bi(111) and Sb(111) surfaces, where similar θ increase occurred at *E* values around the *j* peak related to the 4,4′-BP oxidation/reduction process.

The EC–STM images of Cd(0001) | 0.2% 4,4′-BP + $EMImBF_4$ at the beginning of an experiment (Figure 24) showed a smooth Cd surface with the steps between the terraces corresponding to the multiples of 2.8 Å, *i.e.*, the distance between the neighbouring Cd layers in the hexagonal close-packed structure [113]. During the prolonged EC–STM experiment, the smooth Cd surface was replaced by clusters, which can be related to 4,4′-BP agglomerates. The process is shown in Figure 25 over the course of 1 hour. First, the clusters appeared on the electrode surface′s step edges and defect areas, where there are under-co-

ordinated Cd atoms [206]. Followingly, the clusters also appeared on the terraces and led to the disappearance of well-defined step edges and smooth planes. These results contrast the previous 4,4′-BP adsorption study of Cd(0001) conducted in an aqueous electrolyte, where a well-ordered adlayer of 4,4′-BP with a striated pattern was visualised in a narrow potential range [45]. The existence of a highly ordered structure in the case of Cd(0001) | 0.2% 4,4′-BP + $EMImBF_4$ cannot be excluded entirely, as the 4,4′-BP may have been adsorbed in a configuration, which was not visualised with the EC–STM.

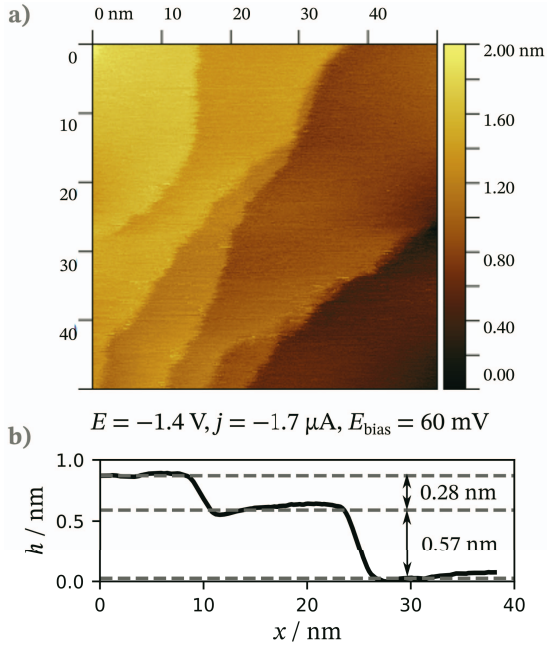

Figure 24. a) EC–STM image of Cd(0001) | 0.2% 4,4′-BP + $EMImBF_4$, illustrating the smooth Cd(0001) surface at the beginning of the experiment; **b)** the height profile of the given STM image with the heights of the visualised steps.

The interplay between interactions can explain the formation of various visualised 4,4′-BP structures, such as ordered multilayer, monolayer, and clusters. The hydrophilicity of studied single crystal surfaces has been shown to increase in the order of Sb(111) < Bi(111) < Cd(0001) [114]. At the same time, the estimated 4,4′-BP adlayer structures at the Bi(111) and Sb(111) surfaces had similar adsorption energies (−1.32 eV and −1.37 eV, respectively). Therefore, the stronger interactions of polar ions with the electrode′s surface can hinder the diffusion of adsorbed 4,4′-BP molecules on the electrode′s surface. Simultaneously, the adsorption of 4,4′-BP is energetically favoured due to strong short- and long-range interactions between IL ions ″squeezing out″ the organic molecules from the IL to the electrode′s surface [207].

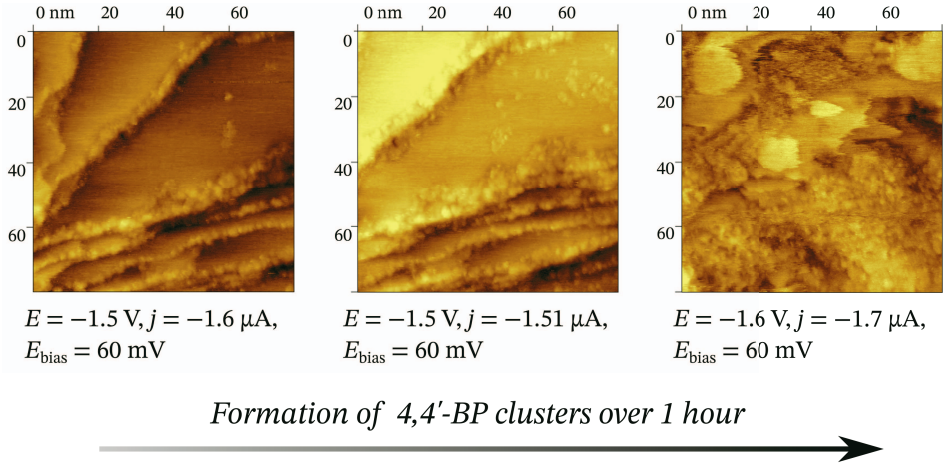

Figure 25. EC–STM images of Cd(0001) | 0.2% 4,4′-BP + $EMImBF_4$ displaying the formation of the clusters on the smooth Cd(0001) surface over time.

7. SUMMARY

Given the transition to sustainable applications, a comprehensive understanding of processes at the molecular level in electrode–electrolyte interfaces is imperative for developing more efficient technologies. This thesis focused on the characterisation of adsorption processes and the electrode–ionic liquid interface structure. The properties and structures of the model single crystal electrode and ionic liquid interfaces were investigated with experimental cyclic voltammetry, electrochemical impedance spectroscopy, and electrochemical scanning tunnelling microscopy techniques, as well as density functional theory calculations and molecular dynamics simulations.

The simulations of Au(001) | $BMImPF_6$ and graphene | $EMImBF_4$ provided atomic-level insights into the structural changes of the interface, elucidating capacitance–structure and capacitance–temperature dependences. The simulations showed that the plateaus and peaks in the capacitance–potential dependence are related to the restructuring of the ionic liquid at the electrode surface within electrical double layer region. The derived bilayer model provided a qualitative description of the capacitance–structure dependence, relating the characteristic points in the *C–E* dependence to the change of electrode charge screening (λ) and the reorientation of IL ions (l and δ). Moreover, the simulations showed that the ambient temperature (T) decreased the interfacial capacitance ($dC/dT < 0$) around the potential of zero charge. As the profiles of ion distribution did not show a notable shifting of IL layers in the studied T range, it was concluded that the λ is dependent on the T, while l and δ are constant. Including graphene′s quantum capacitance (C_Q) highlighted the importance of proper description of electrode properties as it significantly dampened the effect of T on overall interfacial C due to the weak T dependence of C_Q.

The studies of 4,4′-bipyridine (4,4′-BP) adsorption from $EMImBF_4$ on Bi(111), Sb(111), and Cd(0001) showed the impact of electrode characteristics on the adsorption and self-assembly processes from IL. Although the formation of dense 4,4′-BP adlayers was identified with electrochemical impedance spectroscopy, the scanning tunnelling microscopy results displayed the differences in self-assembled adlayer structures. The observed 4,4′-BP adsorbed structures were: ordered multilayer structure at Sb(111), coadsorbed monolayer structure at Bi(111), and 4,4′-BP agglomerates at Cd(0001).

The comparison with previous 4,4′-BP adsorption studies from aqueous solutions highlighted the impact of the electrolyte on the formed adsorbed structures and the interfacial processes. The slow formation of ordered self-assembled structures in ionic liquid led to various adsorbed patterns and even ordered organic multilayer structures. Thus, the trends and adsorption behaviour established in aqueous electrolytes may not be straightforwardly transferable to adsorption from ionic liquid electrolytes. As the alteration of electrode or electrolyte leads to very different adlayers – from highly-organised structures to disordered clusters – the suitability of a chosen interface for specific nanoelectronic applications must be verified. Although the adoption of ionic liquid electrolytes raises challenges, the systematic characterisation of their peculiar interfacial behaviour paves the way for their wider utilisation in practical applications.

8. REFERENCES

[1] H. Chen, J. Fraser Stoddart, From molecular to supramolecular electronics, Nat. Rev. Mater. 6 (2021) 804–828.

[2] D.R. MacFarlane, N. Tachikawa, M. Forsyth, J.M. Pringle, P.C. Howlett, G.D. Elliott, J.H. Davis, M. Watanabe, P. Simon, C.A. Angell, Energy applications of ionic liquids, Energy Environ. Sci. 7 (2014) 232–250.

[3] M.V. Fedorov, A.A. Kornyshev, Ionic Liquids at Electrified Interfaces, Chem. Rev. 114 (2014) 2978–3036.

[4] G. Jeanmairet, B. Rotenberg, M. Salanne, Microscopic Simulations of Electrochemical Double-Layer Capacitors, Chem. Rev. 122 (2022) 10860–10898.

[5] R. Hayes, G.G. Warr, R. Atkin, Structure and Nanostructure in Ionic Liquids, Chem. Rev. 115 (2015) 6357–6426.

[6] S. Trasatti, S. Trasatti, R. Parsons, Interphases in systems of conducting phases, Pure Appl. Chem. 58 (1986) 437–454.

[7] A. Kühnle, Self-assembly of organic molecules at metal surfaces, Curr. Opin. Colloid Interface Sci. 14 (2009) 157–168.

[8] R. Sridharan, R. de Levie, Condensed thymine films at the mercury/water interface: Part V. Phase transitions, J. Electroanal. Chem. Interfacial Electrochem. 230 (1987) 241–256.

[9] R. De Levie, The dynamic double layer: Two-dimensional condensation at the mercury-water interface, Chem. Rev. 88 (1988) 599–609.

[10] R. Srinivasan, R. De Levie, Stochastic behavior in the formation of condensed coumarin films at the mercury-solution interface, J. Phys. Chem. 91 (1987) 2904–2908.

[11] S. Sathyanarayana, K.G. Baikerikar, Interpretation of differential capacitance curves obtained during a two-dimensional association of organic molecules, J. Electroanal. Chem. Interfacial Electrochem. 21 (1969) 449–455.

[12] R.D. Armstrong, The kinetics of adsorption of pyridine at a mercury electrode, J. Electroanal. Chem. Interfacial Electrochem. 20 (1969) 168–170.

[13] S. Sotiropoulos, P. Nikitas, N. Papadopoulos, Adsorption of sodium dodecylsulphate on mercury as an example of micellization within a multilayer interphase, J. Electroanal. Chem. 356 (1993) 201–223.

[14] M. Van krieken, C. Buess-Herman, On the dissolution kinetics of two-dimensional uridine layers adsorbed on gold single-crystal electrodes, Electrochimica Acta 43 (1998) 2831–2841.

[15] G. Nurk, A. Jänes, K. Lust, E. Lust, Adsorption kinetics of 2-methyl-2-butanol on bismuth single crystal planes, J. Electroanal. Chem. 515 (2001) 17–32.

[16] E. Lust, A. Jänes, K. Lust, Adsorption of propanol on bismuth single-crystal-plane electrodes, J. Electroanal. Chem. 436 (1997) 141–153.

[17] A. Popov, R. Naneva, N. Dimitrov, T. Vitanov, V. Bostanov, R. de Levie, Two-dimensional condensation of thymine on a basal face of a cadmium single crystal, Electrochimica Acta 37 (1992) 2369–2371.

[18] L. Stolberg, J. Lipkowski, D.E. Irish, Adsorption of pyridine at the Au (100)-solution interface, J. Electroanal. Chem. Interfacial Electrochem. 238 (1987) 333–353.

[19] L. Stolberg, J. Lipkowski, D.E. Irish, Adsorption of pyridine at the Au(110)-solution interface, J. Electroanal. Chem. Interfacial Electrochem. 296 (1990) 171–189.

[20] A. Hamelin, S. Morin, J. Richer, J. Lipkowski, Adsorption of pyridine on the (110) face of silver, J. Electroanal. Chem. Interfacial Electrochem. 272 (1989) 241–252.
[21] A. Hamelin, S. Morin, J. Richer, J. Lipkowski, Adsorption of pyridine on the (210) face of silver, J. Electroanal. Chem. Interfacial Electrochem. 304 (1991) 195–209.
[22] E. Lust, A. Jänes, P. Miidla, K. Lust, Adsorption of pyridine on the (111), (001) and (001) faces of bismuth, J. Electroanal. Chem. 425 (1997) 25–37.
[23] Th. Wandlowski, M.H. Hölzle, Structural and Thermodynamic Aspects of Phase Transitions in Uracil Adlayers. A Chronocoulometric Study, Langmuir 12 (1996) 6604–6615.
[24] M.H. Hölzle, Th. Wandlowski, D.M. Kolb, Structural transitions in uracil adlayers on gold single crystal electrodes, Surf. Sci. 335 (1995) 281–290.
[25] T. Sagara, S. Tanaka, K. Miuchi, N. Nakashima, Characteristics of faradaic phase transition of an adsorption layer of heptyl viologen at a basal plane HOPG electrode, J. Electroanal. Chem. 524–525 (2002) 68–76.
[26] T. Higashi, T. Kawamoto, S. Yoshimoto, T. Sagara, Two Sharp Phase Change Processes of Diphenyl Viologen at a Au(111) Electrode Surface: Non-Faradaic Transition with Interplay of Ionic Adsorption of Chloride and Bromide and Faradaic One, J. Phys. Chem. C 119 (2015) 1320–1329.
[27] K. Cui, I. Dorner, S.F.L. Mertens, Interfacial supramolecular electrochemistry, Curr. Opin. Electrochem. 8 (2018) 156–163.
[28] Th. Dretschkow, A.S. Dakkouri, Th. Wandlowski, In-Situ Scanning Tunneling Microscopy Study of Uracil on Au(111) and Au(100), Langmuir 13 (1997) 2843–2856.
[29] S. Kallip, H. Kasuk, V. Grozovski, P. Möller, E. Lust, Adsorption of camphor and 2,2′-bipyridine on Bi(1 1 1) electrode surface, Electrochimica Acta 53 (2008) 4035–4045.
[30] T.-H. Vu, T. Wandlowski, Self-Assembled Structures of Benzoic Acid on Au(111) Surface, J. Electron. Mater. 46 (2017) 3463–3471.
[31] D.-T. Pham, K. Gentz, C. Zörlein, N.T.M. Hai, S.-L. Tsay, B. Kirchner, S. Kossmann, K. Wandelt, P. Broekmann, Surface redox chemistry of adsorbed viologens on Cu(100), New J Chem 30 (2006) 1439–1451.
[32] G. Andreasen, M.E. Vela, R.C. Salvarezza, A.J. Arvia, Dynamics of Pyridine Adsorption on Gold(111) Terraces in Acid Solution from in-Situ Scanning Tunneling Microscopy under Potentiostatic Control, Langmuir 13 (1997) 6814–6819.
[33] A. Jeindl, J. Domke, L. Hörmann, F. Sojka, R. Forker, T. Fritz, O.T. Hofmann, Nonintuitive Surface Self-Assembly of Functionalized Molecules on Ag(111), ACS Nano 15 (2021) 6723–6734.
[34] J. Álvarez-Malmagro, F. Prieto, M. Rueda, A. Rodes, In situ Fourier transform infrared reflection absortion spectroscopy study of adenine adsorption on gold electrodes in basic media, Electrochem. New Era 140 (2014) 476–481.
[35] K. Tonigold, A. Groß, Adsorption of small aromatic molecules on the (111) surfaces of noble metals: A density functional theory study with semiempirical corrections for dispersion effects, J. Chem. Phys. 132 (2010) 224701.
[36] S.A. Kislenko, V.A. Nikitina, R.R. Nazmutdinov, A molecular dynamics study of the ionic and molecular permeability of alkanethiol monolayers on the gold electrode surface, High Energy Chem. 49 (2015) 341–346.
[37] F. Gossenberger, F. Juarez, A. Groß, Sulfate, Bisulfate, and Hydrogen Co-adsorption on Pt(111) and Au(111) in an Electrochemical Environment, Front. Chem. 8 (2020).

[38] V. Grozovski, V. Ivaništšev, H. Kasuk, T. Romann, E. Lust, Balance of the interfacial interactions of 4,4′-bipyridine at Bi(111) surface, Electrochimica Acta 120 (2014) 86–95.
[39] O. Oll, T. Romann, P. Pikma, E. Lust, Spectroscopy study of ionic liquid restructuring at lead interface, J. Electroanal. Chem. 778 (2016) 41–48.
[40] M.-A. Dubois, O. Guillermet, S. Gauthier, G. Zhan, Y. Makoudi, F. Palmino, X. Bouju, A. Rochefort, Influence of Cu adatoms on the molecular assembly of 4,4′-bipyridine on Cu(111), Phys Chem Chem Phys 20 (2018) 15350–15357.
[41] G. Gorbatovski, O. Oll, H. Kasuk, P. Pikma, E. Lust, In situ scanning tunneling microscopy study of bipyridine adsorption at semi-metallic Sb(111) plane, Electrochem. Commun. 105 (2019) 106500.
[42] Y.-X. Diao, M.-J. Han, L.-J. Wan, K. Itaya, T. Uchida, H. Miyake, A. Yamakata, M. Osawa, Adsorbed structures of 4,4′-bipyridine on Cu(111) in acid studied by STM and IR, Langmuir 22 (2006) 3640–3646.
[43] F. Cunha, N.J. Tao, X.W. Wang, Q. Jin, B. Duong, J. D′Agnese, Potential-Induced Phase Transitions in 2,2′ -Bipyridine and 4,4′ -Bipyridine Monolayers on Au(111) Studied by in Situ Scanning Tunneling Microscopy and Atomic Force Microscopy, Langmuir 12 (1996) 6410–6418.
[44] D. Mayer, T. Dretschkow, K. Ataka, T. Wandlowski, Structural transitions in 4,4′-bipyridine adlayers on Au(111) – an electrochemical and in-situ STM-study, J. Electroanal. Chem. 524 (2002) 20–35.
[45] P. Pikma, H. Kasuk, O. Oll, V. Ivaništšev, T. Romann, V. Grozovski, K. Lust, E. Lust, Adsorption of 4,4′−bipyridine on the Cd(0001) single crystal electrode surface, Electrochimica Acta 180 (2015) 965–976.
[46] P. Walden, Ueber die Molekulargrösse und elektrische Leitfähigkeit einiger geschmolzenen Salze, Proc. Imp. Acad. Sci. 8 (1914) 405–422.
[47] J.S. Wilkes, M.J. Zaworotko, Air and water stable 1-ethyl-3-methylimidazolium based ionic liquids, J Chem Soc Chem Commun (1992) 965–967.
[48] S.K. Singh, A.W. Savoy, Ionic liquids synthesis and applications: An overview, J. Mol. Liq. 297 (2020) 112038.
[49] I. Krossing, J.M. Slattery, C. Daguenet, P.J. Dyson, A. Oleinikova, H. Weingärtner, Why Are Ionic Liquids Liquid? A Simple Explanation Based on Lattice and Solvation Energies, J. Am. Chem. Soc. 128 (2006) 13427–13434.
[50] Y. Hu, X. Peng, Effect of the Structures of Ionic Liquids on Their Physical Chemical Properties, in: S. Zhang, J. Wang, X. Lu, Q. Zhou (Eds.), Struct. Interact. Ion. Liq., Springer Berlin Heidelberg, Berlin, Heidelberg, 2014: pp. 141–174.
[51] T. Tooming, T. Thomberg, L. Siinor, K. Tõnurist, A. Jänes, E. Lust, A Type High Capacitance Supercapacitor Based on Mixed Room Temperature Ionic Liquids Containing Specifically Adsorbed Iodide Anions, J. Electrochem. Soc. 161 (2014) A222–A227.
[52] G. Lota, E. Frackowiak, Striking capacitance of carbon/iodide interface, Electrochem. Commun. 11 (2009) 87–90.
[53] J. Zhao, G. Gorbatovski, O. Oll, T. Thomberg, E. Lust, Effect of alkali and halide ion doping on the energy storage characteristics of ionic liquid based supercapacitors, Electrochimica Acta 319 (2019) 82–87.
[54] T. Zhou, C. Gui, L. Sun, Y. Hu, H. Lyu, Z. Wang, Z. Song, G. Yu, Energy Applications of Ionic Liquids: Recent Developments and Future Prospects, Chem. Rev. 123 (2023) 12170–12253.

[55] R.L. Vekariya, A review of ionic liquids: Applications towards catalytic organic transformations, J. Mol. Liq. 227 (2017) 44–60.
[56] Z.S. Qureshi, K.M. Deshmukh, B.M. Bhanage, Applications of ionic liquids in organic synthesis and catalysis, Clean Technol. Environ. Policy 16 (2014) 1487–1513.
[57] T. Itoh, Ionic Liquids as Tool to Improve Enzymatic Organic Synthesis, Chem. Rev. 117 (2017) 10567–10607.
[58] Z. Zhang, J. Song, B. Han, Catalytic Transformation of Lignocellulose into Chemicals and Fuel Products in Ionic Liquids, Chem. Rev. 117 (2017) 6834–6880.
[59] F. Pena-Pereira, J. Namieśnik, Ionic Liquids and Deep Eutectic Mixtures: Sustainable Solvents for Extraction Processes, ChemSusChem 7 (2014) 1784–1800.
[60] C.F. Poole, S.K. Poole, Extraction of organic compounds with room temperature ionic liquids, Extr. Tech. 1217 (2010) 2268–2286.
[61] A.P. de los Ríos, F.J. Hernández-Fernández, L.J. Lozano, S. Sánchez, J.I. Moreno, C. Godínez, Removal of Metal Ions from Aqueous Solutions by Extraction with Ionic Liquids, J. Chem. Eng. Data 55 (2010) 605–608.
[62] H. Shirota, E.W. Castner, Physical Properties and Intermolecular Dynamics of an Ionic Liquid Compared with Its Isoelectronic Neutral Binary Solution, J. Phys. Chem. A 109 (2005) 9388–9392.
[63] F. Philippi, D. Rauber, K.L. Eliasen, N. Bouscharain, K. Niss, C.W.M. Kay, T. Welton, Pressing matter: why are ionic liquids so viscous?, Chem Sci 13 (2022) 2735–2743.
[64] J.G. McDaniel, A. Yethiraj, Understanding the Properties of Ionic Liquids: Electrostatics, Structure Factors, and Their Sum Rules, J. Phys. Chem. B 123 (2019) 3499–3512.
[65] G. Feng, M. Chen, S. Bi, Z.A. Goodwin, E.B. Postnikov, N. Brilliantov, M. Urbakh, A.A. Kornyshev, Free and bound states of ions in ionic liquids, conductivity, and underscreening paradox, Phys. Rev. X 9 (2019) 021024.
[66] Z. Hu, J. Vatamanu, O. Borodin, D. Bedrov, A molecular dynamics simulation study of the electric double layer and capacitance of [BMIM][PF6] and [BMIM][BF4] room temperature ionic liquids near charged surfaces., Phys. Chem. Chem. Phys. 15 (2013) 14234–14247.
[67] V. Ivaništšev, M.V. Fedorov, Interfaces between Charged Surfaces and Ionic Liquids: Insights from Molecular Simulations, Electrochem. Soc. Interface 23 (2014) 65–69.
[68] Z. Hu, J. Vatamanu, O. Borodin, D. Bedrov, A comparative study of alkylimidazolium room temperature ionic liquids with FSI and TFSI anions near charged electrodes, Electrochimica Acta 145 (2014) 40–52.
[69] C. Merlet, D.T. Limmer, M. Salanne, R. van Roij, P.A. Madden, D. Chandler, B. Rotenberg, The Electric Double Layer Has a Life of Its Own, J. Phys. Chem. C 118 (2014) 18291–18298.
[70] M.V. Fedorov, A.A. Kornyshev, Towards understanding the structure and capacitance of electrical double layer in ionic liquids, Electrochimica Acta 53 (2008) 6835–6840.
[71] R. Atkin, S.Z.E. Abedin, R. Hayes, L.H.S. Gasparotto, N. Borisenko, F. Endres, AFM and STM Studies on the Surface Interaction of [BMP]TFSA and [EMIm]TFSA Ionic Liquids with Au(111), J. Phys. Chem. C 113 (2009) 13266–13272.

[72] S. Perkin, L. Crowhurst, H. Niedermeyer, T. Welton, A.M. Smith, N.N. Gosvami, Self-assembly in the electrical double layer of ionic liquids, Chem. Commun. 47 (2011) 6572–6574.
[73] G. Gouy, Sur la constitution de la charge electrique a la surface dun electrolyte, J Phys Theor Appl 9 (1910) 457–458.
[74] D.L. Chapman, LI. A contribution to the theory of electrocapillarity, Lond. Edinb. Dublin Philos. Mag. J. Sci. 25 (1913) 475–481.
[75] Z.A.H. Goodwin, G. Feng, A.A. Kornyshev, Mean-Field Theory of Electrical Double Layer In Ionic Liquids with Account of Short-Range Correlations, Electrochimica Acta 225 (2017) 190–197.
[76] A.A. Kornyshev, Double-Layer in Ionic Liquids: Paradigm Change?, J. Phys. Chem. B 111 (2007) 5545–5557.
[77] S. Lamperski, C.W. Outhwaite, L.B. Bhuiyan, The Electric Double-Layer Differential Capacitance at and near Zero Surface Charge for a Restricted Primitive Model Electrolyte, J. Phys. Chem. B 113 (2009) 8925–8929.
[78] M.Z. Bazant, B.D. Storey, A.A. Kornyshev, Double Layer in Ionic Liquids: Overscreening versus Crowding, Phys. Rev. Lett. 106 (2011) 046102–4.
[79] J.P. de Souza, Z.A.H. Goodwin, M. McEldrew, A.A. Kornyshev, M.Z. Bazant, Interfacial Layering in the Electric Double Layer of Ionic Liquids, Phys Rev Lett 125 (2020) 116001.
[80] M.V. Fedorov, A.A. Kornyshev, Ionic Liquid Near a Charged Wall: Structure and Capacitance of Electrical Double Layer, J. Phys. Chem. B 112 (2008) 11868–11872.
[81] Y.-J. Tu, S.-C. Wu, J.G. McDaniel, Importance of Anion–Anion Pairing for Capacitance of Carbon/Ionic Liquid Interfaces, J. Phys. Chem. C 126 (2022) 20213–20225.
[82] I.V. Voroshylova, M. Lembinen, H. Ers, M. Mišin, V.A. Koverga, C.M. Pereira, V.B. Ivaništšev, M.N.D.S. Cordeiro, On the role of the surface charge plane position at Au(*hkl*)–BMImPF_6 interfaces, Electrochimica Acta 318 (2019) 76–82.
[83] T. Pajkossy, R. Jurczakowski, Electrochemical impedance spectroscopy in interfacial studies, Curr. Opin. Electrochem. 1 (2017) 53–58.
[84] V. Ivaništšev, A. Ruzanov, K. Lust, E. Lust, Comparative Impedance Study of Cd(0001) Electrode in EMImBF4 and KI Aqueous Solution at Different Temperatures, J. Electrochem. Soc. 160 (2013) H368–H375.
[85] E. Anderson, V. Grozovski, L. Siinor, C. Siimenson, E. Lust, Comparative in situ STM, cyclic voltammetry and impedance spectroscopy study of Bi(111) | 1-ethyl-3-methylimidazolium tetrafluoroborate interface, J. Electroanal. Chem. 758 (2015) 201–208.
[86] P.-Y. Chen, I.-W. Sun, Electrochemical study of copper in a basic 1-ethyl-3-methylimidazolium tetrafluoroborate room temperature molten salt, Electrochimica Acta 45 (1999) 441–450.
[87] Y. Katayama, S. Dan, T. Miura, T. Kishi, Electrochemical behavior of silver in 1-ethyl-3-methylimidazolium tetrafluoroborate molten salt, J. Electrochem. Soc. 148 (2001) C102.
[88] H. Ers, M. Lembinen, M. Mišin, A.P. Seitsonen, M.V. Fedorov, V.B. Ivaništšev, Graphene–Ionic Liquid Interfacial Potential Drop from Density Functional Theory-Based Molecular Dynamics Simulations, J. Phys. Chem. C 124 (2020) 19548–19555.

[89] R. Burt, G. Birkett, M. Salanne, X.S. Zhao, Molecular Dynamics Simulations of the Influence of Drop Size and Surface Potential on the Contact Angle of Ionic-Liquid Droplets, J. Phys. Chem. C 120 (2016) 15244–15250.
[90] C. Merlet, M. Salanne, B. Rotenberg, New Coarse-Grained Models of Imidazolium Ionic Liquids for Bulk and Interfacial Molecular Simulations, J. Phys. Chem. C 116 (2012) 7687–7693.
[91] P. Pikma, L. Siinor, O. Oll, E. Lust, Formation of 2,2′-bipyridine adlayers at Sb(111)|ionic liquid + 2,2′-bipyridine solution interface, Electrochem. Commun. 61 (2015) 61–65.
[92] P. Pikma, L. Siinor, S. Selberg, E. Lust, In Situ STM Studies of Electrochemically Polished Cd(0001) Electrode in 1-Ethyl-3-Methylimidazolium Tetrafluoroborate, ECS Trans. 66 (2015) 41–47.
[93] L. Siinor, K. Lust, E. Lust, Electrical Double Layer Capacitance at Bi(111) | 1-Ethyl-3-methylimidazolium Tetrafluoroborate Interface as a Function of the Electrode Potential, J. Electrochem. Soc. 157 (2010) F83–F87.
[94] T. Pajkossy, D.M. Kolb, The interfacial capacitance of Au(100) in an ionic liquid, 1-butyl-3-methyl-imidazolium hexafluorophosphate, Electrochem. Commun. 13 (2011) 284–286.
[95] R.N. Gomes, C.P. Sousa, P.N.S. Casciano, F.W.P. Ribeiro, S. Morais, P. de Lima-Neto, A.N. Correia, Dispersion of multi-walled carbon nanotubes in [BMIM]PF6 for electrochemical sensing of acetaminophen, Mater. Sci. Eng. C 88 (2018) 148–156.
[96] H. de Araujo Chagas, E.E. Fileti, G. Colherinhas, Comparing supercapacitors with graphene/graphyne electrodes and [Bmim][PF6], [Emim][BF4], [Ch][Gly] and [Pyr][Tfsi] ionic liquids using molecular dynamics, J. Mol. Liq. 379 (2023) 121703.
[97] V. Lockett, M. Horne, R. Sedev, T. Rodopoulos, J. Ralston, Differential capacitance of the double layer at the electrode/ionic liquids interface, Phys. Chem. Chem. Phys. 12 (2010) 12499–12512.
[98] M. Galiński, A. Lewandowski, I. Stępniak, Ionic liquids as electrolytes, Electrochimica Acta 51 (2006) 5567–5580.
[99] O. Oll, M. Väärtnõu, G. Gorbatovski, J. Zhao, C. Siimenson, L. Siinor, K. Lust, T. Romann, P. Pikma, E. Lust, Adsorption of anions on bismuth and cadmium single crystal plane electrodes from various solvents and ionic liquid mixtures, Electrochimica Acta 319 (2019) 895–908.
[100] S. Trasatti, E. Lust, The Potential of Zero Charge, in: R.E. White, J.O. Bockris, B.E. Conway (Eds.), Mod. Asp. Electrochem., Kluwer Academic / Plenum Publishers, New York, 1999: pp. 1–193.
[101] V. Jovanovski, S.B. Hočevar, B. Ogorevc, Bismuth electrodes in contemporary electroanalysis, Curr. Opin. Electrochem. 3 (2017) 114–122.
[102] R. Wang, H. Li, H. Sun, Bismuth: Environmental Pollution and Health Effects, in: J. Nriagu (Ed.), Encycl. Environ. Health, 2nd ed., Elsevier, Oxford, 2019: pp. 415–423.
[103] H. Mönig, J. Sun, Yu.M. Koroteev, G. Bihlmayer, J. Wells, E.V. Chulkov, K. Pohl, Ph. Hofmann, Structure of the (111) surface of bismuth: LEED analysis and first-principles calculations, Phys. Rev. B 72 (2005) 085410.
[104] Ph. Hofmann, The surfaces of bismuth: Structural and electronic properties, Prog. Surf. Sci. 81 (2006) 191–245.
[105] F. Patthey, W.-D. Schneider, H. Micklitz, Photoemission study of the Bi(111) surface, Phys Rev B 49 (1994) 11293–11296.

[106] C.R. Ast, H. Höchst, Fermi Surface of Bi(111) Measured by Photoemission Spectroscopy, Phys Rev Lett 87 (2001) 177602.
[107] C.S. Barrett, P. Cucka, K. Haefner, The crystal structure of antimony at 4.2, 78 and 298° K, Acta Crystallogr. 16 (1963) 451–453.
[108] K. Sugawara, T. Sato, S. Souma, T. Takahashi, M. Arai, T. Sasaki, Fermi Surface and Anisotropic Spin-Orbit Coupling of Sb(111) Studied by Angle-Resolved Photoemission Spectroscopy, Phys Rev Lett 96 (2006) 046411.
[109] V. Grozovski, S. Kallip, E. Lust, In situ STM studies of Sb(111) electrodes in aqueous electrolyte solutions, Surf. Sci. 613 (2013) 108–113.
[110] H. Kasuk, G. Nurk, K. Lust, E. Lust, Adsorption of uracil on bismuth single crystal planes, J. Electroanal. Chem. 580 (2005) 128–134.
[111] L. Siinor, C. Siimenson, V. Ivaništšev, K. Lust, E. Lust, Influence of cation chemical composition and structure on the double layer capacitance for Bi(111) | room temperature ionic liquid interface, J. Electroanal. Chem. 668 (2012) 30–36.
[112] E. Anderson, V. Grozovski, L. Siinor, C. Siimenson, V. Ivaništšev, K. Lust, S. Kallip, E. Lust, Influence of the electrode potential and in situ STM scanning conditions on the phase boundary structure of the single crystal Bi(1 1 1)|1-butyl-4-methylpyridinium tetrafluoroborate interface, J. Electroanal. Chem. 709 (2013) 46–56.
[113] D.A. Edwards, W.E. Wallace, R.S. Craig, Magnesium-Cadmium Alloys. IV. The Cadmium-Rich Alloys; Some Lattice Parameters and Phase Relationships between 25 and 300°. Structure of the MgCd3 Superlattice. Schottky Defects and the Anomalous Entropy1, J. Am. Chem. Soc. 74 (1952) 5256–5261.
[114] E. Lust, A. Jänes, K. Lust, R. Pullerits, Adsorption of organic compounds and hydrophilicity of bismuth, cadmium and antimony electrodes, J. Electroanal. Chem. 431 (1997) 183–201.
[115] P. Pikma, V. Grozovski, H. Kasuk, E. Lust, In situ STM studies of electrochemically polished Cd(0001) electrode in aqueous electrolyte solutions, Surf. Sci. 628 (2014) 86–91.
[116] W.P. Davey, Precision Measurements of the Lattice Constants of Twelve Common Metals, Phys Rev 25 (1925) 753–761.
[117] J.V. Barth, H. Brune, G. Ertl, R.J. Behm, Scanning tunneling microscopy observations on the reconstructed Au(111) surface: Atomic structure, long-range superstructure, rotational domains, and surface defects, Phys Rev B 42 (1990) 9307–9318.
[118] R. Hammer, A. Sander, S. Förster, M. Kiel, K. Meinel, W. Widdra, Surface reconstruction of Au(001): High-resolution real-space and reciprocal-space inspection, Phys Rev B 90 (2014) 035446.
[119] T. Gritsch, D. Coulman, R.J. Behm, G. Ertl, A scanning tunneling microscopy investigation of the structure of the Pt(110) and Au(110) surfaces, Surf. Sci. 257 (1991) 297–306.
[120] J.O. Bockris, A.K.N. Reddy, M. Gamboa-Aldeco, Modern electrochemistry: Volume 2A, 2nd ed., Kluwer Academic Publishers, New York, 2002.
[121] N. Elgrishi, K.J. Rountree, B.D. McCarthy, E.S. Rountree, T.T. Eisenhart, J.L. Dempsey, A Practical Beginner′s Guide to Cyclic Voltammetry, J. Chem. Educ. 95 (2018) 197–206.
[122] F. Marken, A. Neudeck, A.M. Bond, Cyclic Voltammetry, in: F. Scholz, A.M. Bond, R.G. Compton, D.A. Fiedler, G. Inzelt, H. Kahlert, Š. Komorsky-Lovrić, H. Lohse, M. Lovrić, F. Marken, A. Neudeck, U. Retter, F. Scholz, Z. Stojek (Eds.), Electroanal. Methods Guide Exp. Appl., Springer, Berlin, Heidelberg, 2010: pp. 57–106.

[123] A.Ch. Lazanas, M.I. Prodromidis, Electrochemical Impedance Spectroscopy – A Tutorial, ACS Meas. Sci. Au 3 (2023) 162–193.
[124] U. Retter, H. Lohse, Electrochemical Impedance Spectroscopy, in: F. Scholz (Ed.), Electroanal. Methods, Springer, Berlin, Heidelberg, 2010: pp. 159–177.
[125] A. Lasia, Electrochemical Impedance Spectroscopy and its Applications, in: B.E. Conway, J.O. Bockris, R.E. White (Eds.), Mod. Asp. Electrochem., Kluwer Academic Publishers, Boston, 2002: pp. 143–248.
[126] C. Müller, K. Németh, S. Vesztergom, T. Pajkossy, T. Jacob, The interface between HOPG and 1-butyl-3-methyl-imidazolium hexafluorophosphate, Phys Chem Chem Phys 18 (2016) 916–925.
[127] O. Oll, C. Siimenson, K. Lust, G. Gorbatovski, E. Lust, Specific adsorption from an ionic liquid: impedance study of iodide ion adsorption from a pure halide ionic liquid at bismuth single crystal planes, Electrochimica Acta 247 (2017) 910–919.
[128] H. Feng, X. Xu, Y. Du, S.X. Dou, Application of Scanning Tunneling Microscopy in Electrocatalysis and Electrochemistry, Electrochem. Energy Rev. 4 (2021) 249–268.
[129] P.K. Hansma, J. Tersoff, Scanning tunneling microscopy, J. Appl. Phys. 61 (1987) R1–R24.
[130] A. Della Pia, G. Costantini, Scanning Tunneling Microscopy, in: G. Bracco, B. Holst (Eds.), Surf. Sci. Tech., Springer, Berlin, Heidelberg, 2013: pp. 565–597.
[131] K. Gentz, K. Wandelt, Electrochemical Scanning Tunneling Microscopy, CHIMIA 66 (2012) 44.
[132] S.A. Hollingsworth, R.O. Dror, Molecular Dynamics Simulation for All, Neuron 99 (2018) 1129–1143.
[133] N. Castel, F.-X. Coudert, Atomistic Models of Amorphous Metal–Organic Frameworks, J. Phys. Chem. C 126 (2022) 6905–6914.
[134] F. Jensen, Introduction to computational chemistry, 2nd ed., John Wiley & Sons, Chichester, England ; Hoboken, NJ, 2007.
[135] D. Bedrov, J.-P. Piquemal, O. Borodin, A.D. MacKerell, B. Roux, C. Schröder, Molecular Dynamics Simulations of Ionic Liquids and Electrolytes Using Polarizable Force Fields, Chem. Rev. 119 (2019) 7940–7995.
[136] W.L. Jorgensen, D.S. Maxwell, J. Tirado-Rives, Development and Testing of the OPLS All-Atom Force Field on Conformational Energetics and Properties of Organic Liquids, J. Am. Chem. Soc. 118 (1996) 11225–11236.
[137] T.P. Senftle, S. Hong, M.M. Islam, S.B. Kylasa, Y. Zheng, Y.K. Shin, C. Junkermeier, R. Engel-Herbert, M.J. Janik, H.M. Aktulga, T. Verstraelen, A. Grama, A.C.T. van Duin, The ReaxFF reactive force-field: development, applications and future directions, Npj Comput. Mater. 2 (2016) 15011.
[138] A.D.Jr. MacKerell, D. Bashford, M. Bellott, R.L.Jr. Dunbrack, J.D. Evanseck, M.J. Field, S. Fischer, J. Gao, H. Guo, S. Ha, D. Joseph-McCarthy, L. Kuchnir, K. Kuczera, F.T.K. Lau, C. Mattos, S. Michnick, T. Ngo, D.T. Nguyen, B. Prodhom, W.E. Reiher, B. Roux, M. Schlenkrich, J.C. Smith, R. Stote, J. Straub, M. Watanabe, J. Wiórkiewicz-Kuczera, D. Yin, M. Karplus, All-Atom Empirical Potential for Molecular Modeling and Dynamics Studies of Proteins, J. Phys. Chem. B 102 (1998) 3586–3616.
[139] J. Wang, R.M. Wolf, J.W. Caldwell, P.A. Kollman, D.A. Case, Development and testing of a general amber force field, J. Comput. Chem. 25 (2004) 1157–1174.

[140] O.T. Unke, S. Chmiela, H.E. Sauceda, M. Gastegger, I. Poltavsky, K.T. Schütt, A. Tkatchenko, K.-R. Müller, Machine Learning Force Fields, Chem. Rev. 121 (2021) 10142–10186.
[141] S.A. Kislenko, I.S. Samoylov, R.H. Amirov, Molecular dynamics simulation of the electrochemical interface between a graphite surface and the ionic liquid [BMIM][PF6], Phys. Chem. Chem. Phys. 11 (2009) 5584–5590.
[142] C. Merlet, C. Péan, B. Rotenberg, P.A. Madden, P. Simon, M. Salanne, Simulating Supercapacitors: Can We Model Electrodes As Constant Charge Surfaces?, J. Phys. Chem. Lett. 4 (2013) 264–268.
[143] F. Schwarz, M. Koch, G. Kastlunger, H. Berke, R. Stadler, K. Venkatesan, E. Lörtscher, Charge Transport and Conductance Switching of Redox-Active Azulene Derivatives, Angew. Chem. Int. Ed. 55 (2016) 11781–11786.
[144] V. Tripković, E. Skúlason, S. Siahrostami, J.K. Nørskov, J. Rossmeisl, The oxygen reduction reaction mechanism on Pt(111) from density functional theory calculations, Electrochimica Acta 55 (2010) 7975–7981.
[145] P. Zhang, Y. Yang, X. Duan, Y. Liu, S. Wang, Density Functional Theory Calculations for Insight into the Heterocatalyst Reactivity and Mechanism in Persulfate-Based Advanced Oxidation Reactions, ACS Catal. 11 (2021) 11129–11159.
[146] R. Jayan, M.M. Islam, Functionalized MXenes as effective polyselenide immobilizers for lithium–selenium batteries: a density functional theory (DFT) study, Nanoscale 12 (2020) 14087–14095.
[147] X. Hu, H. Qu, L. Xu, W. Liu, T. Guo, B. Cai, X. Yu, J. Zhu, S. Zhang, DFT coupled with NEGF study of the electronic properties and ballistic transport performances of 2D SbSiTe3, Nanoscale 12 (2020) 9958–9963.
[148] O.T. Hofmann, E. Zojer, L. Hörmann, A. Jeindl, R.J. Maurer, First-principles calculations of hybrid inorganic–organic interfaces: from state-of-the-art to best practice, Phys. Chem. Chem. Phys. 23 (2021) 8132–8180.
[149] W. Kohn, L.J. Sham, Self-consistent equations including exchange and correlation effects, Phys. Rev. 140 (1965) 1133–1138.
[150] W. Koch, Max C. Holthausen, The Quest for Approximate Exchange-Correlation Functionals, in: Chem. Guide Density Funct. Theory, John Wiley & Sons, Ltd, 2001: pp. 65–91.
[151] J.P. Perdew, K. Burke, M. Ernzerhof, Generalized Gradient Approximation Made Simple, Phys. Rev. Lett. 77 (1996) 3865–3868.
[152] S. De Waele, K. Lejaeghere, M. Sluydts, S. Cottenier, Error estimates for density-functional theory predictions of surface energy and work function, Phys Rev B 94 (2016) 235418.
[153] F. Tran, R. Laskowski, P. Blaha, K. Schwarz, Performance on molecules, surfaces, and solids of the Wu-Cohen GGA exchange-correlation energy functional, Phys Rev B 75 (2007) 115131.
[154] S. Grimme, J. Antony, S. Ehrlich, H. Krieg, A consistent and accurate ab initio parametrization of density functional dispersion correction (DFT-D) for the 94 elements H-Pu, J. Chem. Phys. 132 (2010) 154104.
[155] E. Caldeweyher, C. Bannwarth, S. Grimme, Extension of the D3 dispersion coefficient model, J. Chem. Phys. 147 (2017) 034112.
[156] V.G. Ruiz, W. Liu, E. Zojer, M. Scheffler, A. Tkatchenko, Density-Functional Theory with Screened van der Waals Interactions for the Modeling of Hybrid Inorganic-Organic Systems, Phys Rev Lett 108 (2012) 146103.

[157] E. Caldeweyher, J.-M. Mewes, S. Ehlert, S. Grimme, Extension and evaluation of the D4 London-dispersion model for periodic systems, Phys Chem Chem Phys 22 (2020) 8499–8512.
[158] J. Claudot, W.J. Kim, A. Dixit, H. Kim, T. Gould, D. Rocca, S. Lebègue, Benchmarking several van der Waals dispersion approaches for the description of intermolecular interactions, J. Chem. Phys. 148 (2018) 064112.
[159] L. Martínez, R. Andrade, E.G. Birgin, J.M. Martínez, PACKMOL: A Package for Building Initial Configurations for Molecular Dynamics Simulations, J. Comput. Chem. 30 (2009) 2157–2164.
[160] B. Doherty, X. Zhong, S. Gathiaka, B. Li, O. Acevedo, Revisiting OPLS Force Field Parameters for Ionic Liquid Simulations, J. Chem. Theory Comput. 13 (2017) 6131–6145.
[161] M.J. Abraham, T. Murtola, R. Schulz, S. Páll, J.C. Smith, B. Hess, E. Lindahl, GROMACS: High performance molecular simulations through multi-level parallelism from laptops to supercomputers, SoftwareX 1 (2015) 19–25.
[162] E. Roos Nerut, K. Karu, I.V. Voroshylova, K. Kirchner, T. Kirchner, M.V. Fedorov, V.B. Ivaništšev, NaRIBaS – A Scripting Framework for Computational Modeling of Nanomaterials and Room Temperature Ionic Liquids in Bulk and Slab, Computation 6 (2018).
[163] S.V. Sambasivarao, O. Acevedo, Development of OPLS-AA Force Field Parameters for 68 Unique Ionic Liquids, J. Chem. Theory Comput. 5 (2009) 1038–1050.
[164] J.N. Canongia Lopes, J. Deschamps, A.A.H. Pádua, Modeling Ionic Liquids Using a Systematic All-Atom Force Field, J. Phys. Chem. B 108 (2004) 2038–2047.
[165] H. Heinz, R.A. Vaia, B.L. Farmer, R.R. Naik, Accurate Simulation of Surfaces and Interfaces of Face-Centered Cubic Metals Using 12−6 and 9−6 Lennard-Jones Potentials, J. Phys. Chem. C 112 (2008) 17281–17290.
[166] G. Bussi, D. Donadio, M. Parrinello, Canonical sampling through velocity rescaling, J. Chem. Phys. 126 (2007) 014101.
[167] R.W. Hockney, S.P. Goel, J.W. Eastwood, Quiet high-resolution computer models of a plasma, J. Comput. Phys. 14 (1974) 148–158.
[168] J. Enkovaara, C. Rostgaard, J.J. Mortensen, J. Chen, M. Dułak, L. Ferrighi, J. Gavnholt, C. Glinsvad, V. Haikola, H.A. Hansen, H.H. Kristoffersen, M. Kuisma, A.H. Larsen, L. Lehtovaara, M. Ljungberg, O. Lopez-Acevedo, P.G. Moses, J. Ojanen, T. Olsen, V. Petzold, N.A. Romero, J. Stausholm-Møller, M. Strange, G.A. Tritsaris, M. Vanin, M. Walter, B. Hammer, H. Häkkinen, G.K.H. Madsen, R.M. Nieminen, J.K. Nørskov, M. Puska, T.T. Rantala, J. Schiøtz, K.S. Thygesen, K.W. Jacobsen, Electronic structure calculations with GPAW: a real-space implementation of the projector augmented-wave method, J. Phys. Condens. Matter 22 (2010) 253202.
[169] H.J. Monkhorst, J.D. Pack, Special points for Brillouin-zone integrations, Phys. Rev. B 13 (1976) 5188–5192.
[170] D. Nečas, P. Klapetek, Gwyddion: an open-source software for SPM data analysis, Cent. Eur. J. Phys. 10 (2012) 181–188.
[171] L. Hörmann, A. Jeindl, A.T. Egger, M. Scherbela, O.T. Hofmann, SAMPLE: Surface structure search enabled by coarse graining and statistical learning, Comput. Phys. Commun. 244 (2019) 143–155.
[172] M. Todorović, M.U. Gutmann, J. Corander, P. Rinke, Bayesian inference of atomistic structure in functional materials, Npj Comput. Mater. 5 (2019) 35.

[173] A.H. Larsen, J.J. Mortensen, J. Blomqvist, I.E. Castelli, R. Christensen, M. Dulak, J. Friis, M.N. Groves, B. Hammer, C. Hargus, E.D. Hermes, P.C. Jennings, P.B. Jensen, J. Kermode, J.R. Kitchin, E.L. Kolsbjerg, J. Kubal, K. Kaasbjerg, S. Lysgaard, J.B. Maronsson, T. Maxson, T. Olsen, L. Pastewka, A. Peterson, C. Rostgaard, J. Schiøtz, O. Schütt, M. Strange, K.S. Thygesen, T. Vegge, L. Vilhelmsen, M. Walter, Z. Zeng, K.W. Jacobsen, The atomic simulation environment – a Python library for working with atoms, J. Phys. Condens. Matter 29 (2017) 273002.

[174] J.J. Mortensen, L.B. Hansen, K.W. Jacobsen, Real-space grid implementation of the projector augmented wave method, Phys. Rev. B 71 (2005) 035109.

[175] A.H. Larsen, M. Vanin, J.J. Mortensen, K.S. Thygesen, K.W. Jacobsen, Localized atomic basis set in the projector augmented wave method, Phys Rev B 80 (2009) 195112.

[176] E. Caldeweyher, S. Ehlert, A. Hansen, H. Neugebauer, S. Spicher, C. Bannwarth, S. Grimme, A generally applicable atomic-charge dependent London dispersion correction, J. Chem. Phys. 150 (2019) 154122.

[177] P.A.Z. Suarez, V.M. Selbach, J.E.L. Dullius, S. Einloft, C.M.S. Piatnicki, D.S. Azambuja, R.F. de Souza, J. Dupont, Enlarged electrochemical window in dialkyl-imidazolium cation based room-temperature air and water-stable molten salts, Electrochimica Acta 42 (1997) 2533–2535.

[178] M. Sha, Q. Dou, F. Luo, G. Zhu, G. Wu, Molecular Insights into the Electric Double Layers of Ionic Liquids on Au(100) Electrodes, ACS Appl. Mater. Interfaces 6 (2014) 12556–12565.

[179] H. Li, J. Wang, G.G. Warr, R. Atkin, Extremely slow dynamics of ionic liquid self-assembled nanostructures near a solid surface, J. Colloid Interface Sci. 630 (2023) 658–665.

[180] I.V. Voroshylova, H. Ers, B. Docampo-Álvarez, P. Pikma, V.B. Ivaništšev, M.N.D.S. Cordeiro, Hysteresis in the MD Simulations of Differential Capacitance at the Ionic Liquid–Au Interface, J. Phys. Chem. Lett. 11 (2020) 10408–10413.

[181] B. Rotenberg, M. Salanne, Structural Transitions at Ionic Liquid Interfaces, J. Phys. Chem. Lett. 6 (2015) 4978–4985.

[182] S.A. Kislenko, R.H. Amirov, I.S. Samoylov, Influence of temperature on the structure and dynamics of the [BMIM][PF6] ionic liquid/graphite interface, Phys. Chem. Chem. Phys. 12 (2010) 11245–11250.

[183] F. Silva, C. Gomes, M. Figueiredo, R. Costa, A. Martins, C.M. Pereira, The electrical double layer at the [BMIM][PF6] ionic liquid/electrode interface: Effect of temperature on the differential capacitance, J. Electroanal. Chem. 622 (2008) 153–160.

[184] L. Siinor, R. Arendi, K. Lust, E. Lust, Influence of temperature on the electrochemical characteristics of Bi(111)|ionic liquid interface, J. Electroanal. Chem. 689 (2013) 51–56.

[185] J. Vatamanu, L. Xing, W. Li, D. Bedrov, Influence of temperature on the capacitance of ionic liquid electrolytes on charged surfaces., Phys. Chem. Chem. Phys. (2014).

[186] M. Drüschler, N. Borisenko, J. Wallauer, C. Winter, B. Huber, F. Endres, B. Roling, New insights into the interface between a single-crystalline metal electrode and an extremely pure ionic liquid: slow interfacial processes and the influence of temperature on interfacial dynamics, Phys. Chem. Chem. Phys. 14 (2012) 5090–5099.

[187] M. Chen, Z.A.H. Goodwin, G. Feng, A.A. Kornyshev, On the temperature dependence of the double layer capacitance of ionic liquids, J. Electroanal. Chem. 819 (2018) 347–358.
[188] J. Xia, F. Chen, J. Li, N. Tao, Measurement of the quantum capacitance of graphene, Nat. Nanotechnol. 4 (2009) 505–509.
[189] C. Zhan, Y. Zhang, P.T. Cummings, D. Jiang, Enhancing graphene capacitance by nitrogen: effects of doping configuration and concentration, Phys Chem Chem Phys 18 (2016) 4668–4674.
[190] M.D. Stoller, C.W. Magnuson, Y. Zhu, S. Murali, J.W. Suk, R. Piner, R.S. Ruoff, Interfacial capacitance of single layer graphene, Energy Environ. Sci. 4 (2011) 4685–4689.
[191] O. Oll, T. Romann, C. Siimenson, E. Lust, Influence of chemical composition of electrode material on the differential capacitance characteristics of the ionic liquid|electrode interface, Electrochem. Commun. 82 (2017) 39–42.
[192] G. Shen, Y. Sun, Y. Wang, X. Lu, X. Ji, Interfacial structure and differential capacitance of ionic liquid/graphite interface: A perturbed-chain SAFT density functional theory study, J. Mol. Liq. 310 (2020) 113199.
[193] E. Paek, A.J. Pak, G.S. Hwang, A Computational Study of the Interfacial Structure and Capacitance of Graphene in [BMIM][PF6] Ionic Liquid, J. Electrochem. Soc. 160 (2013) A1–A10.
[194] J. Zhao, G. Gorbatovski, O. Oll, E. Anderson, E. Lust, Influence of water on the electrochemical characteristics and nanostructure of Bi(hkl) │Ionic liquid interface, Electrochimica Acta 415 (2022) 140263.
[195] V. Grozovski, H. Kasuk, S. Kallip, E. Lust, Adsorption of thiourea on Bi(111) electrode surface, J. Electroanal. Chem. 712 (2014) 103–112.
[196] S. Kallip, E. Lust, In situ STM studies of Bi(111) electrodes in aqueous electrolyte solutions, Electrochem. Commun. 7 (2005) 863–867.
[197] B. Ratschmeier, B. Braunschweig, Role of imidazolium cations on the interfacial structure of room-temperature ionic liquids in contact with Pt(111) electrodes, Electrochem. Sci. Adv. 3 (2023) e2100173.
[198] M.E. Orazem, N. Pébère, B. Tribollet, Enhanced Graphical Representation of Electrochemical Impedance Data, J. Electrochem. Soc. 153 (2006) B129–B136.
[199] L. Siinor, K. Lust, E. Lust, Influence of anion composition and size on the double layer capacitance for Bi(111) | room temperature ionic liquid interface, Electrochem. Commun. 12 (2010) 1058–1061.
[200] M. Drüschler, B. Huber, S. Passerini, B. Roling, Hysteresis Effects in the Potential-Dependent Double Layer Capacitance of Room Temperature Ionic Liquids at a Polycrystalline Platinum Interface, J. Phys. Chem. C 114 (2010) 3614–3617.
[201] R. Hayes, N. Borisenko, M.K. Tam, P.C. Howlett, F. Endres, R. Atkin, Double Layer Structure of Ionic Liquids at the Au(111) Electrode Interface: An Atomic Force Microscopy Investigation, J. Phys. Chem. C 115 (2011) 6855–6863.
[202] Y. Yokota, T. Harada, K. Fukui, Direct observation of layered structures at ionic liquid/solid interfaces by using frequency-modulation atomic force microscopy, Chem. Commun. 46 (2010) 8627–8629.
[203] K. Kirchner, T. Kirchner, V. Ivaništšev, M.V. Fedorov, Electrical double layer in ionic liquids: Structural transitions from multilayer to monolayer structure at the interface, Electrochimica Acta 110 (2013) 762–771.

[204] A.M. Smith, K.R.J. Lovelock, N.N. Gosvami, P. Licence, A. Dolan, T. Welton, S. Perkin, Monolayer to Bilayer Structural Transition in Confined Pyrrolidinium-Based Ionic Liquids, J. Phys. Chem. Lett. 4 (2013) 378–382.
[205] L. Bou Tannous, M. Simoes Santos, Z. Gong, P.-H. Haumesser, A. Benayad, A.A.H. Padua, A. Steinberger, Effect of Surface Chemistry on the Electrical Double Layer in a Long-Chain Ionic Liquid, Langmuir 39 (2023) 16785–16796.
[206] Y. Jiang, J. Li, G. Su, N. Ferri, W. Liu, A. Tkatchenko, Tuning the work function of stepped metal surfaces by adsorption of organic molecules, J. Phys. Condens. Matter 29 (2017) 204001.
[207] S. Trasatti, Adsorption of organic substances at electrodes: Recent advances, Electrochimica Acta 37 (1992) 2137–2144.

9. SUMMARY IN ESTONIAN

Adsorptsioon ja elektrilise kaksikkihi struktuur mudelelektrood – ioonvedelik piirpindadel

Elektroodi ja elektrolüüdi piirpinnal toimuvate protsesside mõistmine molekulide tasandil on vajalik arendamaks efektiivsemaid ja jätkusuutlikumaid tehnoloogilisi lahendusi. Käesolev doktoritöö keskendus elektroodi ja ioonvedeliku vahelise piirpinna struktuuri ja selles toimuvate adsorptsiooniprotsesside kirjeldamisele. Selleks, et omandada mitmekülgset arusaama piirpinnal toimuvast, kasutati erinevaid mõõtetehnikaid nagu tsükliline voltamperomeetria, elektriline impedantsspektroskoopia ja skaneeriv tunnelmikroskoopia. Samuti viidi läbi tihedusfunktsionaali teoorial põhinevaid arvutusi ja molekulaardünaamika simulatsioone, et selgitada välja elektroodi pinnale adsorbeerunud molekulide/ioonide kihtide struktuure või nende muutusi piirpinna lähedal.

Au(001) | $BMImPF_6$ ja grafeen | $EMImBF_4$ molekulaardünaamika simulatsioonid võimaldasid vaadelda piirpinda ioonide tasandil ning seostada mahtuvuse (C) väärtusi struktuuri ning temperatuuriga (T). Simulatsioonide tulemused näitasid, et mahtuvuse potentsiaalist sõltuvuse platood ja maksimumid on seostatavad muutustega elektroodi ja ioonvedeliku elektrilise kaksikkihi struktuuris. Neid muutusi saab kirjeldada ioonvedeliku kahe kihi mudeliga, mis seostas mahtuvuse potentsiaalist sõltuvuse karakteristlikke kohti elektroodi laengu ülevarjestamisega (λ) ja ioonvedeliku ioonide ümberorienteerumisega (l ja δ). Temperatuur mõjutas piirpinna mahtuvust eelkõige null-laengu potentsiaali lähedal, kus T kasv põhjustas mahtuvuse vähenemist ($\mathrm{d}C/\mathrm{d}T < 0$). Tulenevalt asjaolust, et T ei mõjutanud ioonide kihtide asukohti, siis järeldati, et λ sõltub temperatuurist, kuid l ja δ mitte. Grafeeni kvantmahtuvuse (C_Q) arvestamine piirpinna mahtuvuse hindamisel vähendas oluliselt selle temperatuurisõltuvust ning muutis ka mahtuvuse potentsiaalist sõltuvuse kuju. Mahtuvuskõvera kuju muutumine tõi esile ka elektroodi omaduste korrektse kirjeldamise olulisuse.

Uurimused, mis vaatlesid 4,4′-bipüridiini (4,4′-BP) adsorptsiooni Bi(111), Sb(111) ja Cd(0001) elektroodi ning $EMImBF_4$ ioonvedeliku piirpinnal tõid esile elektroodi omaduste mõju adsorptsioonile ja orgaaniliste kõrgstruktureeritud kihtide moodustumise võimalustele. Elektrokeemilise impedantsspektroskoopia tulemused kinnitasid tiheda 4,4′-bipüridiini kihi moodustumist kõigil uuritud elektroodi pindadel. Siiski näitasid skaneeriva tunnelmikroskoopia tulemused erinevusi 4,4′-BP adsorbeerunud struktuurides: mitmekihiline struktuur Sb(111) pinnal, viirutatud koadsorbeerunud struktuur Bi(111) pinnal ja klastrid Cd(0001) pinnal. Võrdlus varasemate 4,4′-BP adsorptsiooni uuringutega vesilahustes näitas elektrolüüdi märkimisväärset mõju nii piirpinnal toimuvatele protsessidele kui ka 4,4′-BP struktuuridele. Korrapäraste adsorbeerunud kihtide moodustumine ioonvedelikus oli märgatavalt aeglasem kui vesilahustes. Samuti tekkisid pinnale erinevad 4,4′-BP struktuurid – mitmekihilistest korrapärasest struktuurist klastriteni.

Seetõttu, kuna nii elektroodi kui ka elektrolüüdi valik mõjutab oluliselt orgaanika adsorptsiooni, tuleb veenduda valitud piirpinna sobivuses potentsiaalse rakenduse jaoks nanoelektroonikas või energiasalvestuses. Sellest lähtuvalt on ioonvedelike laiemaks kasutuselevõtuks vajalik uurida süstemaatiliselt nende piirpindade omadusi ja neid mõjutavaid faktoreid.

10. ACKNOWLEDGEMENTS

I would like to express my sincere gratitude to my supervisors, who have contributed to my growth as a scientist and as a person. Thanks to Vladislav, I was introduced to physical chemistry as well as ionic liquids and acquired my knowledge of simulations and modelling of the interfaces. He has been the source of boundless optimism. Piret opened the door to experimental electrochemistry, widening my skillset and perspective on interpreting both computational and experimental results. I′m very grateful for the effort she put into the development of my presentation, project writing, and communication skills while nurturing self-confidence. Furthermore, showing that excellence can be achieved without losing work-life balance has inspired me tremendously. Enn′s vast experience and knowledge have provided me invaluable input to conduct research, while reminding me that there is still much to learn.

I would also like to thank everyone who have helped and contributed to my work. Special thanks to Liis, with whom we have spent long hours examining the measurement results alongside other topics and has always provided her opinion while being open for discussions. I am grateful to Ove and Jaak, who have always emphasised not to jump into conclusions without careful data analysis, along with Thomas, showing the more applicable nature of electrochemical studies. Moreover, Marta, Karl Ander, Laura, Miriam, Kenneth, Wiljar and other doctoral students have ensured that there is never a dull day in Chemicum.

Finally, I am grateful to my family and friends, who have supported me in my endeavours. I have always found support from my parents to continue on this path, while my partner Mariethe, although having a medical degree, has patiently heard each and every one of my presentations and provided her expert insights and encouragement.

The present study was performed at the Institute of Chemistry of the University of Tartu and was financially supported by the Estonian Research Council grant PSG249, by the EU through the European Regional Development Fund under project TK141 (2014-2020.4.01.15-0011), by the Estonian Ministry of Education and Research (TK210), and by the project ″Increasing the knowledge intensity of Ida-Viru entrepreneurship″ (ÕÜF12) co-funded by the European Union.

11. PUBLICATIONS

CURRICULUM VITAE

Name: Heigo Ers
Date of birth: January 27, 1995
Citizenship: Estonian
Contact: Institute of Chemistry, University of Tartu, Ravila 14a, 50411, Tartu, Estonia
E-mail: heigoers@ut.ee

Education:

2020–…	University of Tartu, Institute of Chemistry, PhD Student
2018–2020	University of Tartu, Institute of Chemistry, MSc *cum laude* (Chemistry)
2014–2018	University of Tartu, Institute of Chemistry, BSc *cum laude* (Chemistry)

Professional employment:

2021–…	University of Tartu, Faculty of Science and Technology, Institute of Chemistry, Specialist
2018–2019	University of Tartu, Faculty of Science and Technology, Institute of Ecology and Earth Sciences, Specialist

Scientific publications:

1. **H. Ers**, L. Siinor, P. Pikma, Maintaining the order: 4,4′-bipyridine self-assembled layers on the Bi(111) | ionic liquid interface, Electrochim. Acta (2024) 144081.
2. L. Siinor, **H. Ers**, P. Pikma, Another Piece of the Ionic Liquid′s Puzzle: Adsorption of Cl^- Ions, J. Phys. Chem. C 128 (2024) 2722–2729.
3. L. Siinor, **H. Ers**, P. Pikma, The adsorption of organic molecules and inorganic ions – case studies in aqueous, organic and ionic liquid electrolytes, in: K. Wandelt, G. Bussetti (Eds.), Encyclopedia of Solid-Liquid Interfaces (First Edition), Elsevier, Oxford, 2024: pp. 681–691.
4. **H. Ers**, L. Siinor, P. Pikma, The adsorption of 4,4′-bipyridine at a Cd(0001)| ionic liquid interface – The descent into disorder, Electrochem. Commun. 148 (2023) 107451.
5. **H. Ers**, P. Pikma, R. Palm, M. Paalo, A. Jänes, T. Thomberg, M. Härmas, R. Härmas, L. Kalder, L.-K. Salvan, P. Teppor, R. Jäger, H. Kasuk, J. Nerut, S. Sepp, G. Nurk, K. Lust, E. Lust, Teaching electrochemistry and student participation in the development of sustainable electricity generation/storage devices at the Institute of Chemistry of the University of Tartu, J Solid State Electrochem (2023).

6. P. Pikma, **H. Ers**, L. Siinor, J. Zhao, O. Oll, T. Romann, V. Grozovski, C. Siimenson, M. Väärtnõu, M. Paalo, R. Härmas, K. Lust, T. Thomberg, A. Jänes, J. Nerut, R. Jäger, P. Valk, I. Kivi, M. Maide, P. Möller, R. Kanarbik, G. Nurk, E. Lust, The review of advances in interfacial electrochemistry in Estonia: electrochemical double layer and adsorption studies for the development of electrochemical devices, J Solid State Electrochem (2022).
7. **H. Ers**, I.V. Voroshylova, P. Pikma, V.B. Ivaništšev, Double layer in ionic liquids: Temperature effect and bilayer model, J. Mol. Liq. 363 (2022) 119747.
8. **H. Ers**, L. Siinor, C. Siimenson, E. Lust, P. Pikma, Order beyond a monolayer: The story of two self-assembled 4,4′-bipyridine layers on the Sb(111) | ionic liquid interface, Electrochim. Acta 421 (2022) 140468.
9. **H. Ers**, J. Nerut, E. Lust, P. Pikma, Long-term stability of Cd(0001) single crystal | ionic liquid interface – The effect of I^- addition, J. Electroanal. Chem. 903 (2021) 115826.
10. I.V. Voroshylova, **H. Ers**, V. Koverga, B. Docampo-Álvarez, P. Pikma, V.B. Ivaništšev, M.N.D.S. Cordeiro, Ionic liquid–metal interface: The origins of capacitance peaks, Electrochim. Acta 379 (2021) 138148.
11. I.V. Voroshylova, **H. Ers**, B. Docampo-Álvarez, P. Pikma, V.B. Ivaništšev, M.N.D.S. Cordeiro, Hysteresis in the MD Simulations of Differential Capacitance at the Ionic Liquid–Au Interface, J. Phys. Chem. Lett. 11 (2020) 10408–10413.
12. **H. Ers**, M. Lembinen, M. Mišin, A.P. Seitsonen, M.V. Fedorov, V.B. Ivaništšev, Graphene–Ionic Liquid Interfacial Potential Drop from Density Functional Theory-Based Molecular Dynamics Simulations, J. Phys. Chem. C 124 (2020) 19548–19555.
13. M. Lembinen, E. Nõmmiste, **H. Ers**, B. Docampo-Álvarez, J. Kruusma, E. Lust, V.B. Ivaništšev, Calculation of core-level electron spectra of ionic liquids, Int. J. Quantum Chem. 120 (2020) e26247.
14. I.V. Voroshylova, M. Lembinen, **H. Ers**, M. Mišin, V.A. Koverga, C.M. Pereira, V.B. Ivaništšev, M.N.D.S. Cordeiro, On the role of the surface charge plane position at Au(hkl)–BMImPF6 interfaces, Electrochim. Acta 318 (2019) 76–82.
15. K. Karu, M. Mišin, **H. Ers**, J. Sun, V. Ivaništšev, Performance of SCAN density functional for a set of ionic liquid ion pairs, Int. J. Quantum. Chem. 118 (2018) e25582.
16. A. Ruzanov, M. Lembinen, **H. Ers**, J.M. García de la Vega, I. Lage-Estebanez, E. Lust, V.B. Ivaništšev, Density Functional Theory Study of Ionic Liquid Adsorption on Circumcoronene Shaped Graphene, J. Phys. Chem. C 122 (2018) 2624–2631.
17. K. Karu, A. Ruzanov, **H. Ers**, V. Ivaništšev, I. Lage-Estebanez, J.M. García de la Vega, Predictions of Physicochemical Properties of Ionic Liquids with DFT, Computation 4 (2016) 25.

ELULOOKIRJELDUS

Nimi:	Heigo Ers
Sünniaeg:	27. jaanuar, 1995
Kodakondsus:	Eesti
Kontakt:	Tartu Ülikool, Keemia Instituut, Ravila 14a, 50411, Tartu, Eesti
E-mail:	heigoers@ut.ee

Haridus:

2020–…	Tartu Ülikool, Keemia, doktoriõpe
2018–2020	Tartu Ülikool, Keemia, magistriõpe, *cum laude*
2014–2018	Tartu Ülikool, Keemia, bakalaureuseõpe, *cum laude*

Töökogemus:

2021–…	Tartu Ülikool, Loodus- ja täppisteaduste valdkond, keemia instituut, spetsialist
2018–2019	Tartu Ülikool, Loodus- ja täppisteaduste valdkond, ökoloogia ja maateaduste instituut, spetsialist

Teaduspublikatsioonid:

1. **H. Ers**, L. Siinor, P. Pikma, Maintaining the order: 4,4′-bipyridine self-assembled layers on the Bi(111) | ionic liquid interface, Electrochim. Acta (2024) 144081.
2. L. Siinor, **H. Ers**, P. Pikma, Another Piece of the Ionic Liquid′s Puzzle: Adsorption of Cl^- Ions, J. Phys. Chem. C 128 (2024) 2722–2729.
3. L. Siinor, **H. Ers**, P. Pikma, The adsorption of organic molecules and inorganic ions – case studies in aqueous, organic and ionic liquid electrolytes, in: K. Wandelt, G. Bussetti (Eds.), Encyclopedia of Solid-Liquid Interfaces (First Edition), Elsevier, Oxford, 2024: pp. 681–691.
4. **H. Ers**, L. Siinor, P. Pikma, The adsorption of 4,4′-bipyridine at a Cd(0001)| ionic liquid interface – The descent into disorder, Electrochem. Commun. 148 (2023) 107451.
5. **H. Ers**, P. Pikma, R. Palm, M. Paalo, A. Jänes, T. Thomberg, M. Härmas, R. Härmas, L. Kalder, L.-K. Salvan, P. Teppor, R. Jäger, H. Kasuk, J. Nerut, S. Sepp, G. Nurk, K. Lust, E. Lust, Teaching electrochemistry and student participation in the development of sustainable electricity generation/storage devices at the Institute of Chemistry of the University of Tartu, J Solid State Electrochem (2023).
6. P. Pikma, **H. Ers**, L. Siinor, J. Zhao, O. Oll, T. Romann, V. Grozovski, C. Siimenson, M. Väärtnõu, M. Paalo, R. Härmas, K. Lust, T. Thomberg, A. Jänes, J. Nerut, R. Jäger, P. Valk, I. Kivi, M. Maide, P. Möller, R. Kanarbik, G. Nurk, E. Lust, The review of advances in interfacial electrochemistry in Estonia: electrochemical double layer and adsorption studies for the development of electrochemical devices, J Solid State Electrochem (2022).

7. **H. Ers**, I.V. Voroshylova, P. Pikma, V.B. Ivaništšev, Double layer in ionic liquids: Temperature effect and bilayer model, J. Mol. Liq. 363 (2022) 119747.
8. **H. Ers**, L. Siinor, C. Siimenson, E. Lust, P. Pikma, Order beyond a monolayer: The story of two self-assembled 4,4′-bipyridine layers on the Sb(111) | ionic liquid interface, Electrochim. Acta 421 (2022) 140468.
9. **H. Ers**, J. Nerut, E. Lust, P. Pikma, Long-term stability of Cd(0001) single crystal | ionic liquid interface – The effect of I^- addition, J. Electroanal. Chem. 903 (2021) 115826.
10. I.V. Voroshylova, **H. Ers**, V. Koverga, B. Docampo-Álvarez, P. Pikma, V.B. Ivaništšev, M.N.D.S. Cordeiro, Ionic liquid–metal interface: The origins of capacitance peaks, Electrochim. Acta 379 (2021) 138148.
11. I.V. Voroshylova, **H. Ers**, B. Docampo-Álvarez, P. Pikma, V.B. Ivaništšev, M.N.D.S. Cordeiro, Hysteresis in the MD Simulations of Differential Capacitance at the Ionic Liquid–Au Interface, J. Phys. Chem. Lett. 11 (2020) 10408–10413.
12. **H. Ers**, M. Lembinen, M. Mišin, A.P. Seitsonen, M.V. Fedorov, V.B. Ivaništšev, Graphene–Ionic Liquid Interfacial Potential Drop from Density Functional Theory-Based Molecular Dynamics Simulations, J. Phys. Chem. C 124 (2020) 19548–19555.
13. M. Lembinen, E. Nõmmiste, **H. Ers**, B. Docampo-Álvarez, J. Kruusma, E. Lust, V.B. Ivaništšev, Calculation of core-level electron spectra of ionic liquids, Int. J. Quantum Chem. 120 (2020) e26247.
14. I.V. Voroshylova, M. Lembinen, **H. Ers**, M. Mišin, V.A. Koverga, C.M. Pereira, V.B. Ivaništšev, M.N.D.S. Cordeiro, On the role of the surface charge plane position at Au(hkl)–BMImPF6 interfaces, Electrochim. Acta 318 (2019) 76–82.
15. K. Karu, M. Mišin, **H. Ers**, J. Sun, V. Ivaništšev, Performance of SCAN density functional for a set of ionic liquid ion pairs, Int. J. Quantum. Chem. 118 (2018) e25582.
16. A. Ruzanov, M. Lembinen, **H. Ers**, J.M. García de la Vega, I. Lage-Estebanez, E. Lust, V.B. Ivaništšev, Density Functional Theory Study of Ionic Liquid Adsorption on Circumcoronene Shaped Graphene, J. Phys. Chem. C 122 (2018) 2624–2631.
17. K. Karu, A. Ruzanov, **H. Ers**, V. Ivaništšev, I. Lage-Estebanez, J.M. García de la Vega, Predictions of Physicochemical Properties of Ionic Liquids with DFT, Computation 4 (2016) 25.

DISSERTATIONES CHIMICAE UNIVERSITATIS TARTUENSIS

1. **Toomas Tamm.** Quantum-chemical simulation of solvent effects. Tartu, 1993, 110 p.
2. **Peeter Burk.** Theoretical study of gas-phase acid-base equilibria. Tartu, 1994, 96 p.
3. **Victor Lobanov.** Quantitative structure-property relationships in large descriptor spaces. Tartu, 1995, 135 p.
4. **Vahur Mäemets.** The ^{17}O and ^{1}H nuclear magnetic resonance study of H_2O in individual solvents and its charged clusters in aqueous solutions of electrolytes. Tartu, 1997, 140 p.
5. **Andrus Metsala.** Microcanonical rate constant in nonequilibrium distribution of vibrational energy and in restricted intramolecular vibrational energy redistribution on the basis of slater's theory of unimolecular reactions. Tartu, 1997, 150 p.
6. **Uko Maran.** Quantum-mechanical study of potential energy surfaces in different environments. Tartu, 1997, 137 p.
7. **Alar Jänes.** Adsorption of organic compounds on antimony, bismuth and cadmium electrodes. Tartu, 1998, 219 p.
8. **Kaido Tammeveski.** Oxygen electroreduction on thin platinum films and the electrochemical detection of superoxide anion. Tartu, 1998, 139 p.
9. **Ivo Leito.** Studies of Brønsted acid-base equilibria in water and non-aqueous media. Tartu, 1998, 101 p.
10. **Jaan Leis.** Conformational dynamics and equilibria in amides. Tartu, 1998, 131 p.
11. **Toonika Rinken.** The modelling of amperometric biosensors based on oxidoreductases. Tartu, 2000, 108 p.
12. **Dmitri Panov.** Partially solvated Grignard reagents. Tartu, 2000, 64 p.
13. **Kaja Orupõld.** Treatment and analysis of phenolic wastewater with microorganisms. Tartu, 2000, 123 p.
14. **Jüri Ivask.** Ion Chromatographic determination of major anions and cations in polar ice core. Tartu, 2000, 85 p.
15. **Lauri Vares.** Stereoselective Synthesis of Tetrahydrofuran and Tetrahydropyran Derivatives by Use of Asymmetric Horner-Wadsworth-Emmons and Ring Closure Reactions. Tartu, 2000, 184 p.
16. **Martin Lepiku.** Kinetic aspects of dopamine D_2 receptor interactions with specific ligands. Tartu, 2000, 81 p.
17. **Katrin Sak.** Some aspects of ligand specificity of P2Y receptors. Tartu, 2000, 106 p.
18. **Vello Pällin.** The role of solvation in the formation of iotsitch complexes. Tartu, 2001, 95 p.
19. **Katrin Kollist.** Interactions between polycyclic aromatic compounds and humic substances. Tartu, 2001, 93 p.

20. **Ivar Koppel.** Quantum chemical study of acidity of strong and superstrong Brønsted acids. Tartu, 2001, 104 p.
21. **Viljar Pihl.** The study of the substituent and solvent effects on the acidity of OH and CH acids. Tartu, 2001, 132 p.
22. **Natalia Palm.** Specification of the minimum, sufficient and significant set of descriptors for general description of solvent effects. Tartu, 2001, 134 p.
23. **Sulev Sild.** QSPR/QSAR approaches for complex molecular systems. Tartu, 2001, 134 p.
24. **Ruslan Petrukhin.** Industrial applications of the quantitative structure-property relationships. Tartu, 2001, 162 p.
25. **Boris V. Rogovoy.** Synthesis of (benzotriazolyl)carboximidamides and their application in relations with *N*- and *S*-nucleophyles. Tartu, 2002, 84 p.
26. **Koit Herodes.** Solvent effects on UV-vis absorption spectra of some solvatochromic substances in binary solvent mixtures: the preferential solvation model. Tartu, 2002, 102 p.
27. **Anti Perkson.** Synthesis and characterisation of nanostructured carbon. Tartu, 2002, 152 p.
28. **Ivari Kaljurand.** Self-consistent acidity scales of neutral and cationic Brønsted acids in acetonitrile and tetrahydrofuran. Tartu, 2003, 108 p.
29. **Karmen Lust.** Adsorption of anions on bismuth single crystal electrodes. Tartu, 2003, 128 p.
30. **Mare Piirsalu.** Substituent, temperature and solvent effects on the alkaline hydrolysis of substituted phenyl and alkyl esters of benzoic acid. Tartu, 2003, 156 p.
31. **Meeri Sassian.** Reactions of partially solvated Grignard reagents. Tartu, 2003, 78 p.
32. **Tarmo Tamm.** Quantum chemical modelling of polypyrrole. Tartu, 2003. 100 p.
33. **Erik Teinemaa.** The environmental fate of the particulate matter and organic pollutants from an oil shale power plant. Tartu, 2003. 102 p.
34. **Jaana Tammiku-Taul.** Quantum chemical study of the properties of Grignard reagents. Tartu, 2003. 120 p.
35. **Andre Lomaka.** Biomedical applications of predictive computational chemistry. Tartu, 2003. 132 p.
36. **Kostyantyn Kirichenko.** Benzotriazole – Mediated Carbon–Carbon Bond Formation. Tartu, 2003. 132 p.
37. **Gunnar Nurk.** Adsorption kinetics of some organic compounds on bismuth single crystal electrodes. Tartu, 2003, 170 p.
38. **Mati Arulepp.** Electrochemical characteristics of porous carbon materials and electrical double layer capacitors. Tartu, 2003, 196 p.
39. **Dan Cornel Fara.** QSPR modeling of complexation and distribution of organic compounds. Tartu, 2004, 126 p.
40. **Riina Mahlapuu.** Signalling of galanin and amyloid precursor protein through adenylate cyclase. Tartu, 2004, 124 p.

41. **Mihkel Kerikmäe.** Some luminescent materials for dosimetric applications and physical research. Tartu, 2004, 143 p.
42. **Jaanus Kruusma.** Determination of some important trace metal ions in human blood. Tartu, 2004, 115 p.
43. **Urmas Johanson.** Investigations of the electrochemical properties of polypyrrole modified electrodes. Tartu, 2004, 91 p.
44. **Kaido Sillar.** Computational study of the acid sites in zeolite ZSM-5. Tartu, 2004, 80 p.
45. **Aldo Oras.** Kinetic aspects of dATPαS interaction with $P2Y_1$ receptor. Tartu, 2004, 75 p.
46. **Erik Mölder.** Measurement of the oxygen mass transfer through the air-water interface. Tartu, 2005, 73 p.
47. **Thomas Thomberg.** The kinetics of electroreduction of peroxodisulfate anion on cadmium (0001) single crystal electrode. Tartu, 2005, 95 p.
48. **Olavi Loog.** Aspects of condensations of carbonyl compounds and their imine analogues. Tartu, 2005, 83 p.
49. **Siim Salmar.** Effect of ultrasound on ester hydrolysis in aqueous ethanol. Tartu, 2006, 73 p.
50. **Ain Uustare.** Modulation of signal transduction of heptahelical receptors by other receptors and G proteins. Tartu, 2006, 121 p.
51. **Sergei Yurchenko.** Determination of some carcinogenic contaminants in food. Tartu, 2006, 143 p.
52. **Kaido Tämm.** QSPR modeling of some properties of organic compounds. Tartu, 2006, 67 p.
53. **Olga Tšubrik.** New methods in the synthesis of multisubstituted hydrazines. Tartu. 2006, 183 p.
54. **Lilli Sooväli.** Spectrophotometric measurements and their uncertainty in chemical analysis and dissociation constant measurements. Tartu, 2006, 125 p.
55. **Eve Koort.** Uncertainty estimation of potentiometrically measured ph and pK_a values. Tartu, 2006, 139 p.
56. **Sergei Kopanchuk.** Regulation of ligand binding to melanocortin receptor subtypes. Tartu, 2006, 119 p.
57. **Silvar Kallip.** Surface structure of some bismuth and antimony single crystal electrodes. Tartu, 2006, 107 p.
58. **Kristjan Saal.** Surface silanization and its application in biomolecule coupling. Tartu, 2006, 77 p.
59. **Tanel Tätte.** High viscosity $Sn(OBu)_4$ oligomeric concentrates and their applications in technology. Tartu, 2006, 91 p.
60. **Dimitar Atanasov Dobchev**. Robust QSAR methods for the prediction of properties from molecular structure. Tartu, 2006, 118 p.
61. **Hannes Hagu**. Impact of ultrasound on hydrophobic interactions in solutions. Tartu, 2007, 81 p.
62. **Rutha Jäger.** Electroreduction of peroxodisulfate anion on bismuth electrodes. Tartu, 2007, 142 p.

63. **Kaido Viht.** Immobilizable bisubstrate-analogue inhibitors of basophilic protein kinases: development and application in biosensors. Tartu, 2007, 88 p.
64. **Eva-Ingrid Rõõm.** Acid-base equilibria in nonpolar media. Tartu, 2007, 156 p.
65. **Sven Tamp.** DFT study of the cesium cation containing complexes relevant to the cesium cation binding by the humic acids. Tartu, 2007, 102 p.
66. **Jaak Nerut.** Electroreduction of hexacyanoferrate(III) anion on Cadmium (0001) single crystal electrode. Tartu, 2007, 180 p.
67. **Lauri Jalukse.** Measurement uncertainty estimation in amperometric dissolved oxygen concentration measurement. Tartu, 2007, 112 p.
68. **Aime Lust.** Charge state of dopants and ordered clusters formation in CaF_2:Mn and CaF_2:Eu luminophors. Tartu, 2007, 100 p.
69. **Iiris Kahn**. Quantitative Structure-Activity Relationships of environmentally relevant properties. Tartu, 2007, 98 p.
70. **Mari Reinik.** Nitrates, nitrites, N-nitrosamines and polycyclic aromatic hydrocarbons in food: analytical methods, occurrence and dietary intake. Tartu, 2007, 172 p.
71. **Heili Kasuk.** Thermodynamic parameters and adsorption kinetics of organic compounds forming the compact adsorption layer at Bi single crystal electrodes. Tartu, 2007, 212 p.
72. **Erki Enkvist.** Synthesis of adenosine-peptide conjugates for biological applications. Tartu, 2007, 114 p.
73. **Svetoslav Hristov Slavov**. Biomedical applications of the QSAR approach. Tartu, 2007, 146 p.
74. **Eneli Härk.** Electroreduction of complex cations on electrochemically polished Bi(*hkl*) single crystal electrodes. Tartu, 2008, 158 p.
75. **Priit Möller.** Electrochemical characteristics of some cathodes for medium temperature solid oxide fuel cells, synthesized by solid state reaction technique. Tartu, 2008, 90 p.
76. **Signe Viggor.** Impact of biochemical parameters of genetically different pseudomonads at the degradation of phenolic compounds. Tartu, 2008, 122 p.
77. **Ave Sarapuu.** Electrochemical reduction of oxygen on quinone-modified carbon electrodes and on thin films of platinum and gold. Tartu, 2008, 134 p.
78. **Agnes Kütt.** Studies of acid-base equilibria in non-aqueous media. Tartu, 2008, 198 p.
79. **Rouvim Kadis.** Evaluation of measurement uncertainty in analytical chemistry: related concepts and some points of misinterpretation. Tartu, 2008, 118 p.
80. **Valter Reedo.** Elaboration of IVB group metal oxide structures and their possible applications. Tartu, 2008, 98 p.
81. **Aleksei Kuznetsov.** Allosteric effects in reactions catalyzed by the cAMP-dependent protein kinase catalytic subunit. Tartu, 2009, 133 p.

82. **Aleksei Bredihhin.** Use of mono- and polyanions in the synthesis of multisubstituted hydrazine derivatives. Tartu, 2009, 105 p.
83. **Anu Ploom.** Quantitative structure-reactivity analysis in organosilicon chemistry. Tartu, 2009, 99 p.
84. **Argo Vonk.** Determination of adenosine A_{2A}- and dopamine D_1 receptor-specific modulation of adenylate cyclase activity in rat striatum. Tartu, 2009, 129 p.
85. **Indrek Kivi.** Synthesis and electrochemical characterization of porous cathode materials for intermediate temperature solid oxide fuel cells. Tartu, 2009, 177 p.
86. **Jaanus Eskusson.** Synthesis and characterisation of diamond-like carbon thin films prepared by pulsed laser deposition method. Tartu, 2009, 117 p.
87. **Marko Lätt.** Carbide derived microporous carbon and electrical double layer capacitors. Tartu, 2009, 107 p.
88. **Vladimir Stepanov.** Slow conformational changes in dopamine transporter interaction with its ligands. Tartu, 2009, 103 p.
89. **Aleksander Trummal.** Computational Study of Structural and Solvent Effects on Acidities of Some Brønsted Acids. Tartu, 2009, 103 p.
90. **Eerold Vellemäe.** Applications of mischmetal in organic synthesis. Tartu, 2009, 93 p.
91. **Sven Parkel.** Ligand binding to 5-HT_{1A} receptors and its regulation by Mg^{2+} and Mn^{2+}. Tartu, 2010, 99 p.
92. **Signe Vahur.** Expanding the possibilities of ATR-FT-IR spectroscopy in determination of inorganic pigments. Tartu, 2010, 184 p.
93. **Tavo Romann**. Preparation and surface modification of bismuth thin film, porous, and microelectrodes. Tartu, 2010, 155 p.
94. **Nadežda Aleksejeva.** Electrocatalytic reduction of oxygen on carbon nanotube-based nanocomposite materials. Tartu, 2010, 147 p.
95. **Marko Kullapere.** Electrochemical properties of glassy carbon, nickel and gold electrodes modified with aryl groups. Tartu, 2010, 233 p.
96. **Liis Siinor.** Adsorption kinetics of ions at Bi single crystal planes from aqueous electrolyte solutions and room-temperature ionic liquids. Tartu, 2010, 101 p.
97. **Angela Vaasa.** Development of fluorescence-based kinetic and binding assays for characterization of protein kinases and their inhibitors. Tartu 2010, 101 p.
98. **Indrek Tulp.** Multivariate analysis of chemical and biological properties. Tartu 2010, 105 p.
99. **Aare Selberg.** Evaluation of environmental quality in Northern Estonia by the analysis of leachate. Tartu 2010, 117 p.
100. **Darja Lavõgina.** Development of protein kinase inhibitors based on adenosine analogue-oligoarginine conjugates. Tartu 2010, 248 p.
101. **Laura Herm.** Biochemistry of dopamine D_2 receptors and its association with motivated behaviour. Tartu 2010, 156 p.

102. **Terje Raudsepp.** Influence of dopant anions on the electrochemical properties of polypyrrole films. Tartu 2010, 112 p.
103. **Margus Marandi.** Electroformation of Polypyrrole Films: *In-situ* AFM and STM Study. Tartu 2011, 116 p.
104. **Kairi Kivirand.** Diamine oxidase-based biosensors: construction and working principles. Tartu, 2011, 140 p.
105. **Anneli Kruve.** Matrix effects in liquid-chromatography electrospray mass-spectrometry. Tartu, 2011, 156 p.
106. **Gary Urb.** Assessment of environmental impact of oil shale fly ash from PF and CFB combustion. Tartu, 2011, 108 p.
107. **Nikita Oskolkov.** A novel strategy for peptide-mediated cellular delivery and induction of endosomal escape. Tartu, 2011, 106 p.
108. **Dana Martin.** The QSPR/QSAR approach for the prediction of properties of fullerene derivatives. Tartu, 2011, 98 p.
109. **Säde Viirlaid.** Novel glutathione analogues and their antioxidant activity. Tartu, 2011, 106 p.
110. **Ülis Sõukand.** Simultaneous adsorption of Cd^{2+}, Ni^{2+}, and Pb^{2+} on peat. Tartu, 2011, 124 p.
111. **Lauri Lipping.** The acidity of strong and superstrong Brønsted acids, an outreach for the "limits of growth": a quantum chemical study. Tartu, 2011, 124 p.
112. **Heisi Kurig.** Electrical double-layer capacitors based on ionic liquids as electrolytes. Tartu, 2011, 146 p.
113. **Marje Kasari.** Bisubstrate luminescent probes, optical sensors and affinity adsorbents for measurement of active protein kinases in biological samples. Tartu, 2012, 126 p.
114. **Kalev Takkis.** Virtual screening of chemical databases for bioactive molecules. Tartu, 2012, 122 p.
115. **Ksenija Kisseljova**. Synthesis of aza-β^3-amino acid containing peptides and kinetic study of their phosphorylation by protein kinase A. Tartu, 2012, 104 p.
116. **Riin Rebane.** Advanced method development strategy for derivatization LC/ESI/MS. Tartu, 2012, 184 p.
117. **Vladislav Ivaništšev.** Double layer structure and adsorption kinetics of ions at metal electrodes in room temperature ionic liquids. Tartu, 2012, 128 p.
118. **Irja Helm.** High accuracy gravimetric Winkler method for determination of dissolved oxygen. Tartu, 2012, 139 p.
119. **Karin Kipper.** Fluoroalcohols as Components of LC-ESI-MS Eluents: Usage and Applications. Tartu, 2012, 164 p.
120. **Arno Ratas.** Energy storage and transfer in dosimetric luminescent materials. Tartu, 2012, 163 p.
121. **Reet Reinart-Okugbeni**. Assay systems for characterisation of subtype-selective binding and functional activity of ligands on dopamine receptors. Tartu, 2012, 159 p.

122. **Lauri Sikk.** Computational study of the Sonogashira cross-coupling reaction. Tartu, 2012, 81 p.
123. **Karita Raudkivi.** Neurochemical studies on inter-individual differences in affect-related behaviour of the laboratory rat. Tartu, 2012, 161 p.
124. **Indrek Saar.** Design of GalR2 subtype specific ligands: their role in depression-like behavior and feeding regulation. Tartu, 2013, 126 p.
125. **Ann Laheäär.** Electrochemical characterization of alkali metal salt based non-aqueous electrolytes for supercapacitors. Tartu, 2013, 127 p.
126. **Kerli Tõnurist.** Influence of electrospun separator materials properties on electrochemical performance of electrical double-layer capacitors. Tartu, 2013, 147 p.
127. **Kaija Põhako-Esko.** Novel organic and inorganic ionogels: preparation and characterization. Tartu, 2013, 124 p.
128. **Ivar Kruusenberg.** Electroreduction of oxygen on carbon nanomaterial-based catalysts. Tartu, 2013, 191 p.
129. **Sander Piiskop.** Kinetic effects of ultrasound in aqueous acetonitrile solutions. Tartu, 2013, 95 p.
130. **Ilona Faustova**. Regulatory role of L-type pyruvate kinase N-terminal domain. Tartu, 2013, 109 p.
131. **Kadi Tamm.** Synthesis and characterization of the micro-mesoporous anode materials and testing of the medium temperature solid oxide fuel cell single cells. Tartu, 2013, 138 p.
132. **Iva Bozhidarova Stoyanova-Slavova.** Validation of QSAR/QSPR for regulatory purposes. Tartu, 2013, 109 p.
133. **Vitali Grozovski**. Adsorption of organic molecules at single crystal electrodes studied by *in situ* STM method. Tartu, 2014, 146 p.
134. **Santa Veikšina**. Development of assay systems for characterisation of ligand binding properties to melanocortin 4 receptors. Tartu, 2014, 151 p.
135. **Jüri Liiv.** PVDF (polyvinylidene difluoride) as material for active element of twisting-ball displays. Tartu, 2014, 111 p.
136. **Kersti Vaarmets.** Electrochemical and physical characterization of pristine and activated molybdenum carbide-derived carbon electrodes for the oxygen electroreduction reaction. Tartu, 2014, 131 p.
137. **Lauri Tõntson**. Regulation of G-protein subtypes by receptors, guanine nucleotides and Mn^{2+}. Tartu, 2014, 105 p.
138. **Aiko Adamson.** Properties of amine-boranes and phosphorus analogues in the gas phase. Tartu, 2014, 78 p.
139. **Elo Kibena**. Electrochemical grafting of glassy carbon, gold, highly oriented pyrolytic graphite and chemical vapour deposition-grown graphene electrodes by diazonium reduction method. Tartu, 2014, 184 p.
140. **Teemu Näykki.** Novel Tools for Water Quality Monitoring – From Field to Laboratory. Tartu, 2014, 202 p.
141. **Karl Kaupmees.** Acidity and basicity in non-aqueous media: importance of solvent properties and purity. Tartu, 2014, 128 p.

142. **Oleg Lebedev**. Hydrazine polyanions: different strategies in the synthesis of heterocycles. Tartu, 2015, 118 p.
143. **Geven Piir.** Environmental risk assessment of chemicals using QSAR methods. Tartu, 2015, 123 p.
144. **Olga Mazina.** Development and application of the biosensor assay for measurements of cyclic adenosine monophosphate in studies of G protein-coupled receptor signalinga. Tartu, 2015, 116 p.
145. **Sandip Ashokrao Kadam.** Anion receptors: synthesis and accurate binding measurements. Tartu, 2015, 116 p.
146. **Indrek Tallo.** Synthesis and characterization of new micro-mesoporous carbide derived carbon materials for high energy and power density electrical double layer capacitors. Tartu, 2015, 148 p.
147. **Heiki Erikson.** Electrochemical reduction of oxygen on nanostructured palladium and gold catalysts. Tartu, 2015, 204 p.
148. **Erik Anderson.** *In situ* Scanning Tunnelling Microscopy studies of the interfacial structure between Bi(111) electrode and a room temperature ionic liquid. Tartu, 2015, 118 p.
149. **Girinath G. Pillai.** Computational Modelling of Diverse Chemical, Biochemical and Biomedical Properties. Tartu, 2015, 140 p.
150. **Piret Pikma.** Interfacial structure and adsorption of organic compounds at Cd(0001) and Sb(111) electrodes from ionic liquid and aqueous electrolytes: an *in situ* STM study. Tartu, 2015, 126 p.
151. **Ganesh babu Manoharan.** Combining chemical and genetic approaches for photoluminescence assays of protein kinases. Tartu, 2016, 126 p.
152. **Carolin Siimenson**. Electrochemical characterization of halide ion adsorption from liquid mixtures at Bi(111) and pyrolytic graphite electrode surface. Tartu, 2016, 110 p.
153. **Asko Laaniste.** Comparison and optimisation of novel mass spectrometry ionisation sources. Tartu, 2016, 156 p.
154. **Hanno Evard.** Estimating limit of detection for mass spectrometric analysis methods. Tartu, 2016, 224 p.
155. **Kadri Ligi.** Characterization and application of protein kinase-responsive organic probes with triplet-singlet energy transfer. Tartu, 2016, 122 p.
156. **Margarita Kagan.** Biosensing penicillins' residues in milk flows. Tartu, 2016, 130 p.
157. **Marie Kriisa.** Development of protein kinase-responsive photoluminescent probes and cellular regulators of protein phosphorylation. Tartu, 2016, 106 p.
158. **Mihkel Vestli.** Ultrasonic spray pyrolysis deposited electrolyte layers for intermediate temperature solid oxide fuel cells. Tartu, 2016, 156 p.
159. **Silver Sepp**. Influence of porosity of the carbide-derived carbon on the properties of the composite electrocatalysts and characteristics of polymer electrolyte fuel cells. Tartu, 2016, 137 p.
160. **Kristjan Haav**. Quantitative relative equilibrium constant measurements in supramolecular chemistry. Tartu, 2017, 158 p.

161. **Anu Teearu**. Development of MALDI-FT-ICR-MS methodology for the analysis of resinous materials. Tartu, 2017, 205 p.
162. **Taavi Ivan**. Bifunctional inhibitors and photoluminescent probes for studies on protein complexes. Tartu, 2017, 140 p.
163. **Maarja-Liisa Oldekop**. Characterization of amino acid derivatization reagents for LC-MS analysis. Tartu, 2017, 147 p.
164. **Kristel Jukk**. Electrochemical reduction of oxygen on platinum- and palladium-based nanocatalysts. Tartu, 2017, 250 p.
165. **Siim Kukk**. Kinetic aspects of interaction between dopamine transporter and *N*-substituted nortropane derivatives. Tartu, 2017, 107 p.
166. **Birgit Viira**. Design and modelling in early drug development in targeting HIV-1 reverse transcriptase and Malaria. Tartu, 2017, 172 p.
167. **Rait Kivi**. Allostery in cAMP dependent protein kinase catalytic subunit. Tartu, 2017, 115 p.
168. **Agnes Heering**. Experimental realization and applications of the unified acidity scale. Tartu, 2017, 123 p.
169. **Delia Juronen**. Biosensing system for the rapid multiplex detection of mastitis-causing pathogens in milk. Tartu, 2018, 85 p.
170. **Hedi Rahnel.** ARC-inhibitors: from reliable biochemical assays to regulators of physiology of cells. Tartu, 2018, 176 p.
171. **Anton Ruzanov.** Computational investigation of the electrical double layer at metal–aqueous solution and metal–ionic liquid interfaces. Tartu, 2018, 129 p.
172. **Katrin Kestav.** Crystal Structure-Guided Development of Bisubstrate-Analogue Inhibitors of Mitotic Protein Kinase Haspin. Tartu, 2018, 166 p.
173. **Mihkel Ilisson.** Synthesis of novel heterocyclic hydrazine derivatives and their conjugates. Tartu, 2018, 101 p.
174. **Anni Allikalt.** Development of assay systems for studying ligand binding to dopamine receptors. Tartu, 2018, 160 p.
175. **Ove Oll.** Electrical double layer structure and energy storage characteristics of ionic liquid based capacitors. Tartu, 2018, 187 p.
176. **Rasmus Palm.** Carbon materials for energy storage applications. Tartu, 2018, 114 p.
177. **Jörgen Metsik.** Preparation and stability of poly(3,4-ethylenedioxythiophene) thin films for transparent electrode applications. Tartu, 2018, 111 p.
178. **Sofja Tšepelevitš.** Experimental studies and modeling of solute-solvent interactions. Tartu, 2018, 109 p.
179. **Märt Lõkov.** Basicity of some nitrogen, phosphorus and carbon bases in acetonitrile. Tartu, 2018, 104 p.
180. **Anton Mastitski**. Preparation of α-aza-amino acid precursors and related compounds by novel methods of reductive one-pot alkylation and direct alkylation. Tartu, 2018, 155 p.
181. **Jürgen Vahter**. Development of bisubstrate inhibitors for protein kinase CK2. Tartu, 2019, 186 p.

182. **Piia Liigand.** Expanding and improving methodology and applications of ionization efficiency measurements. Tartu, 2019, 189 p.
183. **Sigrid Selberg.** Synthesis and properties of lipophilic phosphazene-based indicator molecules. Tartu, 2019, 74 p.
184. **Jaanus Liigand.** Standard substance free quantification for LC/ESI/MS analysis based on the predicted ionization efficiencies. Tartu, 2019, 254 p.
185. **Marek Mooste.** Surface and electrochemical characterisation of aryl film and nanocomposite material modified carbon and metal-based electrodes. Tartu, 2019, 304 p.
186. **Mare Oja.** Experimental investigation and modelling of pH profiles for effective membrane permeability of drug substances. Tartu, 2019, 306 p.
187. **Sajid Hussain.** Electrochemical reduction of oxygen on supported Pt catalysts. Tartu, 2019, 220 p.
188. **Ronald Väli.** Glucose-derived hard carbon electrode materials for sodium-ion batteries. Tartu, 2019, 180 p.
189. **Ester Tee.** Analysis and development of selective synthesis methods of hierarchical micro- and mesoporous carbons. Tartu, 2019, 210 p.
190. **Martin Maide.** Influence of the microstructure and chemical composition of the fuel electrode on the electrochemical performance of reversible solid oxide fuel cell. Tartu, 2020, 144 p.
191. **Edith Viirlaid.** Biosensing Pesticides in Water Samples. Tartu, 2020, 102 p.
192. **Maike Käärik.** Nanoporous carbon: the controlled nanostructure, and structure-property relationships. Tartu, 2020, 162 p.
193. **Artur Gornischeff.** Study of ionization efficiencies for derivatized compounds in LC/ESI/MS and their application for targeted analysis. Tartu, 2020, 124 p.
194. **Reet Link.** Ligand binding, allosteric modulation and constitutive activity of melanocortin-4 receptors. Tartu, 2020, 108 p.
195. **Pilleriin Peets.** Development of instrumental methods for the analysis of textile fibres and dyes. Tartu, 2020, 150 p.
196. **Larisa Ivanova.** Design of active compounds against neurodegenerative diseases. Tartu, 2020, 152 p.
197. **Meelis Härmas.** Impact of activated carbon microstructure and porosity on electrochemical performance of electrical double-layer capacitors. Tartu, 2020, 122 p.
198. **Ruta Hecht.** Novel Eluent Additives for LC-MS Based Bioanalytical Methods. Tartu, 2020, 202 p.
199. **Max Hecht.** Advances in the Development of a Point-of-Care Mass Spectrometer Test. Tartu, 2020, 168 p.
200. **Ida Rahu.** Bromine formation in inorganic bromide/nitrate mixtures and its application for oxidative aromatic bromination. Tartu, 2020, 116 p.
201. **Sander Ratso**. Electrocatalysis of oxygen reduction on non-precious metal catalysts. Tartu, 2020, 371 p.
202. **Astrid Darnell.** Computational design of anion receptors and evaluation of host-guest binding. Tartu, 2021, 150 p.

203. **Ove Korjus.** The development of ceramic fuel electrode for solid oxide cells. Tartu, 2021, 150 p.
204. **Merit Oss.** Ionization efficiency in electrospray ionization source and its relations to compounds' physico-chemical properties. Tartu, 2021, 124 p.
205. **Madis Lüsi**. Electroreduction of oxygen on nanostructured palladium catalysts. Tartu, 2021, 180 p.
206. **Eliise Tammekivi.** Derivatization and quantitative gas-chromatographic analysis of oils. Tartu, 2021, 122 p.
207. **Simona Selberg.** Development of Small-Molecule Regulators of Epi-transcriptomic Processes. Tartu, 2021, 122 p.
208. **Olivier Etebe Nonga.** Inhibitors and photoluminescent probes for in vitro studies on protein kinases PKA and PIM. Tartu, 2021, 189 p.
209. **Riinu Härmas.** The structure and H2 diffusion in porous carbide-derived carbon particles. Tartu, 2022, 123 p.
210. **Maarja Paalo.** Synthesis and characterization of novel carbon electrodes for high power density electrochemical capacitors. Tartu, 2022, 144 p.
211. **Jinfeng Zhao.** Electrochemical characteristics of Bi(hkl) and micro-meso-porous carbon electrodes in ionic liquid based electrolytes. Tartu, 2022, 134 p.
212. **Alar Heinsaar.** Investigation of oxygen electrode materials for high-temperature solid oxide cells in natural conditions. Tartu, 2022, 120 p.
213. **Jaana Lilloja.** Transition metal and nitrogen doped nanocarbon cathode catalysts for anion exchange membrane fuel cells. Tartu, 2022, 202 p.
214. **Maris-Johanna Tahk.** Novel fluorescence-based methods for illuminating transmembrane signal transduction by G-protein coupled receptors. Tartu, 2022, 200 p.
215. **Eerik Jõgi.** Development and Applications of E. coli Immunosensor. Tartu, 2022, 103 p.
216. **Alo Rüütel.** Design principles of synthetic molecular receptors for anion-selective electrodes. Tartu, 2022, 109 p.
217. **Tanel Sõrmus.** Development of stimuli-responsive and covalent bisub-strate inhibitors of protein kinases. Tartu, 2022, 148 p.
218. **Oleg Artemchuk.** Autotrophic nitrogen removal processes for nutrient removal from sidestream and mainstream wastewater. Tartu, 2022, 115 p.
219. **Andre Leesment.** Quantitative studies of Brønsted acidity in biphasic systems and gas-phase. Tartu, 2023, 83 p.
220. **Meeli Arujõe-Sado.** Structural effects in aza-peptide bond formation re-action. Tartu, 2023, 83 p.
221. **Jonas Mart Linge.** Electrochemical reduction of oxygen on silver-based catalysts. Tartu, 2023, 269 p.
222. **Tõnis Laasfeld.** Integrating Image Analysis and Quantitative Modeling for a Holistic View of GPCR Ligand Binding Dynamics. Tartu, 2023, 226 p.
223. **Ernesto de Jesus Zapata Flores.** Derivatization Reagents used in nega-tive mode electrospray LC-MS. Tartu, 2023, 107 p.

224. **Patrick Teppor.** Obtaining platinum-free oxygen reduction catalysts through biomass valorization: a case study of peat. Tartu, 2023, 161 p.
225. **Peeter Valk.** Methanol Oxidation on Platinum-Rare-Earth Metal Oxide Activated Catalysts. Tartu, 2023, 162 p.
226. **Shidong Chen.** Unravelling prehistoric plant exploitation in eastern Baltic: organic residue analysis of plant-based materials by multi-method approach. Tartu, 2023, 245 p.
227. **Yogesh Kumar.** M-N_4 macrocycle-based catalysts for electrocatalysis of oxygen reduction and oxygen evolution. Tartu, 2023, 224 p.
228. **Kerli Martin.** Recognition of carboxylates by synthetic receptors – from structure-affinity studies to solid-contact anion-selective electrode prototyping. Tartu, 2024, 130 p.
229. **Huy Quí Vinh Nguyen.** Development of Carbon Supported Pt–CeO_2 Catalysts for Proton Exchange Membrane Fuel Cells. Tartu, 2024, 198 p.